

AD-A032 509

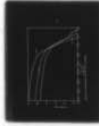
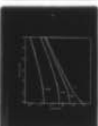
RICE UNIV HOUSTON TEX DEPT OF SPACE PHYSICS AND ASTRONOMY F/G 4/1
LARGE SCALE ATMOSPHERIC ELECTRIC FIELDS: COMPARISONS WITH BALLO--ETC(U)
NOV 75 H K BURKE
TR061-761

N00014-67-A-0145-0006

NL

UNCLASSIFIED

1 of 2
AD
A032509



ADA032509

1.

DDC
RECEIVED
NOV 23 1976
RESERVE

ONE COPY ONLY
of complete text to TR011-7C1

6

DISTRIBUTION STATEMENT A
Approved for public release;
Distribution is limited

REPORT DOCUMENTATION PAGE		READ INSTRUCTIONS BEFORE COMPLETING FORM
1. REPORT NUMBER TR061-761	2. GOVT ACCESSION NO.	3. RECIPIENT'S CATALOG NUMBER
4. TITLE (and Subtitle) Large Scale Atmospheric Electric Fields; Comparisons with Balloon Data.		5. TYPE OF REPORT & PERIOD COVERED Technical Rept. 09
7. AUTHOR(s) Hsiao-hua Kuo Burke		6. PERFORMING ORG. REPORT NUMBER
9. PERFORMING ORGANIZATION NAME AND ADDRESS Rice University - A. A. Few P. O. Box 1892 Houston, Texas 77001		8. CONTRACT OR GRANT NUMBER(s) N00014-67-A-0145-0006 NEW
11. CONTROLLING OFFICE NAME AND ADDRESS Physics Program and Atmospheric Sciences Program, Code 465 and 421 Office of Naval Res., Arlington, VA 22217		10. PROGRAM ELEMENT, PROJECT, TASK AREA & WORK UNIT NUMBERS 11 Nov 75
14. MONITORING AGENCY NAME & ADDRESS (if different from Controlling Office)		12. REPORT DATE 18 October 1976
		13. NUMBER OF PAGES 6 (complete text 128 pp)
		15. SECURITY CLASS. (of this report)
		15a. DECLASSIFICATION/DOWNGRADING SCHEDULE
16. DISTRIBUTION STATEMENT (of this Report) Approved for public release; distribution unlimited.		
17. DISTRIBUTION STATEMENT (of the abstract entered in Block 20, if different from Report)		
18. SUPPLEMENTARY NOTES Ph.D thesis published at Rice University May, 1976. Copies available from University Microfilms, Zeeb Road, Ann Arbor, Michigan 48104. This is standard distribution in accordance with contract.		
19. KEY WORDS (Continue on reverse side if necessary and identify by block number) Atmospheric Electricity, Electric Fields, Atmospheric Ions, Electrified Clouds, Lightning Transients.		
20. ABSTRACT (Continue on reverse side if necessary and identify by block number) A new more general technique for calculating large scale electric fields in the Earth's atmosphere is developed. This allows more detailed and accurate mapping of tropospheric fields upward and upper atmospheric fields downward; interactions in the stratosphere can be explored. Electric Field Data from stratospheric balloons are compared with the predicted fields.		

0

by

A THESIS SUBMITTED

DOCTOR OF PHILOSOPHY

REC'D
NOV 23 1976
REGISTERED

Houston, Texas

ADMISSION (UP)

REG	REG. Section	<input checked="" type="checkbox"/>
ENC	ENC. Section	<input type="checkbox"/>
CHARGE		<input type="checkbox"/>
ADMISSION		

BY _____

RECEIVED/ADMISSION OFFICE

DATE _____

TIME _____

A

DISTRIBUTION STATEMENT A
Approved for public release;
Distribution Unlimited

CONTENTS

CHAPTER 1 INTRODUCTION

I. General Review of Atmospheric Electricity	1
II. Ions, Mobilities, and Conductivities	2
III. The Conductivity Profile	5

CHAPTER 2 THEORETICAL MODEL OF FIELD MAPPING IN THE ATMOSPHERE

I. Summary of Work in the Past	17
II. Basic Equations	18
III. Fair Weather Fields	20
IV. Solution for Thunderstorm Fields	23
V. Different Charge Sources	26

CHAPTER 3 ELECTRIC FIELDS MAPPED INTO THE IONOSPHERE

I. Theory and Solution without Boundary Conditions	42
II. Boundary Conditions	46
III. Results	50

CHAPTER 4 COMPARISONS BETWEEN MODEL AND DATA FROM A BALLOON FLIGHT

I. Description of the Balloon Flight and Data	66
II. Fair Weather Field Data	69
III. Expected Thunderstorm Field and Comparison with Data	70
IV. A Study of Lightning Events	77

CHAPTER 5 DISCUSSION

I. An Outline of the Electrical Structure in the Atmosphere, Ionosphere, and Magnetosphere	108
II. Techniques of Electric Field Mapping	111
III. Experimental Techniques	113
IV. Future Prospects	114

MATHEMATICAL APPENDIX	118
ACKNOWLEDGEMENTS	123
REFERENCES	124

LARGE SCALE ATMOSPHERIC ELECTRIC FIELDS:
COMPARISONS WITH BALLOON DATA

by

Hsiao-hua Kuo Burke

ABSTRACT

Measurements of air conductivity have indicated that the conductivity of the atmosphere can be approximated as an exponentially increasing function of the altitude with a scale height of 5-6 km. Because of this property, the atmospheric electric fields produced by a variety of charge sources cannot be described by the simple Coulomb field relationship. In this thesis, a new theoretical approach is employed to calculate the large-scale weather-induced atmospheric fields at different altitudes. The Green's function method is used to obtain analytic solutions for different charge sources. This mapping technique is then extended into the lower ionosphere where the conductivity is of a tensor form.

The model is used to evaluate high-altitude electric-field data from a balloon flight. The balloon was launched on August 3, 1969, from Penhold, Canada, and measured vector electric fields at 28 km for a period of 24 hours. Data included the electric fields of a local thunderstorm during the earlier portion of the flight and fair weather fields during the later portion.

Comparisons between theoretical models and balloon data indicate that during the storm the balloon was about 22 km south of the thunder-

clouds and that it was moving east relative to the storm. The thundercloud model charges were calculated to be ± 20 Coul (20 Coul in the upper portion at ~ 6 km and -20 Coul in the lower portion at ~ 4 km) for each major cell. A downward field of 0.3 V/m at 28 km was assumed in the calculation; this assumed value agrees with the fair-weather data measured later in the flight and with theoretical estimates. The results also indicated that a shielding layer existed at the cloud boundary; the total shielding charge was around 5 Coul.

One portion of the data contained intra-cloud-lightning field changes. The amount of each lightning discharge was estimated to be approximately the same as the total charge in the cell. The time constant for field recovery after each flash was also studied. The recovery time constant ranged between 2.5 sec and 7.5 sec. In addition to the distance dependence readily obtainable from the potential equation, it was observed that this time constant was also related to the amount of discharge.

CHAPTER 1

INTRODUCTION

I. General Review of Atmospheric Electricity

For a long time, the study of atmospheric electricity was confined to the theory of "concentric spherical capacitor" (cf. Chalmers, 1967). The lower boundary of this capacitor was the earth's surface and the electrosphere, a highly conducting layer at about 50-70 km, was the upper boundary. The electrosphere was defined as the height at which the equipotential condition was reached. Being a good conductor, it acted as a perfect electrostatic shield. As a result, thunderstorms and other electrical phenomena in the lower atmosphere would not have any effect outside the electrosphere. At the same time, charges bombarding the ionosphere from outside should not have any effect in the lower atmosphere unless they penetrate through the electrosphere. In this classical picture, the thunderstorm activity would act as the major mechanism for charge generation and the fair weather conduction current as the consumer.

This "close-in" theory on atmospheric electricity works in most aspects except it does not allow any horizontal atmospheric electric field which is known to exist both from weather and ionospheric origins. A closer look at the electrosphere also indicates that such an ideal equipotential layer does not exist. Thus the perfect capacitor now becomes a leaky one which allows the atmospheric electric phenomena to interact with the ionosphere and magnetosphere. Influences of solar and

extraterrestrial activities are also taken into consideration. This leads to a new realm of atmospheric electricity studies. The mapping of electric fields between the atmosphere and the ionosphere is thus an essential step.

II. Ions, Mobilities and Conductivities

Electric field modeling depends largely on the air conductivity in the environment. It is therefore necessary to take a close look at the conductivity of air at different altitudes.

The air is a slightly conducting medium due to the presence of ions continuously produced in the atmosphere. The ionization agencies include (1) cosmic radiation, (2) radiation from radioactive substances from soil and (3) radioactive gases produced by decay of (2).

Among them (1) is mainly responsible for air conductivity at higher altitudes while (2) and (3) are dominant in the lower atmosphere. Table 1-1 shows average ion pair production rates due to radioactivity and cosmic radiation between 0 and 10 km.

The conductivity σ of air is defined as

$$\sigma = \sum_{i=1}^m n_i e_i k_i \quad (1-1)$$

where m is the number of different ion species present, and n_i , e_i , k_i , are the number density, charge and mobility of the i^{th} ion species respectively. Small ions, because of their low mass, have higher mobility than large ions. They contribute over 95% to the total conductivity of

Altitude (km)	Ion pairs ($\text{cm}^{-3}\text{sec}^{-1}$)		
	radioactive	cosmic rays	Total
0	7.6	1.5	9.1
0.5	3.8	1.8	5.6
1	2.7	2.6	5.3
2	1.5	5.0	6.5
3	0.9	8.0	8.9
4	0.5	15.0	15.5
5	0.3	23.0	23.3
6	---	37.0	37.0
8	---	75.0	75.0
10	---	125.0	125.0

Table 1-1

Average ion pair production rates due to
radioactivity and cosmic radiation as a
function of altitude
(Sagalyn and Fitzgerald, 1965)

the air so that

$$\sigma \approx n_+ e k_+ + n_- e k_- \quad (1-2)$$

where n_+ and n_- are number densities of positive and negative small ions and k_+ and k_- are their mobilities. Near earth's surface, $n_+ \approx 600 \text{ cm}^{-3}$, $n_- \approx 500 \text{ cm}^{-3}$, $k_+ \approx 1.3 \text{ cm}^2 \text{V}^{-1} \text{ sec}^{-1}$ and $k_- \approx 1.6 \text{ cm}^2 \text{V}^{-1} \text{ sec}^{-1}$ which give a conductivity of about $2.5 \times 10^{-14} \text{ ohm}^{-1} \text{ m}^{-1}$ or $2.5 \times 10^{-16} \text{ ohm}^{-1} \text{ cm}^{-1}$.

The conductivity of air increases rapidly with altitude due to the following reasons:

- (1) The mobility of ions increases when the neutral number density decreases. This is the dominant factor for the increase of conductivity. To prove this property, we start from the relation for the ion mobility k ,

$$k \propto \frac{\bar{v} \cdot l}{T},$$

where the parameters are

\bar{v} , the mean thermal velocity of the ions,

l , the mean free path of ions, and

T , the temperature of the air.

The increase of conductivity with respect to \bar{v} and l is obvious. Conductivity also increases with the decrease of viscosity and in a gas viscosity increase proportionally with temperature which implies the relationship of $k \propto \frac{1}{T}$. Since $l \propto \frac{1}{n}$, n being the neutral number density, and $v \propto \sqrt{T}$, we get $k \propto \frac{1}{n\sqrt{T}}$. Then from

$$n \propto e^{-z/h}$$

where z is the altitude and h the scale height of density, we reach the conclusion that conductivity increases as we go higher. Figure 1-1 shows the variation of ion mobility k with atmospheric neutral number density.

- (2) The presence of numerous large aerosols lowers the conductivity of air near ground. After small ions attach themselves to aerosols, their mobility, and hence the conductivity of air, is decreased due to the increase of the collisional cross sectional area.
- (3) The effect of cosmic radiation on ionization increases with altitude (Table 1-1) in the lower atmosphere.

III. The Conductivity Profile

(i) Atmospheric Conductivity Profile

Variations of electrical conductivity in the atmosphere as a function of altitude have been observed by a number of people (cf. Benbrook et al. 1974; Bragin, 1967; Paltridge, 1965; Hatakeyama, 1963; Kraakevik, 1958). Cole and Pierce (1965) deduced a conductivity profile versus height (Figure 1-2) based on observations on variations of electron and ion concentrations and effective collisional frequencies with respect to altitude. From this figure the conductivity profile in the atmosphere was modeled as

$$\sigma(z) = \begin{cases} 3 \times 10^{-15} \exp(z/0.82) \text{ ohm}^{-1}\text{m}^{-1} & 0 \leq z \leq 3.6 \\ 1 \times 10^{-13} \exp(z/4.1) \text{ ohm}^{-1}\text{m}^{-1} & 3.6 \leq z \leq 17.7 \\ 6 \times 10^{-13} \exp(z/7.0) \text{ ohm}^{-1}\text{m}^{-1} & 17.7 \leq z \leq 40 \end{cases}$$

where z is the height in kilometers.

Because of this variational property of conductivity, the air can not be treated as a uniformly conducting medium when the electric field of interest is extended beyond a few kilometers.

As a convenient large-scale working model, the conductivity profile can be approximated as

$$\sigma(z) = \sigma_0 \exp(2kz) \quad (1-3)$$

where $(2k)^{-1}$ is called the scale height of conductivity. The accepted values of the scale height vary between 5 and 6 km.

Table 1-2 shows conductivities at different altitudes calculated from (1-3) with different scale heights. Figure 1-3 shows the computed values as compared to the Cole and Pierce profile and other measurements.

(ii) Ionospheric Conductivity Profile

The region above 70 km is called the ionosphere. The ionization sources in this region are different from those in the atmosphere. During daytime, the major source of ionization is the flux of the extremely high

Alt. (km)	δ (ohm ⁻¹ m ⁻¹)	
	(2k) ⁻¹ = 5 km	(2k) ⁻¹ = 6 km
0	3.0×10^{-14}	3.0×10^{-14}
10	2.2×10^{-13}	1.6×10^{-13}
20	1.6×10^{-12}	8.4×10^{-13}
30	1.2×10^{-11}	4.4×10^{-12}
40	8.9×10^{-11}	2.4×10^{-11}
50	6.6×10^{-10}	1.3×10^{-10}
60	4.9×10^{-9}	6.6×10^{-10}
70	3.6×10^{-8}	3.5×10^{-9}

Table 1-2

Computed conductivities of air at different altitudes based on (1-3)

energy solar photons. During nighttime, the major source is the precipitation of magnetospheric particles. In addition, since the electron gyrofrequency becomes comparable to the collisional frequency, magnetic forces have to be taken into consideration. The conductivity of a plasma that has magnetic field lines imbedded in it is no longer isotropic; it is a tensor rather than a scalar,

$$\sigma_z = \begin{pmatrix} \sigma_1 & \sigma_2 & 0 \\ \sigma_2 & \sigma_1 & 0 \\ 0 & 0 & \sigma_0 \end{pmatrix} \quad (1-4)$$

(choosing z to point along the direction of B).

As for a two component plasma (electrons and one species of positive ion):

$$\sigma_1 = \frac{\epsilon_0 \omega_e^2 \nu_e}{\nu_e^2 + \omega_{eH}^2} + \frac{\epsilon_0 \omega_+^2 \nu_+}{\nu_+^2 + \omega_{+H}^2}$$

is called the "Pederson conductivity;"

$$\sigma_2 = - \frac{\epsilon_0 \omega_e^2 \omega_{eH}}{\nu_e^2 + \omega_{eH}^2} + \frac{\epsilon_0 \omega_+^2 \omega_{+H}}{\nu_+^2 + \omega_{+H}^2}$$

is called the "Hall conductivity;" and

$$\sigma_0 = \frac{\epsilon_0 \omega_e^2}{\nu_e} + \frac{\epsilon_0 \omega_+^2}{\nu_+}$$

is the "specific conductivity" where

$\omega_{+H} = e B/m_+$ is the gyrofrequency of ions,

$\omega_+ = N_k e^2/m_+ \epsilon_0$ is the plasma frequency of ions,

ν_+ is the collision frequency for ions

and similarly for ω_{eH} , ω_e and ν_e of electrons.

Calculated values of σ_0 , σ_1 and σ_2 at different altitudes in the ionosphere can be found in detail in the Satellite Environment Handbook (1965). The necessary approximations for field modeling will be discussed in Chapter 3. Figure 1-4 is a sample conductivity profile up to 150 km. Above 150 km, the specific conductivity becomes so large that magnetic field lines can be considered as equipotentials.

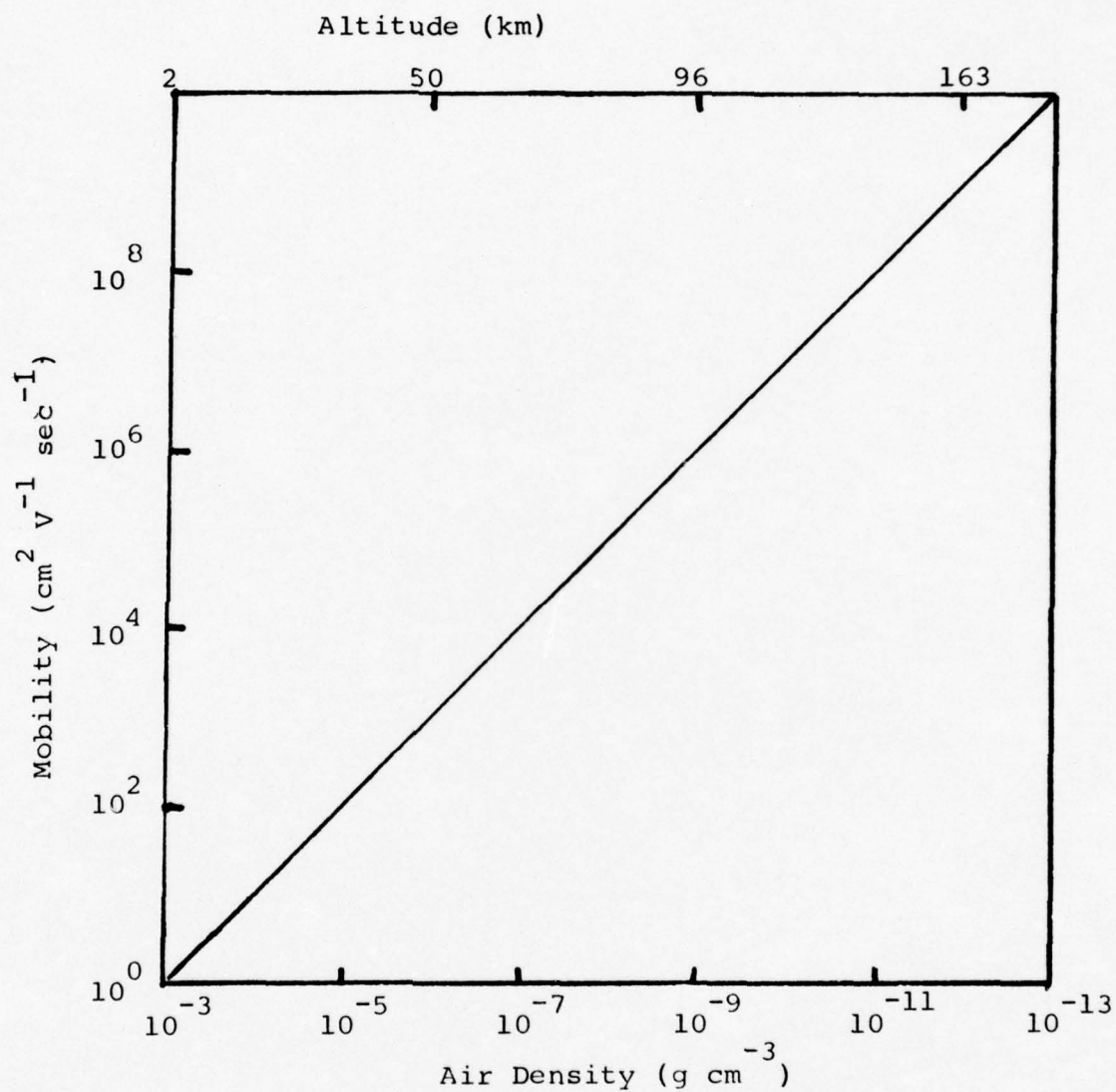


Figure 1-1

Variation of ion mobility k with atmospheric neutral number density
(Sagalyn and Fitzgerald, 1965)

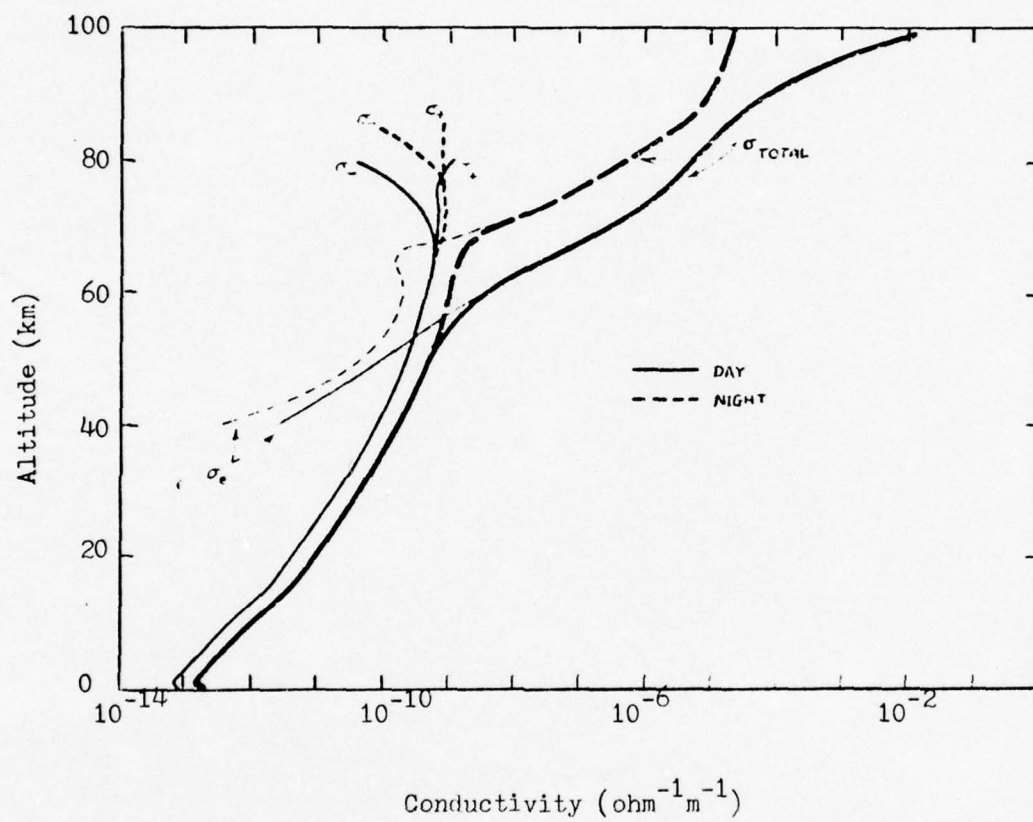


Figure 1-2

Profiles of conductivity versus altitude

Suffixes +, -, and e refer to positive ions,

negative ions, and electrons respectively. (Cole and Pierce, 1965)

In this Figure, δ_e , δ_- and δ_+ are obtained by the measured values of electron and ion concentrations, their effective collisional frequencies and the relation

$$\delta = n e^2 / m \nu$$

where n , e , m , ν are number density, electric charge, mass and collisional frequency respectively. δ_{total} is then the summation of δ_e , δ_+ and δ_- .

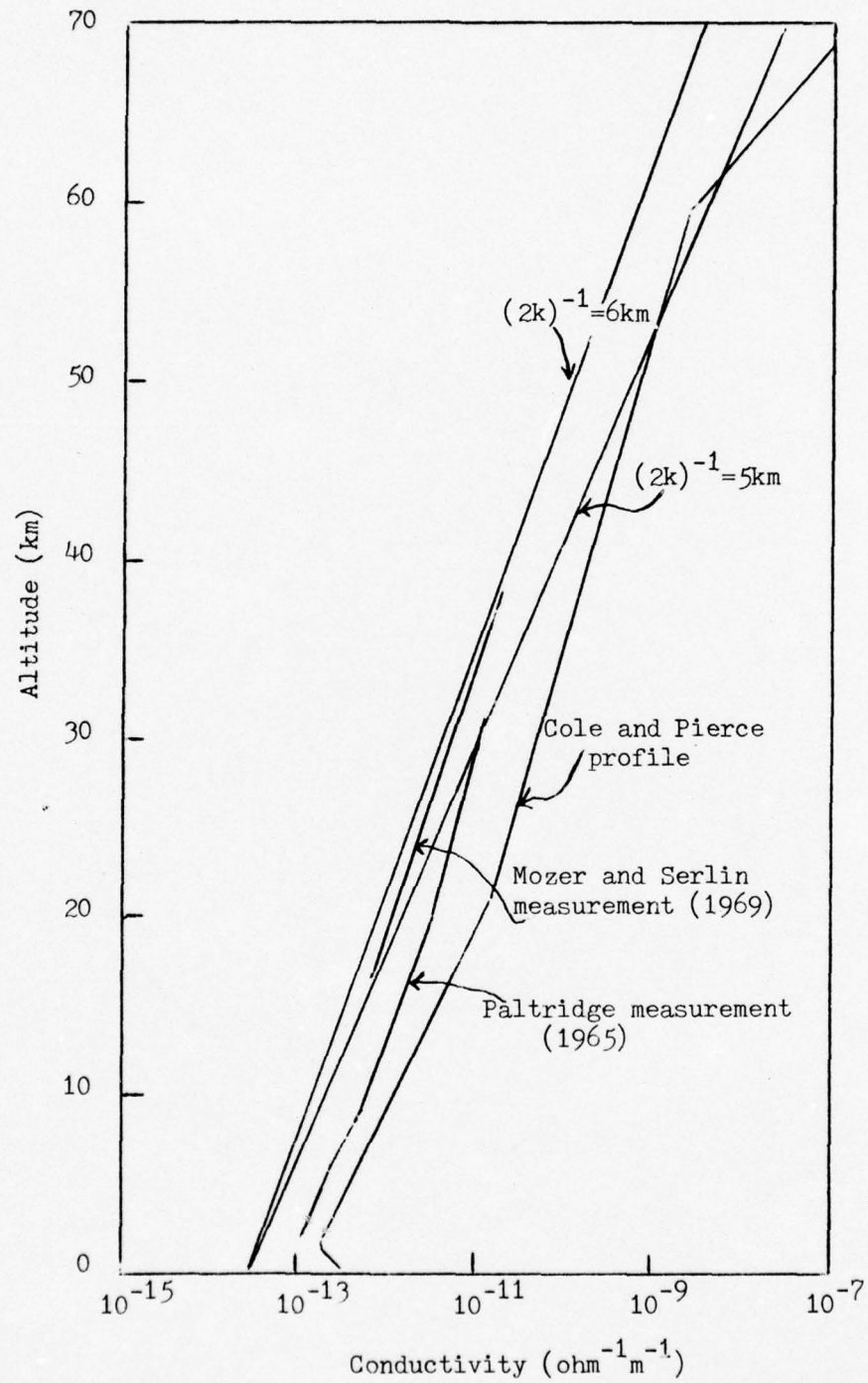


Figure 1-3

Computed values of conductivities as compared with the Cole and Pierce profile (1965) and other measurements by Mozer and Serlin (1969) and Paltridge (1965).

The conductivity of air near ground by Cole and Pierce profile is higher than the average accepted value ($3 \times 10^{-14} \text{ ohm}^{-1} \text{ m}^{-1}$) due to the negligence of the existence of large ions, which are formed as a result of local contamination of the atmosphere and reduce the conductivity near the earth's surface.

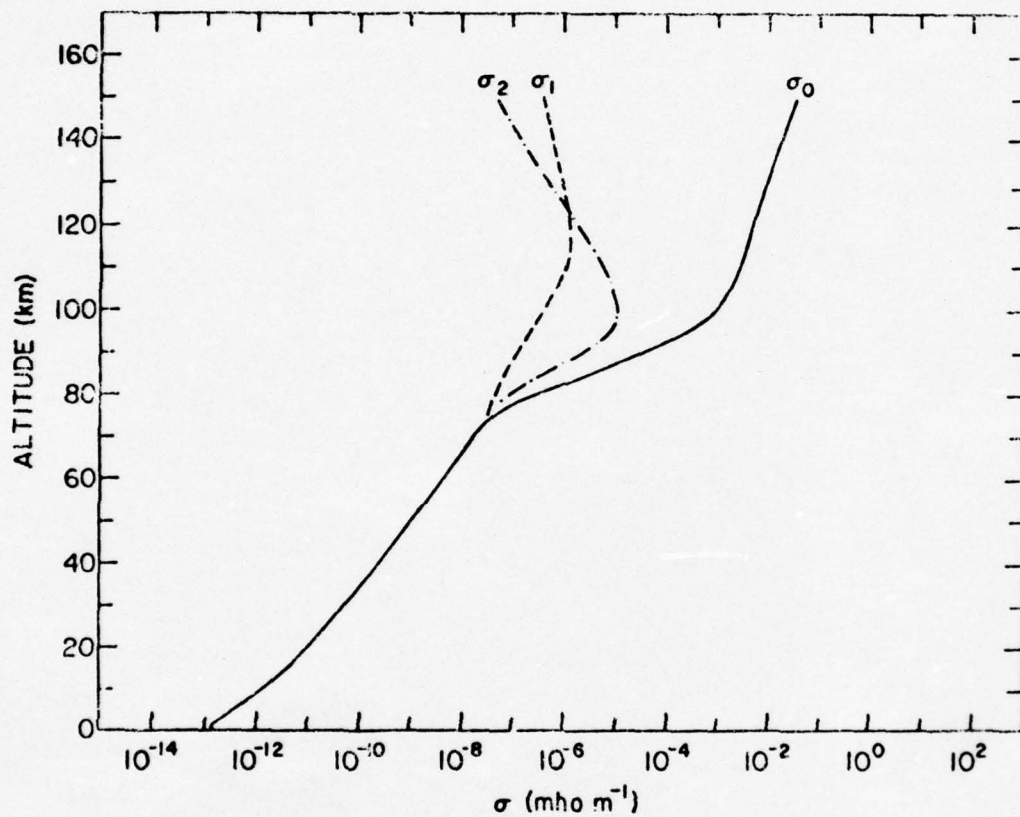


Figure 1-4

A representative conductivity profile with an isotropic (scalar conductivity) region below 70 km and an anisotropic (tensor conductivity) region above.

(Park and Dejnakintra, 1973)

CHAPTER 2

THEORETICAL MODEL OF FIELD MAPPING IN THE ATMOSPHERE

I. Summary of Work in the Past

The purpose of this modeling of atmospheric electric field mapping to different altitudes is three-fold. The general formulation for field mapping is aimed such that:

- (1) it can apply not only to the atmosphere but also to the ionosphere,
- (2) it can be used for both fair weather and disturbed weather conditions,
and
- (3) it should be possible to consider different geometries of charge sources for thunderstorm field mapping. For example, in a thundercloud model, simple point charge sources (monopole, dipole, etc.) are sufficient for examining field variations at large distances. However, disc, cylinder or other shapes of charge sources need to be used in order to study near-by field changes.

The research of large scale mapping of atmospheric electric field that considered the variational property of air conductivity, i.e., the conductivity increases with altitude in an exponential manner, can be summarized by the following representative papers:

- (1) Holzer and Saxon (1952) and Anderson and Freier (1969). Holzer and Saxon were the first ones who employed the property of exponentially increasing conductivity of air to calculate the electric field and conduction currents at different distances due to a simpler dipolar

thundercloud. Anderson and Freier added in possible time variation on potential changes. However, their calculations were limited to the atmosphere; in other words, the range of validity does not extend into the ionosphere where the conductivity is of a tensor form rather than a scalar.

- (2) Park and Dejnakarindra (1973). The mapping of thundercloud electric field at middle and higher latitudes was investigated as a three-dimensional boundary problem. The electrical conductivity was represented by several piecewise exponential functions of altitude, and the anisotropy of air was taken into account above 70 km. The geomagnetic field lines were assumed to be straight and vertical below 150 km in the regions considered. They derived solutions for both the atmosphere and ionosphere but did not achieve an analytic solution. As a result, involved numerical integrations had to be used. Furthermore, the results were good only for point charge sources.

II. Basic Equations

Assuming an exponential increase in conductivity with respect to altitude, the basic equations governing electric field in the atmosphere are the following ((2-1)-(2-5)):

$$\sigma_z = \sigma_0 \exp(2kz) \quad (2-1)$$

$$\vec{\nabla} \times \vec{E} = 0 \quad \text{or} \quad \vec{E} = -\vec{\nabla}\phi \quad (2-2)$$

where σ_e and σ_0 are conductivities of air at altitude z and ground

respectively, $(2k)^{-1}$ is the scale height of conductivity, E is the electric field intensity in the air and Φ is the electric potential with respect to the earth surface.

In steady state conditions $\vec{\nabla} \cdot \vec{j}_{\text{total}} = 0$ where $j_{\text{total}} = j_a + j_s$, the summation of current density in the air and that at the source region due to convection. We then have

$$\vec{j}_a = \sigma \vec{E} \quad (2-3)$$

and

$$\vec{\nabla} \cdot \vec{j}_{\text{total}} = 0 \quad \text{or} \quad \vec{\nabla} \cdot \vec{j}_a = -\vec{\nabla} \cdot \vec{j}_s \quad (2-4)$$

And Poisson's equation is

$$\vec{\nabla} \cdot \vec{E} = \rho / \epsilon_0 \quad \text{or} \quad \nabla^2 \Phi = -\rho / \epsilon_0 \quad (2-5)$$

where ρ is the space charge density and ϵ_0 is the permittivity of air.

Combination of (2-1), (2-2), (2-3), (2-4) gives

$$\sigma_z \left(\nabla^2 + 2k \frac{\partial}{\partial z} \right) \Phi = \vec{\nabla} \cdot \vec{j}_s. \quad (2-6)$$

Substituting (2-5) into (2-6), we obtain

$$\rho = 2k\epsilon_0 \frac{\partial \Phi}{\partial z} - \frac{\epsilon_0}{\sigma_z} \vec{\nabla} \cdot \vec{j}_s. \quad (2-7)$$

The first term is space charge in the air

$$\rho_{\text{air}} = 2k\epsilon_0 \frac{\partial \Phi}{\partial z}. \quad (2-8)$$

The second term is zero everywhere else except at the source of charge such that

$$\rho_{\text{source}} = - \frac{\epsilon_0}{\sigma_z} \vec{\nabla} \cdot \vec{j}_s. \quad (2-9)$$

From (2-6) and (2-9) we then obtain the potential equation as

$$\left[\nabla^2 + 2k \frac{\partial}{\partial z} \right] \Phi = - \frac{f}{\epsilon_0} \quad (2-10)$$

where f is a known source distribution (ρ_{source}).

For fair weather condition (i.e., without a charge source), the potential equation is simply

$$\left[\nabla^2 + 2k \frac{\partial}{\partial z} \right] \Phi = 0. \quad (2-11)$$

III. Fair Weather Fields

In order to solve equation (2-11), we first write out the boundary conditions as:

$$\Phi = V_0 \quad \text{at } z = H, \text{ and}$$

$$\Phi = 0 \quad \text{at } z = 0.$$

where H is the upper boundary of the atmosphere and V_0 is the total potential difference between the top of the atmosphere and the earth surface.

The solution for the potential V at any altitude in the atmosphere is simply

$$V = V_0 \left(\frac{1 - e^{-2kz}}{1 - e^{-2kH}} \right). \quad (2-12)$$

The electric field is calculated from $\vec{E} = -\nabla V$ such that

$$\begin{aligned} E_x &= 0, \\ E_y &= 0, \text{ and} \\ E_z &= - \left(\frac{V_0 \cdot 2k}{1 - e^{-2kH}} \right). \end{aligned}$$

Only the vertical component exists and it is in the downward direction.

$$\text{Defining } E_0 \equiv - \frac{V_0 \cdot 2k}{1 - e^{-2kH}} \text{ as the field intensity near the ground,}$$

we obtain

$$E_z = E_0 e^{-2kH} \quad (2-13)$$

the same result obtained by Holzer and Saxon (1952) and Mozer (1971).

The average observed values of E_0 over land is about 130 volts/m under fair weather conditions. Based on this value, Table 2-1 gives the expected field intensities and potentials with respect to ground at different altitudes. The Table also shows the difference between the classical picture of spherical capacitor and the more recent model of a leaky capacitor. In the classical picture, the field would fall off to zero at the top of the atmosphere (50-70 km). However, the new model allows 0.1 mV/m to 1 mV/m of field at 70 km during fair weather which is in the same order of magnitude as fields of magnetospheric origins. During disturbed weather conditions, more pronounced fields will be observed.

Figure 2-1 is a comparison between calculated values and the observed ground and airborne averages during fair weather.

Alt. (km)	E (Volts/m)		(Volts)	
	$(2k)^{-1}=5km$	$(2k)^{-1}=6km$	$(2k)^{-1}=5km$	$(2k)^{-1}=6km$
0	1.3×10^2	1.3×10^2	0	0
10	1.8×10^1	2.5×10^1	5.60×10^5	6.33×10^5
20	2.4×10^0	4.6×10^0	6.38×10^5	7.52×10^5
30	3.2×10^{-1}	8.8×10^{-1}	6.48×10^5	7.74×10^5
40	4.4×10^{-2}	1.7×10^{-1}	6.50×10^5	7.79×10^5
50	5.9×10^{-3}	3.1×10^{-2}	6.50×10^5	7.80×10^5
60	8.0×10^{-4}	5.9×10^{-3}	6.50×10^5	7.80×10^5
70	1.1×10^{-4}	1.1×10^{-3}	6.50×10^5	7.80×10^5

Table 2-1

Electric Fields and Potential at different altitudes
in fair weather computed from (2-13) and (2-12)

IV. Solution for Thunderstorm Fields

The potential equation for thunderstorm conditions, when there is additional charge source in the air, is

$$\left(\nabla^2 + 2k \frac{\partial}{\partial z} \right) \phi = - \frac{f}{\epsilon_0} \quad (2-10)$$

The solution of equation (2-10) is complicated by the fact that the charge distribution is spread over a finite volume. In solving differential equations such as (2-10) with either Dirichlet or Nuemann boundary condition the Green's function method is both elegant and effective. The Green's function is the solution of the potential for a point source. The principle of superposition allows us to calculate the potential for the actual source distribution.

The first step in solving (2-10) is to generate a Green's function for the equation. Assuming azimuthal symmetry, the Green's function depends on $(r, z; r', z')$ and satisfies the equation

$$\left[\nabla^2 + 2k \frac{\partial}{\partial z} \right] G = - \frac{1}{\epsilon_0} \delta(\vec{x} - \vec{x}') \quad (2-10')$$

The solution of (2-10) is then

$$\phi(r, z) = \int_{\tau'(\text{volume})} G(r, z; r', z') f(r', z') d\tau'$$

in infinite space with no boundary surfaces.

To find G we consider the Fourier transform of both sides of (2-10'). The delta function on the right has the representation,

$$\delta(\vec{x} - \vec{x}') = \frac{1}{(2\pi)^3} \int d\kappa_z d\phi \kappa_r d\kappa_r e^{i\kappa_z(z-z')} e^{i\kappa_r \cdot (\vec{r} - \vec{r}')}$$

in cylindrical coordinates. Therefore

$$G(r, z; r', z') = \iiint d\kappa_z d\phi \kappa_r d\kappa_r g(\kappa_r, \kappa_z) e^{i\kappa_z(z-z')} e^{i\kappa_r \cdot (\vec{r}-\vec{r}')} \quad (2-13)$$

The Fourier transform $g(\kappa_r, \kappa_z)$ is to be determined. Substituting (2-13) into (2-10') gives

$$\begin{aligned} & \iiint d\kappa_z d\phi \kappa_r d\kappa_r g(\kappa_r, \kappa_z) (-\kappa_r^2, -\kappa_z^2 + 2ik \kappa_z) e^{i\kappa_z(z-z')} e^{i\kappa_r \cdot (\vec{r}-\vec{r}')} \\ &= \iiint -\frac{1}{\epsilon_0 (2\pi)^3} d\kappa_z d\phi \kappa_r d\kappa_r e^{i\kappa_z(z-z')} e^{i\kappa_r \cdot (\vec{r}-\vec{r}')} \end{aligned} \quad (2-14)$$

By comparing both sides of (2-14) we get

$$g(\kappa_r, \kappa_z) = \frac{1}{\epsilon_0 (2\pi)^3} [\kappa_r^2 + \kappa_z^2 - 2ik \kappa_z]^{-1} \quad (2-15)$$

Substitute (2-15) back into (2-13):

$$G(r, z; r', z') = \frac{1}{\epsilon_0 (2\pi)^3} \iiint d\kappa_z d\phi d\kappa_r \kappa_r \frac{e^{i\kappa_z(z-z')} e^{i\kappa_r \cdot (\vec{r}-\vec{r}')}}{\kappa_z^2 + \kappa_r^2 - 2ik \kappa_z} \quad (2-16)$$

by using the relation

$$\begin{aligned} e^{i\kappa_r \cdot (\vec{r}-\vec{r}')} &= e^{i\kappa_r |r-r'| \cos \phi} \\ &= \sum_{m=-\infty}^{\infty} i^m e^{im} J_m(\kappa_r |r-r'|) \end{aligned} \quad (2-17)$$

which can be proved separately ($J_m()$ is the Bessel function of first kind of m^{th} order).

G then becomes

$$G(r, z; r', z') = \frac{1}{\epsilon_0 (2\pi)^2} \int_{-\infty}^{\infty} \int_0^{\infty} d\kappa_z \kappa_r d\kappa_r \frac{e^{i\kappa_z(z-z')}}{(\kappa_z^2 + \kappa_r^2 - 2ik \kappa_z)} J_0(\kappa_r |\vec{r}-\vec{r}'|) \quad (2-18)$$

since after integration over ϕ only $m = 0$ term survives.

The poles of equation (2-18) are found at

$$\kappa_z = i \left[k \pm \sqrt{k^2 + \kappa_r^2} \right] \quad (2-19)$$

as shown in Figure 2-2. There are two possible contours, one in the upper half plane and the other in the lower half plane.

In order to make G vanish at $z \rightarrow \infty$, we choose the contour closing in the upper half plane.

$$\begin{aligned} G(r, z; r', z') &= \frac{1}{4\pi^2 \epsilon_0} \int_{-\infty}^{\infty} \int_0^{\infty} d\kappa_z \kappa_r d\kappa_r \frac{e^{i\kappa_z(z-z')} J_0(\kappa_r |\vec{r}-\vec{r}'|)}{\left[\kappa_z - ik \left(1 + \sqrt{1 + \frac{\kappa_r^2}{k^2}} \right) \right] \left[\kappa_z - ik \left(1 - \sqrt{1 + \frac{\kappa_r^2}{k^2}} \right) \right]} \\ &= \frac{2\pi i}{4\pi^2 \epsilon_0} \int_0^{\infty} \frac{\kappa_r J_0(\kappa_r |\vec{r}-\vec{r}'|) e^{-[k + \sqrt{k^2 + \kappa_r^2}](z-z')}}{2i\sqrt{k^2 + \kappa_r^2}} d\kappa_r \\ &= \frac{1}{4\pi \epsilon_0} \int_0^{\infty} \frac{\kappa_r J_0(\kappa_r |\vec{r}-\vec{r}'|) e^{-[k + \sqrt{k^2 + \kappa_r^2}](z-z')}}{\sqrt{k^2 + \kappa_r^2}} d\kappa_r \end{aligned} \quad (2-20)$$

Gradshteyn and Ryzhik (1965, 6.616) gives

$$\int_1^{\infty} J_0(r\sqrt{m'^2 - 1}) \exp(-zm') dm' = \frac{\exp(-\sqrt{r^2 + z^2})}{\sqrt{r^2 + z^2}} \quad (2-21)$$

With proper substitution, (2-20) becomes

$$G(r, z; r', z') = \frac{1}{4\pi\epsilon_0} e^{-k(z-z')} \frac{e^{-k\sqrt{|\vec{r}-\vec{r}'|^2 + (z-z')^2}}}{\sqrt{|\vec{r}-\vec{r}'|^2 + (z-z')^2}} \quad (2-22)$$

Substitute (2-22) back into (2-12):

$$\Phi(r, z) = \frac{1}{4\pi\epsilon_0} \int_{\tau'} f(r', z') e^{-k(z-z')} \frac{e^{-k\sqrt{|\vec{r}-\vec{r}'|^2 + (z-z')^2}}}{\sqrt{|\vec{r}-\vec{r}'|^2 + (z-z')^2}} d\tau' \quad (2-23)$$

where $f(r', z')$ is the source function and

$$d\tau' = r' dr' d\phi' dz'$$

is the volume element in cylindrical coordinates.

With (2-23), we are now ready to solve different potential problems in the atmosphere.

The mathematics references of this section are: for Green's function method, Jackson (1966), Chapters 3 and 6; for properties of Bessel functions and contour integration, Hilderbrand (1955), Chapters 4 and 9 respectively.

V. Different Charge Sources

It is currently accepted that a thundercloud consists of two portions of approximately equal and opposite charges of electricity, the upper part being positively charged and the lower part negatively charged. The charge separation mechanism (or mechanisms) is not well understood yet. This dipolar structure will change the electric field intensity both above and below the cloud. The sign and magnitude of the charge depend on the relative

position of the observer (Chalmers, 1967). Furthermore, there have also been observations and studies on the shielding layer around the cloud boundary which will be discussed in Chapter 4.

The simplest approximations for the charge distribution inside thunderclouds include (1) point approximation and (2) thin disc approximation illustrated in Figure 2-3. Their respective range of validity will also be discussed. For charge distribution of a thick disc, cylinder or other shape, the solution can be obtained by integration (summation) over contributions of points or thin discs.

The first step in solving the potential and electric field problem is to write the source function. For a point charge q_i at $r = 0$ and $z = z_i$, the source function can be written as

$$f_i(r', z') = \frac{q_i}{2\pi r'} \delta(r') \delta(z' - z_i) \quad (2-24)$$

such that the potential above the source is

$$\begin{aligned} \phi_i(r, z) &= \frac{1}{4\pi\epsilon_0} \int_{z'=0}^{\infty} \int_{r'=0}^{\infty} \int_{\phi'=0}^{2\pi} \frac{q_i}{2\pi r'} \\ &\quad \frac{\delta(r') \delta(z' - z_i) e^{-k(z-z')} e^{-k\sqrt{(z-z')^2 + |r-r'|^2}}}{\sqrt{|r-r'|^2 + (z-z')^2}} r' dr' d\phi' dz' \\ &= \frac{q}{4\pi\epsilon_0} \frac{e^{-k(z-z_i)} e^{-k\sqrt{r^2 + (z-z_i)^2}}}{\sqrt{r^2 + (z-z_i)^2}} \end{aligned} \quad (2-25)$$

The boundary condition requires that $\phi = 0$ at $z = 0$, so the image charge is introduced which gives

$$\Phi_i(r, z) = \frac{q_i}{4\pi\epsilon_0} e^{-k(z-z_i)} \left[\frac{e^{-k\sqrt{r^2+(z-z_i)^2}}}{\sqrt{r^2+(z-z_i)^2}} + \frac{e^{-k\sqrt{r^2+(z+z_i)^2}}}{\sqrt{r^2+(z+z_i)^2}} \right] \quad (2-26)$$

such that the vertical and horizontal fields are

$$E_{iz} = \frac{1}{4\pi\epsilon_0} \sum_{n=1}^2 \frac{q_n}{R_n} \left(\frac{\Delta z_n}{R_n} + k(R_n + \Delta z_n) \right) \exp \left(-k(R_n + \Delta z_n) \right) \quad (2-27)$$

$$E_{iH} = \frac{1}{4\pi\epsilon_0} \sum_{n=1}^2 \frac{q_n \cdot r}{R_n^2} \left(\frac{1}{R_n} + k \right) \exp \left(-k(R_n + \Delta z_n) \right) \quad (2-28)$$

where $n = 1$ and 2 refer to the charge and image charge respectively such that

$$q_1 = q_2 = q_i$$

$$R_1 = \sqrt{r^2 + (z - z_i)^2},$$

$$R_2 = \sqrt{r^2 + (z + z_i)^2},$$

$$\Delta z_1 = z - z_i$$

$$\Delta z_2 = z + z_i.$$

The potential problem for a point charge source can also be solved by finding the solution of Laplace's equation in cylindrical coordinates with appropriate boundary conditions. However, this method, because it does not apply to other different geometrical shapes of charge sources, is not as handy as the Green's function method. The procedure is shown in the Mathematical Appendix for comparison.

For a dipolar structure of a thundercloud with q_1 at z_1 and $-q_2$ at z_2 , the total field change is simply the vector sum of changes due

to individual charges.

$$\Phi = \sum_i \Phi_i, \text{ and}$$

$$E = \sum_i E_i.$$

Consider a case of typical thundercloud with +20 Coul at 6 km and -20 Coul at 4 km. Table 2-2 shows a comparison of the electric fields that would be observed using this model with the property of variant conductivity taken into consideration and the "classical" method assuming uniform conductivity (Coulomb field).

It is shown that the electric field above the source drops much faster with distance as compared with the classical method. They differ by a factor of 10 when the observer is 24 km overhead above the cloud, over 100 when 39 km above and 1000 when 53 km away.

Figures 2-4 and 2-5 are the calculated vertical profiles for E_z and E_H , overhead and at horizontal distances of 20 km, 50 km and 100 km. It is seen that the electric field decreases much slower at larger horizontal distances. For example, the vertical fields at $r = 0$ and $r = 100$ km differ by eight orders of magnitude when observed at an altitude of 10 km (4 km vertically from the cloud in this case), but at 70 km, they only differ by three orders of magnitude. It is also shown that even for a moderately charged thundercloud as considered in this case (recent works have observed up to several hundred coulombs of charge inside one cell) the change in the E field at the top of the atmosphere can still be detected. It is in the order of millivolts per meter within a horizontal range of 50 km, comparable to fields of ionospheric origins.

Alt (km)	E_z (V/m) (present model)	E_z (V/m) (Coulomb field)	Ratio E_z present: E_z Coulomb
10	6.0×10^{-3}	6.6×10^{-3}	1:1.1
15	5.3×10^{-2}	8.5×10^{-2}	1:1.6
20	9.7×10^{-1}	2.7×10^{-2}	1:2.8
25	2.3×10^{-1}	1.2×10^{-2}	1:5.2
30	6.2×10^0	6.5×10^{-1}	1:10.5
35	1.8×10^0	3.9×10^{-1}	1:22
40	5.3×10^{-1}	2.5×10^{-1}	1:48
50	5.2×10^{-2}	1.3×10^{-1}	1:240
55	1.7×10^{-2}	8.8×10^0	1:654
60	5.6×10^{-3}	7.2×10^0	1:1281
65	1.8×10^{-3}	5.6×10^0	1:3031
67	1.2×10^{-3}	5.1×10^0	1:4283

Table 2-2

Comparison of E_z between using the present model
 ((2-27) with $(2k)^{-1} = 5\text{km}$) and the Coulomb field
 calculation $((2k)^{-1} = \infty)$

The same technique can also be employed to find the potential and electric field at different altitudes for the case of thin disc charge distribution instead of point charge source. This disc distribution of charge is similar to that suggested by MacGorman and Few (1975). Assume the $r = 0$ axis is defined to be along the center axis of the uniformly charged disc, the source function can be written as

$$f_i(r', z') = \alpha' \delta(z' - z_i) \quad (2-28)$$

where α' is the surface charge density and z_i is the height of disc.

The potential can then be written as

$$\begin{aligned} \Phi(r, z) &= \int_{r'=0}^a \int_{\phi'=0}^{2\pi} \int_{z'=0}^{\infty} \frac{\alpha' \delta(z' - z_i)}{4\pi\epsilon_0} e^{-k(z-z')} \frac{e^{-k\sqrt{r^2+r'^2-2rr'\cos\phi'+(z-z')^2}}}{\sqrt{r^2+r'^2-2rr'\cos\phi'+(z-z')^2}} \\ &\quad r' dr' d\phi' dz' \\ &= \int_{r'=0}^a \int_{\phi'=0}^{2\pi} \frac{\alpha' e^{-k(z-z_i)} e^{-k\sqrt{r^2+r'^2-2rr'\cos\phi'+(z-z_i)^2}}}{4\pi\epsilon_0 \sqrt{r^2+r'^2-2rr'\cos\phi'+(z-z_i)^2}} r' dr' d\phi' \quad (2-29) \end{aligned}$$

plus the image term, where a is the radius of the disc such that $q = \pi a^2 \alpha$.

In order to compare field changes due to point and disc charge sources, it is only necessary to compare the vertical fields along the $r = 0$ axis where the difference is the greatest. For a point source, from (2-26):

$$\left. \Phi_i(z) \right|_{r=0} = \frac{q_i}{4\pi\epsilon_0} e^{-k(z-z_i)} \left[\frac{e^{-k(z-z_i)}}{z-z_i} + \frac{e^{-k(z+z_i)}}{z+z_i} \right] \quad (2-30)$$

such that

$$E_{iz} \Big|_{r=0} = \frac{q}{4\pi\epsilon_0} \cdot \frac{e^{-2k(z-z_i)}}{(z-z_i)^2} \cdot (1 + 2k(z-z_i))$$

+ image term. (2-31)

For a disc charge source, from (2-29)

$$\Phi_i(z) \Big|_{r=0} = \frac{q \cdot 2\pi}{4\pi\epsilon_0 \cdot \pi a^2} e^{-k(z-z_i)} \int_{r'=0}^a \frac{e^{-k\sqrt{r'^2+(z-z_i)^2}}}{\sqrt{r'^2+(z-z_i)^2}} r' dr'$$

+ image term,

$$= \frac{q}{2\pi\epsilon_0 a^2} \left[e^{-2k(z-z_i)} - e^{-k\sqrt{a^2+(z-z_i)^2}+(z-z_i)} \right]$$

+ image term, (2-32)

such that

$$E_{iz} \Big|_{r=0} = \frac{q}{2\pi\epsilon_0 a^2} \left[2e^{-2k(z-z_i)} - \left(1 + \frac{z-z_i}{\sqrt{a^2+(z-z_i)^2}} \right) e^{-k\sqrt{a^2+(z-z_i)^2}+(z-z_i)} \right]$$

+ image term. (2-33)

Table 2-3 shows field changes due to disc charge sources as compared to point charge sources. The heights of different charges are the same as before; 20 Coul at 6 km and -20 Coul at 4 km. Different radii of $r=2$ km and $r=5$ km for the disc are used as representative sizes of a small and medium-large cell respectively.

From these calculations, it is indicated that the disc model is only necessary when calculating fields near the cloud. For a 5 km radius cell,

-33-

the difference drops to 10% at 22 km (16 km away) and for a small cell it only differs by 1-2%.

Alt. (km)	$E_z r=0$ (V/m) point	$E_z r=0$ (V/m) a=2km	Ratio: $\frac{E_{\text{point}}}{E_{a=2\text{km}}}$	$E_z r=0$ (V/m) a=5km	Ratio: $\frac{E_{\text{point}}}{E_{a=5\text{km}}}$
7	1.64×10^5	4.08×10^4	4.01	7.81×10^3	20.99
10	6.02×10^3	4.93×10^3	1.22	2.53×10^3	2.38
15	5.29×10^2	5.05×10^2	1.05	4.09×10^2	1.29
20	9.74×10^1	9.54×10^1	1.02	8.61×10^1	1.13
30	6.16×10^0	6.11×10^0	1.01	5.85×10^0	1.05
40	5.31×10^{-1}	5.29×10^{-1}	1.01	5.15×10^{-1}	1.03
50	5.24×10^{-2}	5.22×10^{-2}	1.00	5.12×10^{-2}	1.02

Table 2-3

Comparison of field changes due to disc charge sources
(2-33) and point charge sources (2-31)
(The charge distribution is 20 Coul at 6 km and
-20 Coul at 4 km.)

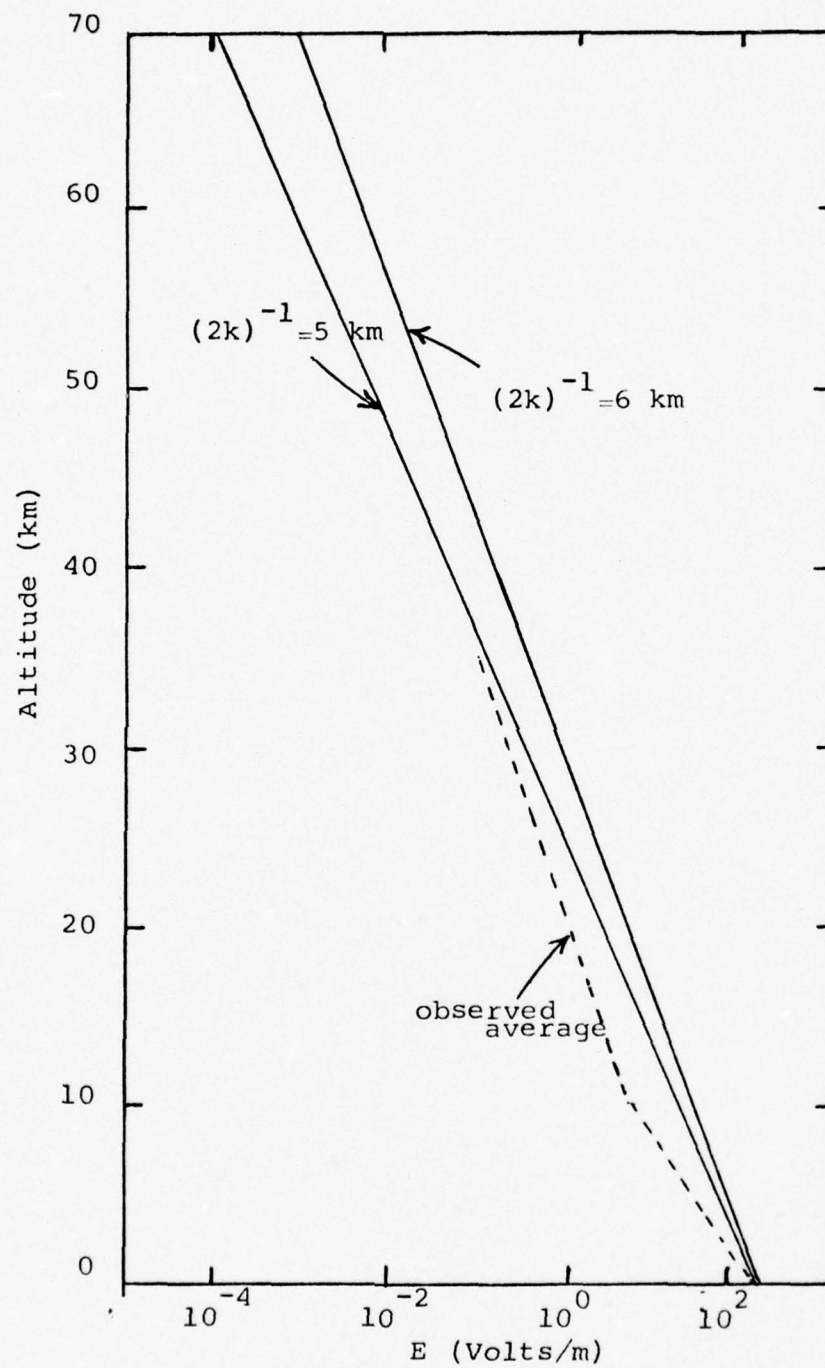


Figure 2-1

Computed and observed dependences
of electric field strength on height

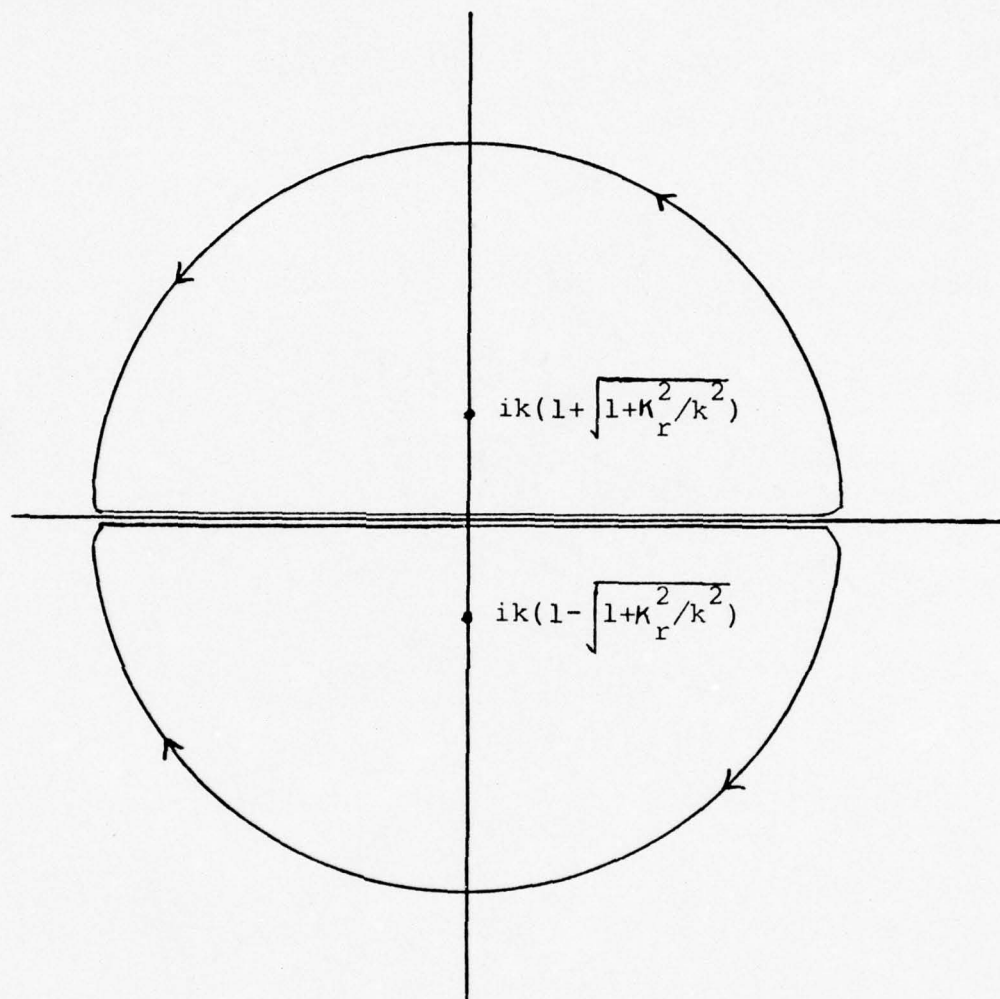


Figure 2-2
The complex κ_z plane

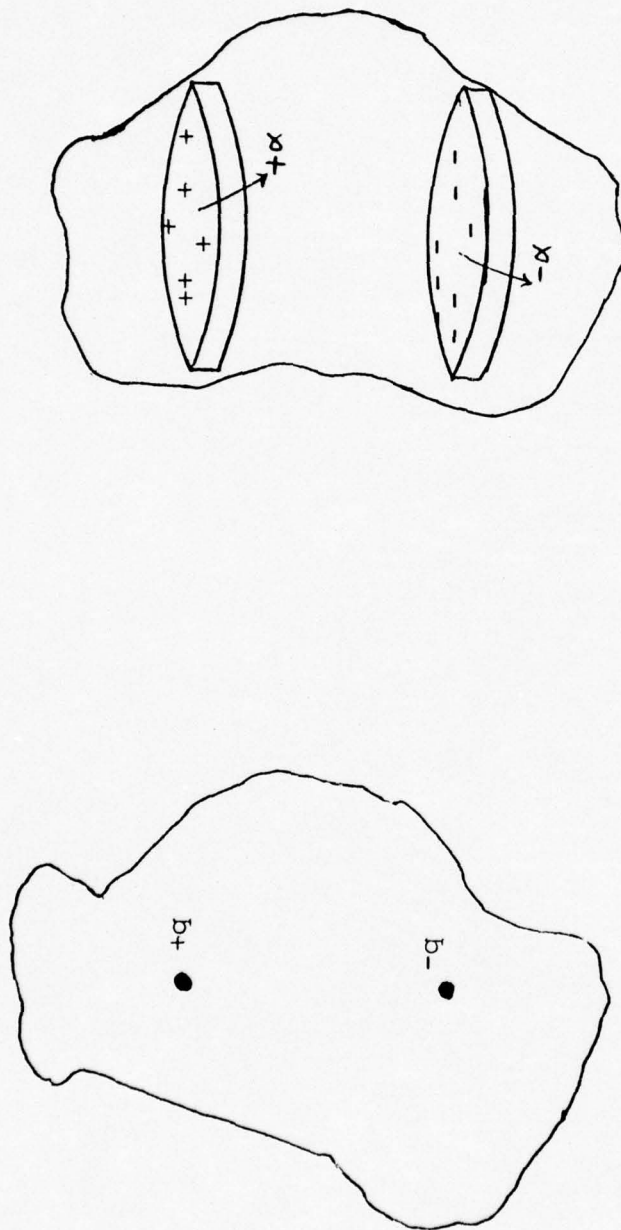


Figure 2-3

Charge models for a dipolar thundercloud

(a) point approximation

(b) thin disc approximation
 $(\pm \alpha \pi a^2 = \pm q)$

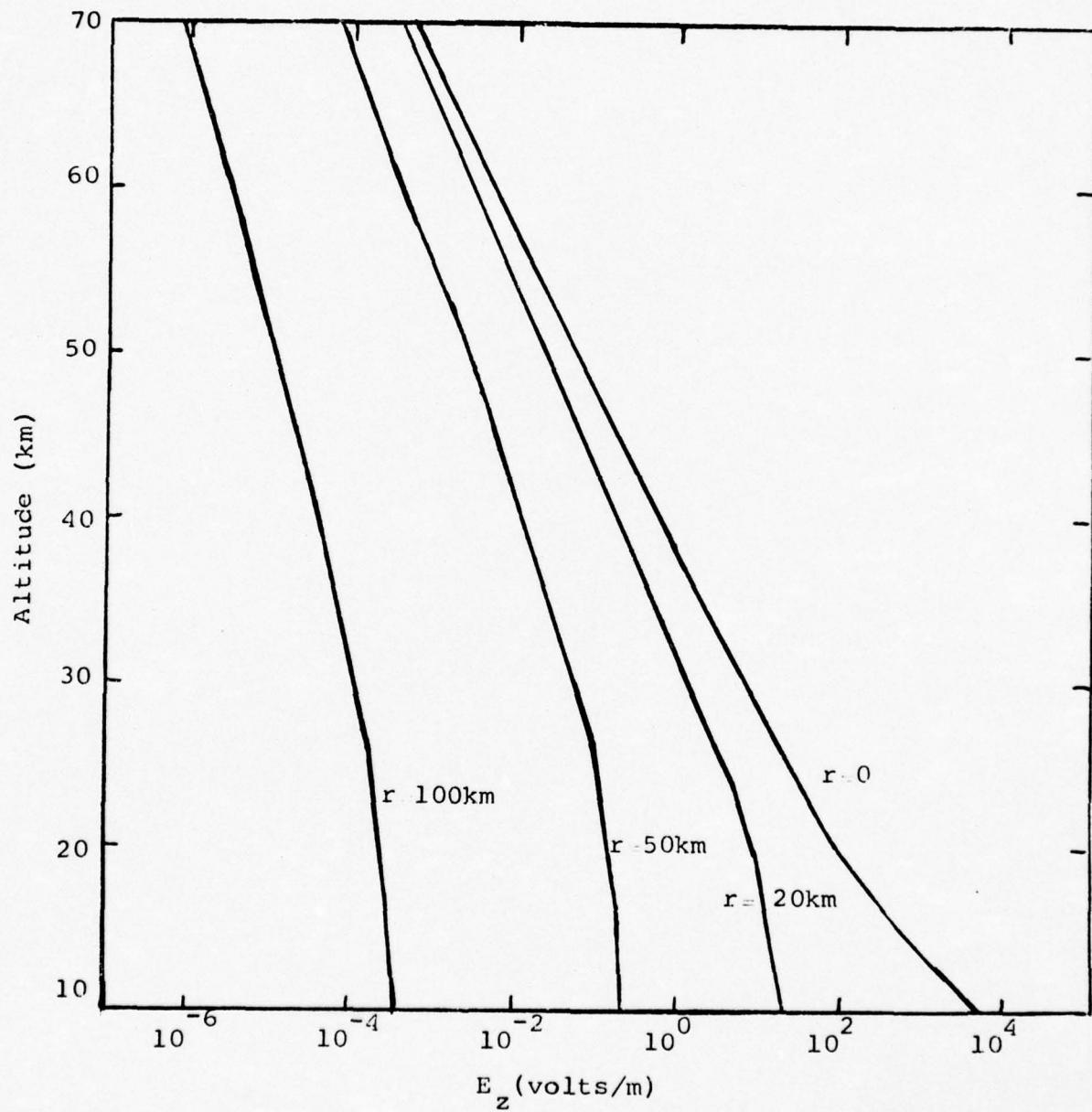


Figure 2-4

Calculated verticle profile for vertical electric field E_z at different horizontal distances. The source is an electric dipole thundercloud of 20 C at 6 km and -20 C at 4 km.

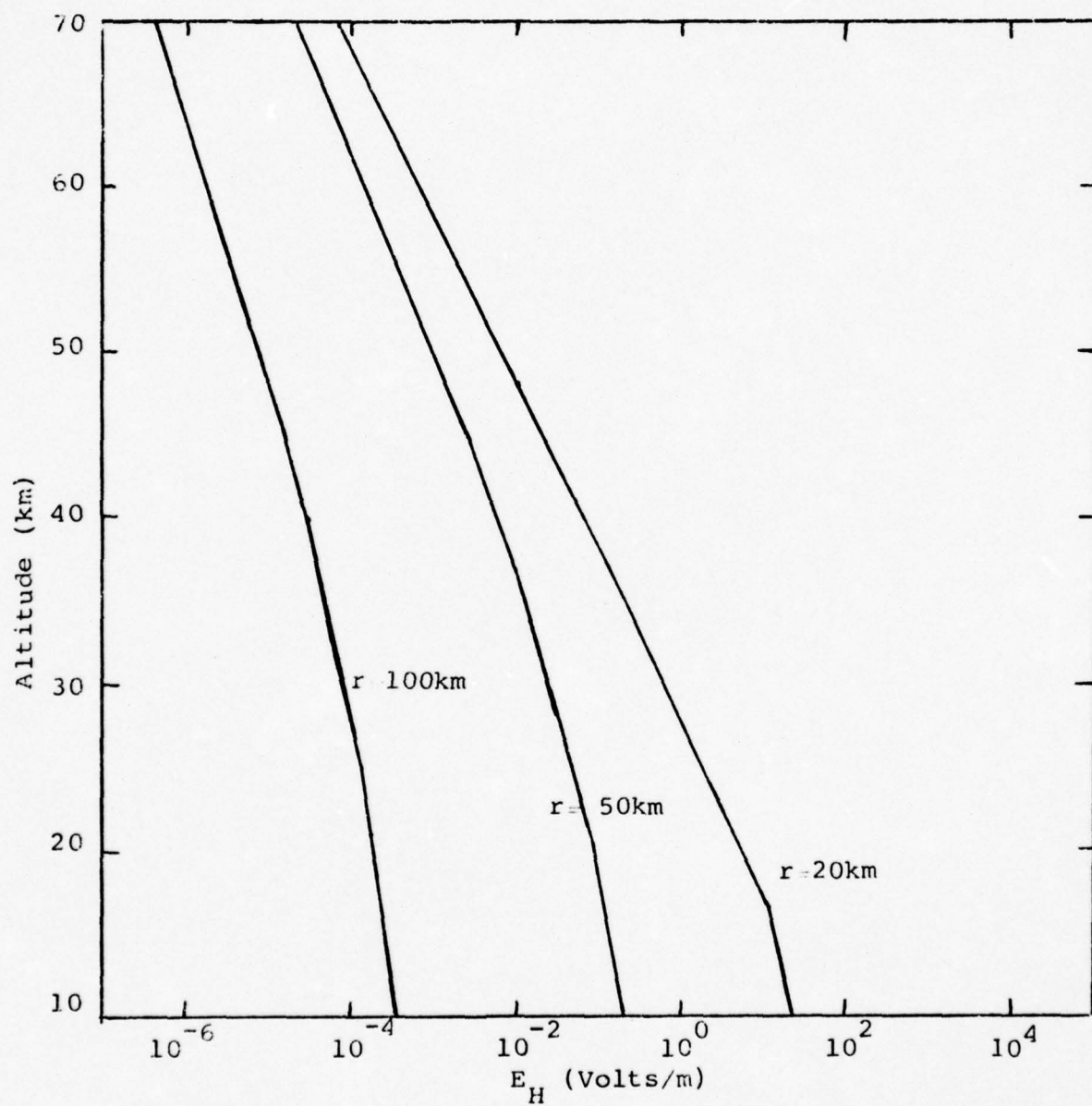


Figure 2-5

Calculated vertical profile for horizontal electric fields E_H at different horizontal distances. The assumed source is a dipole thundercloud of 20 C at 6 km and - 20 C at 4 km.

CHAPTER 3

ATMOSPHERIC FIELDS MAPPED INTO THE IONOSPHERE

I. Theory and Solution without Boundary Conditions

In Chapter 2, the mapping problem of atmospheric electric fields within the atmosphere was extensively discussed. The upper boundary of the atmosphere was assumed to be at the altitude of 70 km. Yet beyond that, there is still another exciting game for "atmospheric electricians" to play instead of working with a classical non-permissive shielding layer which prevents electrical interactions between the atmosphere and ionosphere.

Beyond 70 km, the conductivity of air becomes a tensor as shown in (1-4) instead of a scalar as is the case for the atmosphere. All the other electric equations stay practically the same. The basic equations between 70 km and 150 km are thus:

$$\underline{\underline{\sigma}} = \begin{pmatrix} \sigma_1 & -\sigma_2 & 0 \\ \sigma_2 & \sigma_1 & 0 \\ 0 & 0 & \sigma_0 \end{pmatrix} \quad (3-1)$$

(z-axis is along \vec{B})

$$\vec{\nabla} \times \vec{E} = 0 \quad \text{or} \quad \vec{E} = -\vec{\nabla}\phi \quad (3-2)$$

$$\vec{j}_a = \underline{\underline{\sigma}} \cdot \vec{E} \quad \text{or} \quad \sum_{i=x,y,z} \left(\sum_{j=x,y,z} \sigma_{ij} E_j \right) \hat{i} \quad (3-3)$$

$$\vec{\nabla} \cdot \vec{j}_a = -\vec{\nabla} \cdot \vec{j}_s \quad (3-4)$$

$$\vec{\nabla} \cdot \vec{E} = \frac{\rho}{\epsilon_0} \quad \text{or} \quad \nabla^2 \phi = -\frac{\rho}{\epsilon_0} \quad (3-5)$$

Following the same steps as in Chapter 2 we can solve the potential problem in the lower ionosphere.

Combination of (3-1), (3-2), (3-3) and (3-4) gives

$$\sigma_1 \left(\frac{\partial^2 \Phi}{\partial x^2} + \frac{\partial^2 \Phi}{\partial y^2} + \frac{\sigma_0}{\sigma_1} \frac{\partial^2 \Phi}{\partial z^2} + \frac{1}{\sigma_1} \frac{\partial \sigma_0}{\partial z} \frac{\partial \Phi}{\partial z} \right) = \vec{\nabla} \cdot \vec{j}_s \quad (3-6)$$

It is shown from (3-6) that the field is independent of σ_2 , the Hall conductivity, because of the antisymmetric property of the conductivity tensor. For simplification, we can express σ_0 and σ_1 as

$$\sigma_{0z} = \sigma_{00} \exp(2k_0 z) \quad (3-7)$$

and

$$\sigma_{1z} = \sigma_{10} \exp(2k_1 z) \quad (3-8)$$

where the second subscripts 0 and z refer to heights at and above the upper boundary of the atmosphere, or equivalently, the lower boundary of the ionosphere. $(2k_0)^{-1}$ and $(2k_1)^{-1}$ are scale heights of the specific and Pederson conductivities respectively. For better approximation, they can be divided into two different scale-height regions, one from 70-110 km and another 110-150 km.

(3-6) becomes

$$\sigma_1 \left(\frac{\partial^2}{\partial x^2} + \frac{\partial^2}{\partial y^2} + \frac{\sigma_0}{\sigma_1} \frac{\partial^2}{\partial z^2} + \frac{\sigma_0}{\sigma_1} \cdot 2k_0 \frac{\partial}{\partial z} \right) \Phi = \vec{\nabla} \cdot \vec{j}_s \quad (3-9)$$

Without repeating similar steps as in the previous chapter, we can write

$$\rho_{\text{source}} = - \frac{\epsilon_0}{\sigma_1} \vec{\nabla} \cdot \vec{j}_s$$

$$\rho_{\text{air}} = \epsilon_0 \cdot 2k_0 \frac{\partial \Phi}{\partial z} + \left(\frac{\sigma_0}{\sigma_1} - 1 \right) \frac{\partial^2 \Phi}{\partial z^2}$$

such that

$$\left(\frac{\partial^2}{\partial x^2} + \frac{\partial^2}{\partial y^2} + \frac{\sigma_0}{\sigma_1} \frac{\partial^2}{\partial z^2} + \frac{\sigma_0}{\sigma_1} 2k_0 \frac{\partial}{\partial z} \right) \phi = - \frac{\rho_{\text{source}}}{\epsilon_0} \equiv - \frac{f}{\epsilon_0} \quad (3-10)$$

and Green's function satisfies

$$\left(\frac{\partial^2}{\partial x^2} + \frac{\partial^2}{\partial y^2} + \frac{\sigma_0}{\sigma_1} \frac{\partial^2}{\partial z^2} + \frac{\sigma_0}{\sigma_1} 2k_0 \frac{\partial}{\partial z} \right) G = - \frac{1}{\epsilon_0} \delta(x-x') \delta(y-y') \delta(z-z') \quad (3-11)$$

The Fourier transformer g should be such that

$$G(r, z; r', z') = \iiint d\kappa_z \kappa_r d\kappa_r d\phi g(\kappa_r, \kappa_z) e^{i\kappa_z(z-z')} e^{i\vec{\kappa}_r \cdot (\vec{r}-\vec{r}')} \quad (3-12)$$

Substitute (3-12) into (3-11) and compare both sides:

$$\begin{aligned} & \iiint d\kappa_z \kappa_r d\kappa_r d\phi g(\kappa_r, \kappa_z) \left[-\kappa_r^2 - \frac{\sigma_0}{\sigma_1} \kappa_z^2 + i \frac{\sigma_0}{\sigma_1} 2k_0 \kappa_z \right] e^{i\kappa_z(z-z')} e^{i\vec{\kappa}_r \cdot (\vec{r}-\vec{r}')} \\ &= \iiint - \frac{1}{\epsilon_0 (2\pi)^3} d\kappa_z \kappa_r d\kappa_r d\phi e^{i\kappa_z(z-z')} e^{i\vec{\kappa}_r \cdot (\vec{r}-\vec{r}')} \\ &\therefore g(\kappa_r, \kappa_z) = \frac{1}{\epsilon_0 (2\pi)^3} \left[\kappa_r^2 + \frac{\sigma_0}{\sigma_1} \kappa_z^2 - 2i \frac{\sigma_0}{\sigma_1} k_0 \kappa_z \right]^{-1} \end{aligned} \quad (3-13)$$

Substitute (3-13) into (3-12) and use the relation (2-17):

$$G(r, z; r', z') = \frac{1}{\epsilon_0 (2\pi)^2} \int_{-\infty}^{\infty} \int_0^{\infty} d\kappa_z \kappa_r d\kappa_r \frac{e^{-\kappa_z(z-z')} J_0(\kappa_r |\vec{r}-\vec{r}'|)}{\frac{\sigma_0}{\sigma_1} \kappa_z^2 + \kappa_r^2 - 2i \frac{\sigma_0}{\sigma_1} k_0 \kappa_z}$$

The poles are at

$$\kappa_z = i \left(k_0 \pm \sqrt{k_0^2 + \frac{\sigma_1}{\sigma_0} \kappa^2} \right)$$

We choose the contour closing in the upper half plane. Contour integration then gives

$$G(r, z; r', z') = \frac{e^{-k_0(z-z')}}{4\pi\epsilon_0} \int_0^\infty \frac{\kappa_r d\kappa_r J_0(\kappa_r |r-r'|) e^{-\sqrt{k_0^2 + \frac{\sigma_1}{\sigma_0} \kappa_r^2} (z-z')}}{\frac{\sigma_0}{\sigma_1} \sqrt{k_0^2 + \frac{\sigma_1}{\sigma_0} \kappa_r^2}}$$

Define $\sqrt{\frac{\sigma_1}{\sigma_0}} \kappa_r \equiv \kappa'_r$

$$\begin{aligned} G(r, z; r', z') &= \frac{e^{-k_0(z-z')}}{4\pi\epsilon_0} \int_0^\infty \frac{\kappa'_r J_0(\kappa'_r \sqrt{\frac{\sigma_0}{\sigma_1}} |\vec{r}-\vec{r}'|) e^{-\sqrt{k_0^2 + \kappa_r'^2} (z-z')}}{\sqrt{\kappa_r'^2 + k_0^2}} d\kappa'_r \\ &= \frac{e^{-k_0(z-z')}}{4\pi\epsilon_0} \frac{e^{-k_0 \sqrt{\frac{\sigma_0}{\sigma_1}} |\vec{r}-\vec{r}'|^2 + (z-z')^2}}{\sqrt{\frac{\sigma_0}{\sigma_1} |\vec{r}-\vec{r}'|^2 + (z-z')^2}} \end{aligned}$$

The potential is thus

$$\Phi(r, z) = \int_{\tau'} G(r, z; r', z') f(r', z') d\tau' \quad (3-14)$$

where

$$G(r, z; r', z') = \frac{e^{-k_0(z-z')}}{4\pi\epsilon_0} \frac{e^{-k_0 \sqrt{\frac{\sigma_0}{\sigma_1}} |\vec{r}-\vec{r}'|^2 + (z-z')^2}}{\sqrt{\frac{\sigma_0}{\sigma_1} |\vec{r}-\vec{r}'|^2 + (z-z')^2}}$$

$$d\tau = r' dr' d\phi' dz',$$

and f is the source function.

Consider a simple case of a point charge source q in the lower ionosphere at $r = 0$ and $z = z_0$ above 70 km. The potential at altitude z above the source is simply

$$\Phi(r, z) = \frac{q}{4\pi\epsilon_0} e^{-k_0(z-z_0)} \frac{e^{-k_0 \sqrt{\frac{\sigma_0}{\sigma_1} r^2 + (z-z_0)^2}}}{\sqrt{\frac{\sigma_0}{\sigma_1} r^2 + (z-z_0)^2}} + \text{image term} \quad (3-15)$$

without any other boundary conditions.

Along the $r = 0$ axis, (3-15) reduces to

$$\Phi(r = 0, z) = \frac{q \cdot e^{-k_0(z-z_0)}}{4\pi\epsilon_0 (z-z_0)} \quad (3-16)$$

the same form as (2-30).

At all other distances ($r \neq 0$), however, the potential (and the field) decreases much faster than it would in the atmosphere because $\frac{\sigma_0}{\sigma_1} > 1$ in the ionosphere. σ_0 and σ_1 are the same at $h \leq 70$ km. Above that σ_0 increases faster than σ_1 ; at 150 km, they differ by 4-5 orders of magnitude (Figure 1-4). Above 150 km, the specific conductivity becomes so large that magnetic field lines can be considered as equipotentials. The mapping technique developed in this thesis will thus be confined to the region below 150 km.

II. Boundary Conditions

Now we can proceed to the mapping problem of atmospheric electric fields into the ionosphere. We will assume the simple point charge sources because

it was shown in Chapter 2 that all the weather-induced charge sources can be approximated as point sources at large distances.

The problem yet to be solved of field mapping between the atmosphere and the ionosphere is just a boundary value problem of different conductivities. This is similar to boundary value problems of different dielectrics because the dielectric and conductivity represent the real and imaginary parts of the complex dielectric coefficient respectively. In order to complete the mapping solution, we can take similar steps as in solving boundary value problems with different dielectrics which are shown in many electrodynamics books (cf. Smythe, 1950).

Assume a point charge q embedded at $P(z = z_0)$ in Region 1 (atmosphere). The boundary surface is at $h(z = 70 \text{ km})$ which separates the first medium from Region 2 (ionosphere) as shown in Figure 3-1. It is natural to locate an "image" q' in Region 2 at the symmetrical position P' . The potential at height z in Region 1 described by cylindrical coordinates is then

$$\Phi_1 = \frac{1}{4\pi\epsilon_0} \left[\frac{q e^{-k_{01}(Z+R_1)}}{R_1} + \frac{q' e^{-k_{01}(Z'+R'_1)}}{R'_1} \right] \quad (3-17)$$

In Region 2, since there is no charge source, it must be a solution of Laplace's equation without singularities in that region. Clearly the simplest assumption is that for $z > 70 \text{ km}$, the potential is equivalent to that of a charge q'' at P of the actual charge such that

$$\Phi_2 = \frac{q'' e^{-k_{02}(Z+R_2)}}{4\pi\epsilon_0 R_2} \quad (3-18)$$

where $(2k_{01})^{-1}$ and $(2k_{02})^{-1}$ are scale heights of specific conductivities in the atmosphere and ionosphere respectively and

$$Z = z - z_0$$

$$Z' = 2h - z_0 - z$$

$$R_1 = \sqrt{\frac{\sigma_{01}}{\sigma_{11}} r^2 + Z^2}$$

$$R_2 = \sqrt{\frac{\sigma_{02}}{\sigma_{12}} r^2 + Z^2}, \text{ and}$$

$$R'_1 = \sqrt{\frac{\sigma_{01}}{\sigma_{11}} r^2 + Z'^2}$$

The boundary conditions required at $z = 70$ km in this case are:

(1) tangential condition

$$\phi_1 \Big|_{\lim h \rightarrow 70^-} = \phi_2 \Big|_{\lim h \rightarrow 70^+} \quad (3-19)$$

(2) normal condition

$$\sigma_{01} \frac{\partial \phi_1}{\partial z} \Big|_{\lim h \rightarrow 70^-} = \sigma_{02} \frac{\partial \phi_2}{\partial z} \Big|_{\lim h \rightarrow 70^+} \quad (3-20)$$

where subscripts 1 and 2 refer to the atmosphere and ionosphere up to 150 km respectively. Since the conductivity is continuous at the boundary, (3-20) is equivalent to

$$\frac{\partial \phi_1}{\partial z} \Big|_{\lim h \rightarrow 70^-} = \frac{\partial \phi_2}{\partial z} \Big|_{\lim h \rightarrow 70^+} \quad (3-21)$$

Also at h ($z = 70$ km), $\frac{\sigma_0}{\sigma_1} = 1$ and $Z = Z' = 70 - z_0$, $R = R' = \sqrt{r^2 + Z^2}$.

Boundary condition (3-19) implies that

$$(q+q') e^{-k_{01}(Z+R)} = q'' e^{-k_{02}(Z+R)} \quad (3-22)$$

Boundary condition (3-21) is reduced to

$$q - q' = q'' \left[e^{-(k_{02} - k_{01})(Z+R)} \right] \left[\frac{Z/R + k_{02}(Z+R)}{Z/R + k_{01}(Z+R)} \right] \quad (3-23)$$

Solving (3-22) and (3-23):

$$q' = q \left[\frac{(k_{01} - k_{02})(Z+R)}{(k_{01} + k_{02})(Z+R) + 2Z/R} \right] \quad (3-24)$$

and

$$q'' = 2q \left[\frac{Z/R + k_{01}(Z+R)}{(k_{01} + k_{02})(Z+R) + 2Z/R} \right] e^{[(k_{01} - k_{02})(Z+R)]} \quad (3-25)$$

Substituting them back into (3-17) and (3-18), we obtain potential expressions both in the atmosphere and the lower ionosphere and therefore can calculate the vector electric fields.

We can write similar expressions if the lower ionosphere is divided into two different scale height regions. Figure 3-2 shows the conductivity profiles below 150 km for both day and night. The scale heights are $(2k_{02})^{-1} = 3$ km, $(2k_{03})^{-1} = \infty$, $(2k_{12})^{-1} = 6$ km and $(2k_{13})^{-1} = -24$ km, where the first subscripts 0 and 1 refer to specific and Pederson conductivities, the second subscripts 2 and 3 refer to regions 70-110 km respectively for nighttime and 70-120 km and 120-150 km for daytime. Since the electric fields are only affected by the relative scale heights of conductivities but not their absolute values, the field mapping equations are the same for both day and night.

III. Results

Electric fields mapped into the ionosphere can now be calculated and plotted for higher latitude regions from the results (3-17), (3-18) (3-24) and (3-25). Figure 3-3 shows variations in the vertical fields at different horizontal distances. The vertical field decreases rapidly with altitude. In other words, vertical fields induced by weather in the atmosphere dissipates fast in the ionosphere. This is due to the fact that specific conductivity increases rapidly with altitude. At even higher altitudes (from the F2 region around 200 km and higher) the conductivity is so high that the magnetic field lines become equipotentials which force the electric fields along them to go to zero.

Figure 3-4 shows variations of the horizontal fields. Within the 50 km horizontal range considered, they vary in the same bulk order of magnitude as the vertical fields. However, at higher altitudes, 200 km or above, when $\sigma_0/\sigma_1 \gg 1$ (for example, at 200 km, $\sigma_0/\sigma_1 \sim 10^5-10^6$ and at 500 km, $\sigma_0/\sigma_1 \sim 10^8$) and such that $\sqrt{\sigma_0/\sigma_1} \cdot r \gg z$, the vertical field vanishes and the horizontal field E_r approaches an asymptotic value. In other words, E_r becomes a function of r , independent of z .

To demonstrate the case mathematically, we start from (3-18)

$$\phi'' = \frac{q''}{4\pi\epsilon_0} \frac{e^{-k_0(Z+R)}}{R} \quad (3-18)$$

where $z = z - z_0$

$$R = \sqrt{\frac{\sigma_0}{\sigma_1} r^2 + z^2}$$

$$\text{or } \lim_{\sqrt{\frac{\sigma_0}{\sigma_1}} r \gg z} R_2 = \sqrt{\frac{\sigma_0}{\sigma_1}} r$$

such that

$$\lim_{\sqrt{\frac{\sigma_0}{\sigma_1}} r \gg z} \phi = \frac{q''}{4\pi\epsilon_0} \sqrt{\frac{\sigma_1}{\sigma_0}} \frac{e^{-k\left(\sqrt{\frac{\sigma_0}{\sigma_1}} r\right)}}{r} \quad (3-26)$$

This leads to

$$\lim E_z = 0 \quad (3-27)$$

and

$$\lim E_r = \frac{q''}{4\pi\epsilon_0} \sqrt{\frac{\sigma_1}{\sigma_0}} \frac{e^{-k_0\sqrt{\frac{\sigma_0}{\sigma_1}} r}}{r^2} \left(1 + k_0\sqrt{\frac{\sigma_0}{\sigma_1}}\right) \quad (3-28)$$

Figure 3-5 is a diagram of different conductivity profiles in the ionosphere up to 1000 km. It is shown that above the F2 region (~250 km) σ_0 remains constant which implies that $k_0 \rightarrow \infty$. Thus (3-26) and (3-28) are simply

$$\lim \phi = \frac{q''}{4\pi\epsilon_0} \sqrt{\frac{\sigma_1}{\sigma_0}} \frac{1}{r} \quad (3-29)$$

and

$$\lim E_r = \frac{q''}{4\pi\epsilon_0} \sqrt{\frac{\sigma_1}{\sigma_0}} \frac{1}{r^2} \quad (3-30)$$

It is also of interest to observe the corresponding horizontal distance for maximum E_r at different altitudes. It is a simple relationship for Coulomb field conditions. Since

$$\phi \propto \frac{1}{(r^2+z^2)^{1/2}}$$

and

$$E_r \propto \frac{1}{(r^2+z^2)^{3/2}}$$

such that

$$\frac{dE_r}{dr} = 0 \quad \text{implies}$$

$$2r^2 - z^2 = 0$$

or

$$r \Big|_{E_{r \max}} = \frac{1}{\sqrt{2}} z = 0.7z.$$

However, in the atmosphere-ionosphere system, the situation is quite different. In the isotropic atmosphere, the ratio $r \Big|_{E_{r \max}} / z$ starts from ~ 0.2 at lower altitude and increases to ~ 0.5 at 20 km, then drops slowly till the top of the atmosphere. In the anisotropic ionosphere the ratio drops at a much faster rate with increasing altitude. At 120 km, $E_{r \max}$ is at $r \sim 0.5$ km which gives the ratio $r \Big|_{E_{r \max}} / z \sim 0.004$. Table 3-1 gives in more detail the horizontal fields at different altitudes. We have again considered the same charge source as in the previous sections: +20 C at 6 km and -20 C at 4 km.

At lower latitude regions where magnetic field lines are no longer along z axis, the differential equation to be solved is much more complex. The conductivity tensor is of a more general form

$$\underline{\sigma} = \begin{pmatrix} \sigma_1 \sin I + \cos I & \sigma_2 \sin I & (\sigma_0 - \sigma_1) \sin I \cos I \\ -\sigma_2 \sin I & \sigma_1 & \sigma_2 \cos I \\ (\sigma_0 - \sigma_1) \sin I \cos I & -\sigma_2 \cos I & \sigma_1 \cos^2 I + \sigma_0 \sin^2 I \end{pmatrix}$$

where I is the magnetic dip angle; at pole $I = 90^\circ$ and at equator $I = 0$ for a dipole model.

At equator, it is reduced to

$$\approx = \begin{pmatrix} \sigma_0 & 0 & 0 \\ 0 & \sigma_1 & \sigma_2 \\ 0 & -\sigma_2 & \sigma_1 \end{pmatrix}$$

such that the potential equation to be solved is

$$\frac{\sigma_0}{\sigma_1} \frac{\partial^2 \Phi}{\partial x^2} + \frac{\partial^2 \Phi}{\partial y^2} + \frac{\partial^2 \Phi}{\partial z^2} - 2k_2 \frac{\sigma_2}{\sigma_1} \frac{\partial \Phi}{\partial y} + 2k_1 \frac{\partial \Phi}{\partial z} = - \frac{f}{\epsilon_0} \quad (3-31)$$

Difficulty arises because equation (3-31) does not have the property of spherical symmetry. Different approximation methods and computer techniques will have to be used in order to obtain the electric field profile. Furthermore, in the upper atmosphere of lower latitude regions, tidal winds interact with the geomagnetic field and charged particles which induces electric fields and current flow. According to this dynamo theory (first developed by Chapman and Bartels, 1940), the induced electric fields bear both solar and lunar variations which will add more difficulty on filtering out the thunderstorm electric fields in the lower latitude ionosphere. Generally speaking, however, we can anticipate that at equatorial region, the component of the electric field parallel to the magnetic field lines will dissipate faster than other components, and E_z will reach an asymptotic value at higher altitudes. Furthermore, since ionospheric conductivities are much higher at equatorial regions, especially during the day, than at higher latitude regions, the electric fields will map less efficiently in equatorial than higher latitude regions. In short, electric fields induced by thunderstorms in the equatorial region are less efficient in being mapped into the lower ionosphere than those produced at higher latitude regions.

Altitude (km)	E_r (V/m) at different horizontal distances								horiz. dist. where E_r is $E_{r \max}$	$\frac{r_{E \max}}{z}$
	0.2 km	0.5 km	1.0 km	2.0 km	5.0 km	10 km	20 km	50 km		
Isotropic	10	2.8×10^2	6.9×10^2	1.3×10^3	1.9×10^3	2.9×10^2	3.1×10^1	2.4×10^{-1}	~ 2 km	0.2
	20	1.0×10^0	2.6×10^0	5.1×10^0	1.0×10^1	2.0×10^1	6.9×10^0	1.2×10^{-1}	~ 10 km	0.5
	50	1.4×10^{-4}	3.6×10^{-4}	7.2×10^{-4}	1.4×10^{-3}	6.0×10^{-3}	7.2×10^{-3}	1.2×10^{-3}	~ 20 km	0.4
	70	8.6×10^{-7}	2.1×10^{-6}	4.3×10^{-6}	8.5×10^{-6}	3.8×10^{-5}	5.5×10^{-5}	2.0×10^{-5}	~ 20 km	0.3
Anisotropic	100	3.8×10^{-9}	9.3×10^{-9}	1.6×10^{-8}	2.1×10^{-9}	2.6×10^{-9}	1.6×10^{-12}	4.2×10^{-47}	~ 2 km	0.02
	120	8.0×10^{-11}	9.3×10^{-11}	1.5×10^{-11}	9.8×10^{-15}	5.7×10^{-14}	7.1×10^{-14}	—	~ 0.5 km	0.04

Table 3-1

Horizontal electric fields at different altitudes and horizontal distances.

The sources are 20 Coul at 6 km and -20 Coul at 4 km.

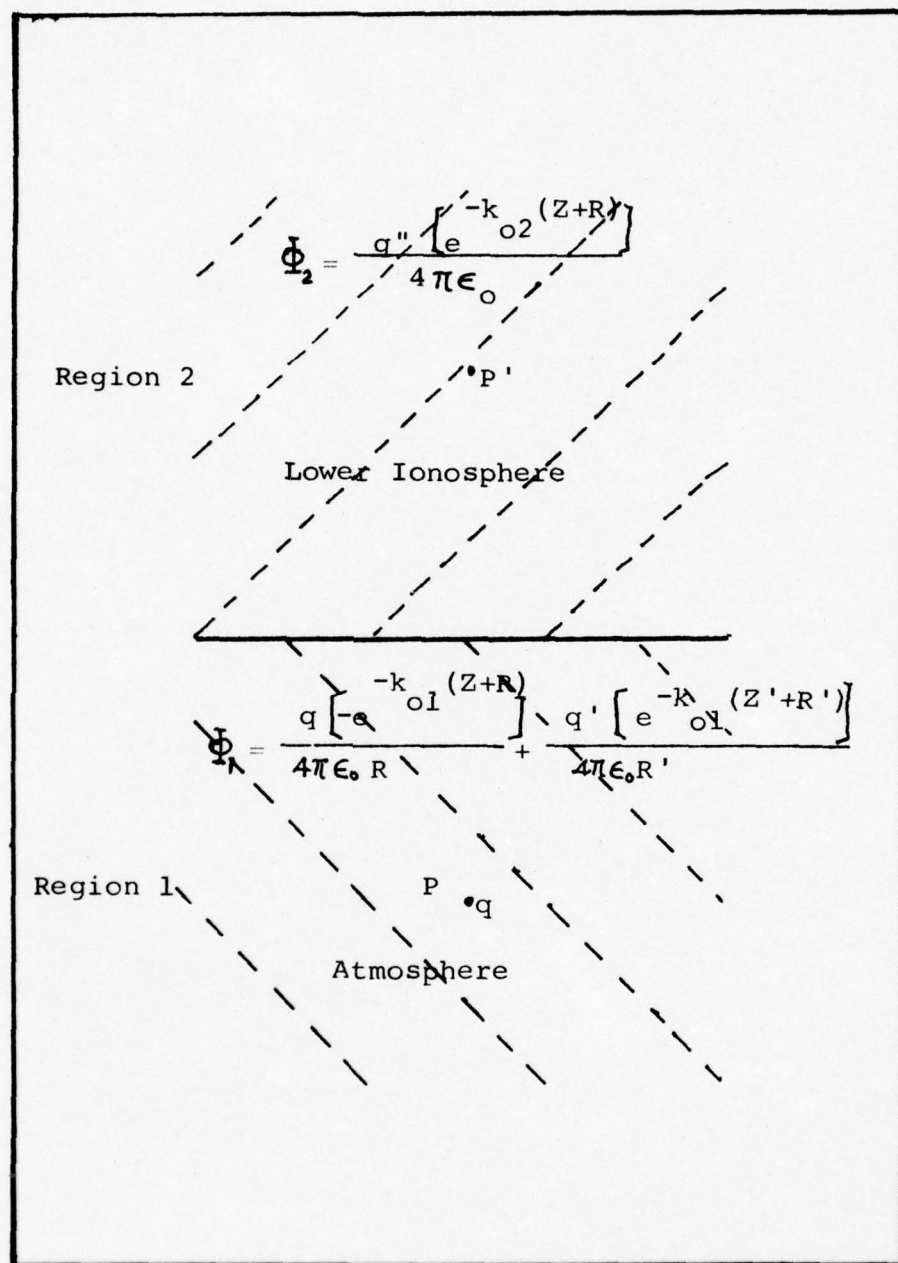


Figure 3-1

Illustration for Boudary value problem between Atmosphere and Ionosphere

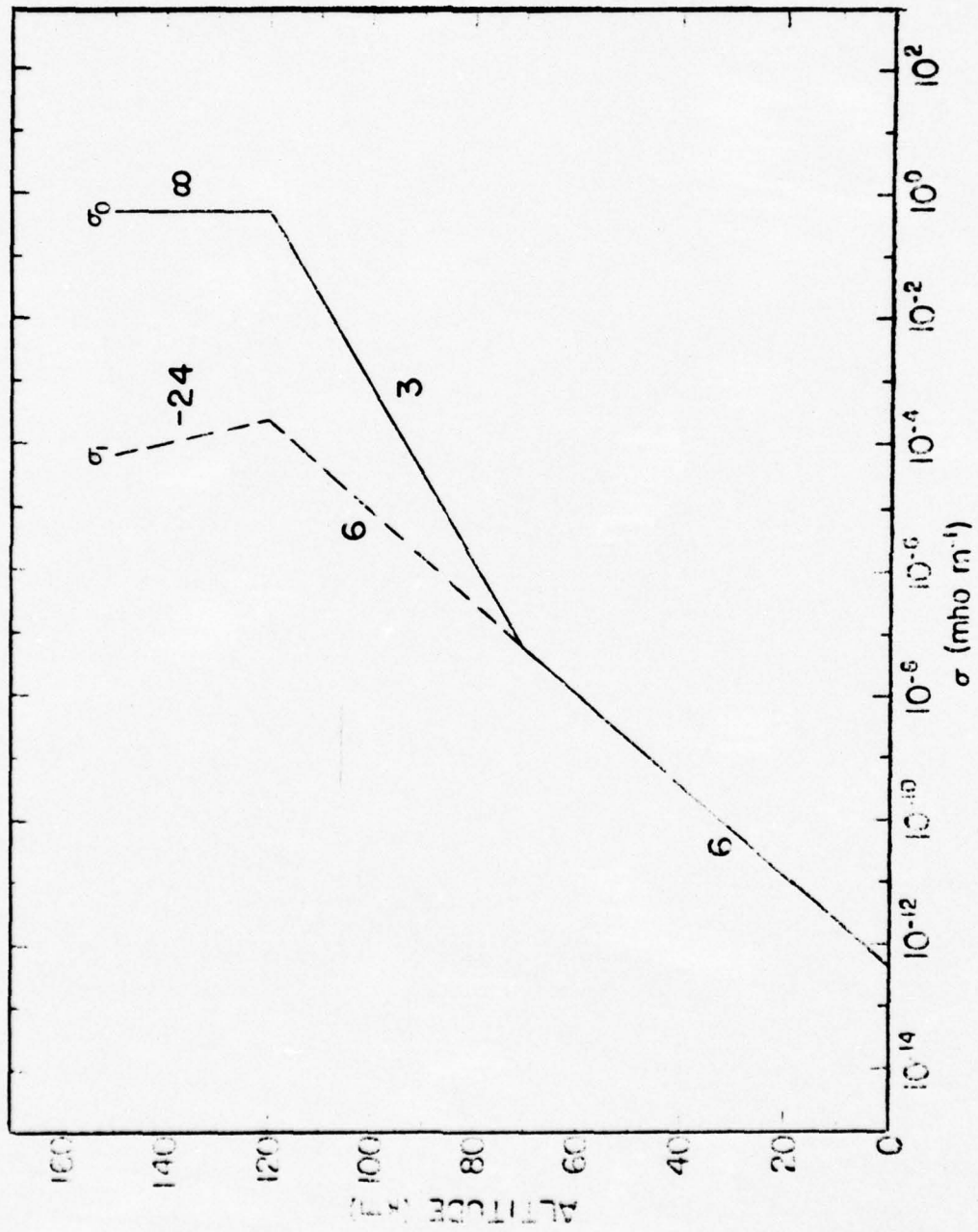


Figure 3-2a

Conductivity profile approximating the daytime condition above 70 km and the Cole and Pierce profile below 70 km. The numbers next to the curves are scale heights in kilometers. (Park and Dejnakintra, 1974)

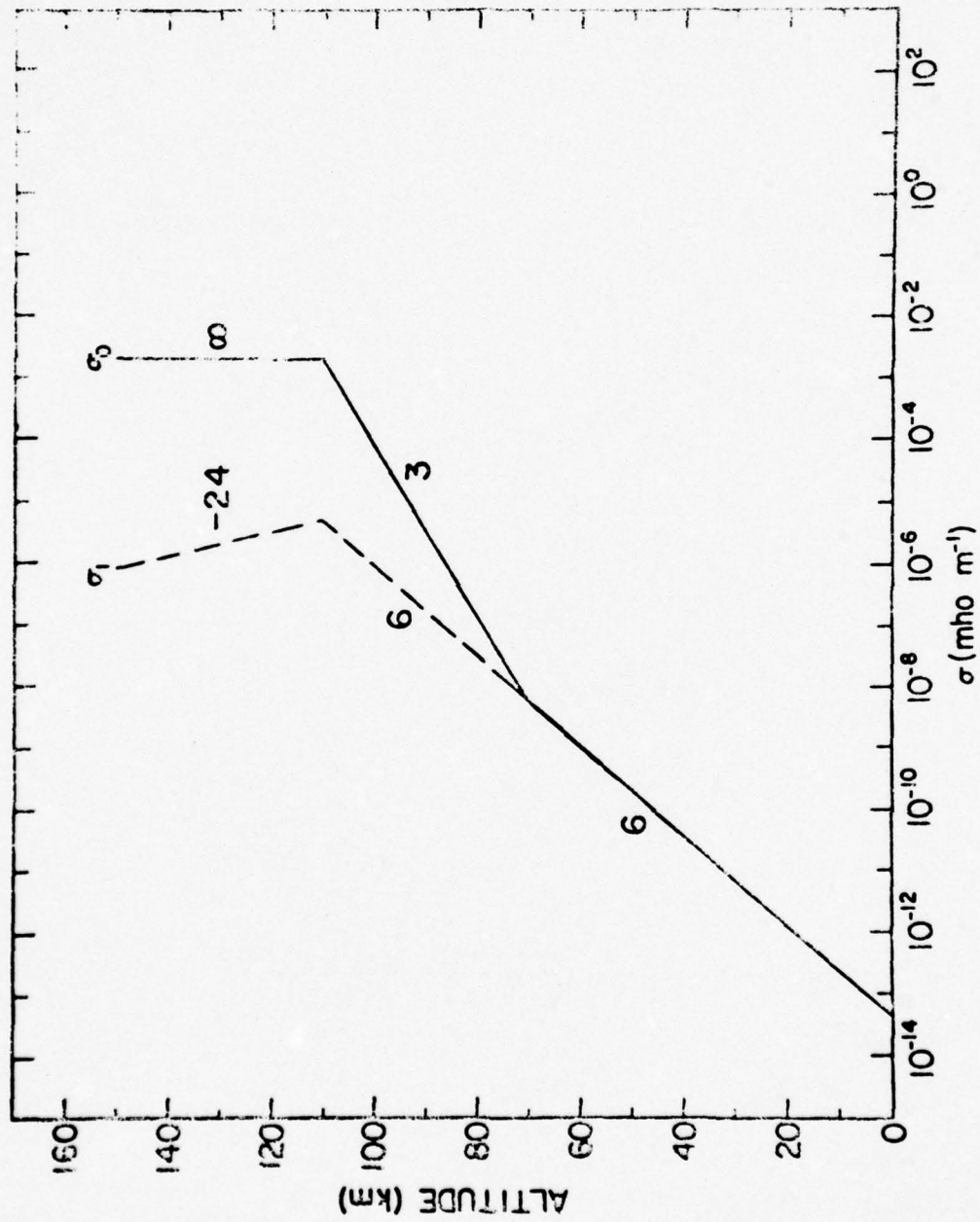


Figure 3-2b

Conductivity profile approximating the nighttime condition

(Park and Dejnakintra, 1974)

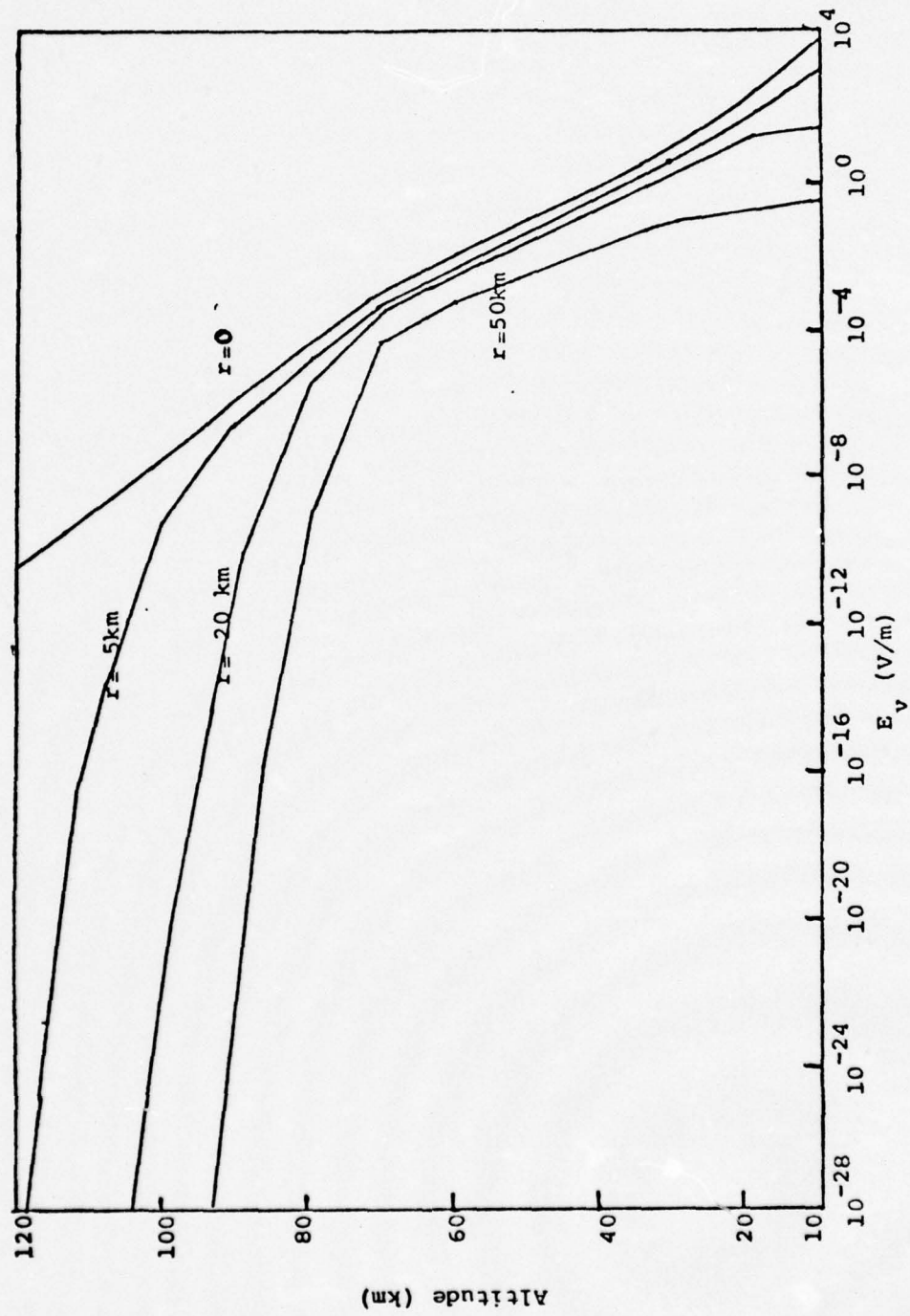


Figure 3-3
Vertical fields mapped into the ionosphere

Figure 3-3

Vertical electric fields mapped into the ionosphere.

The source is an electric dipole of 20 C at 6 km and -20 C
at 4 km.

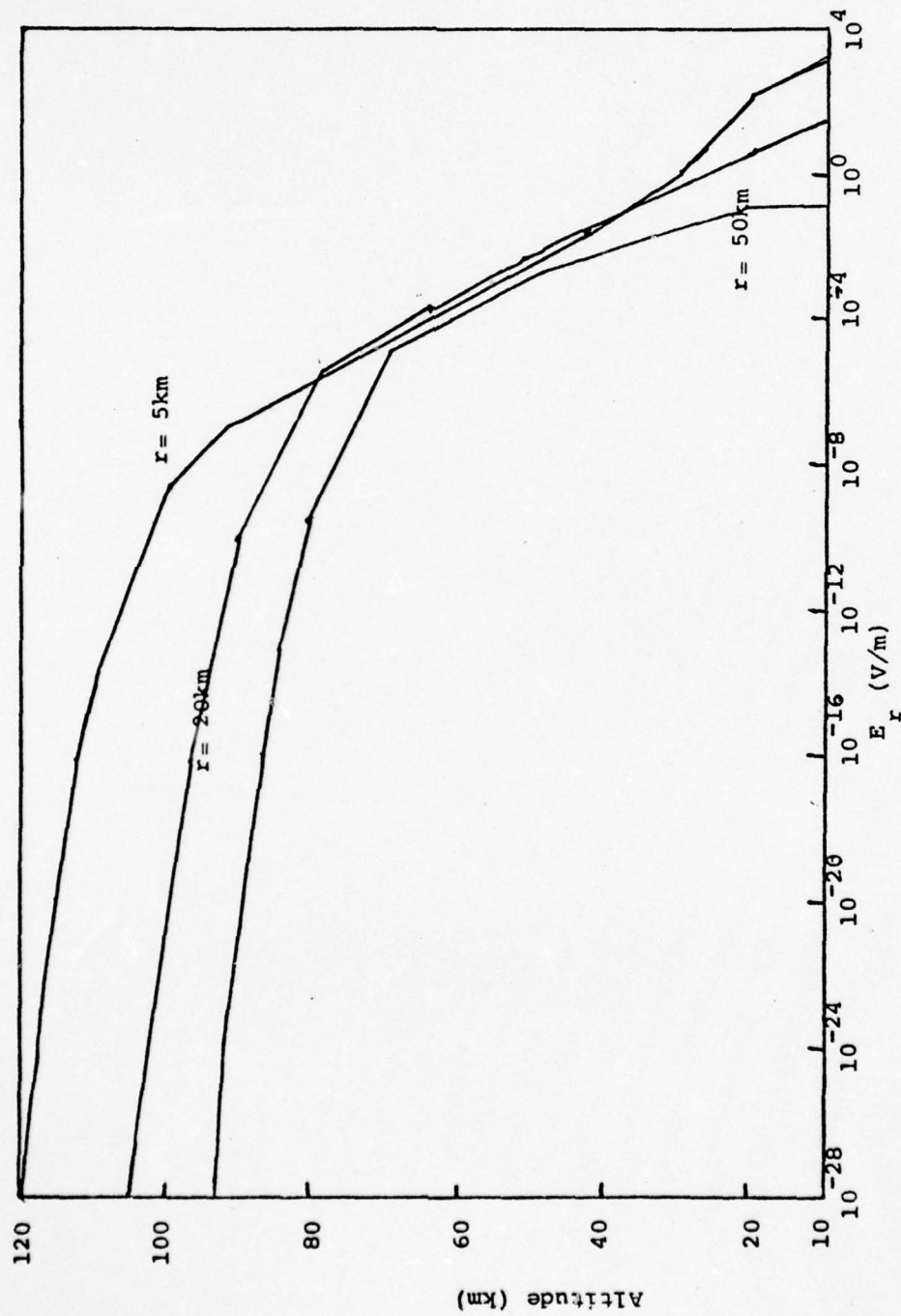


Figure 3-4
Horizontal fields mapped into the lower ionosphere

Figure 3-4

Horizontal electric fields mapped into the lower ionosphere.
The source is an electric dipole of 20 C at 6 km and -20 C
at 4 km.

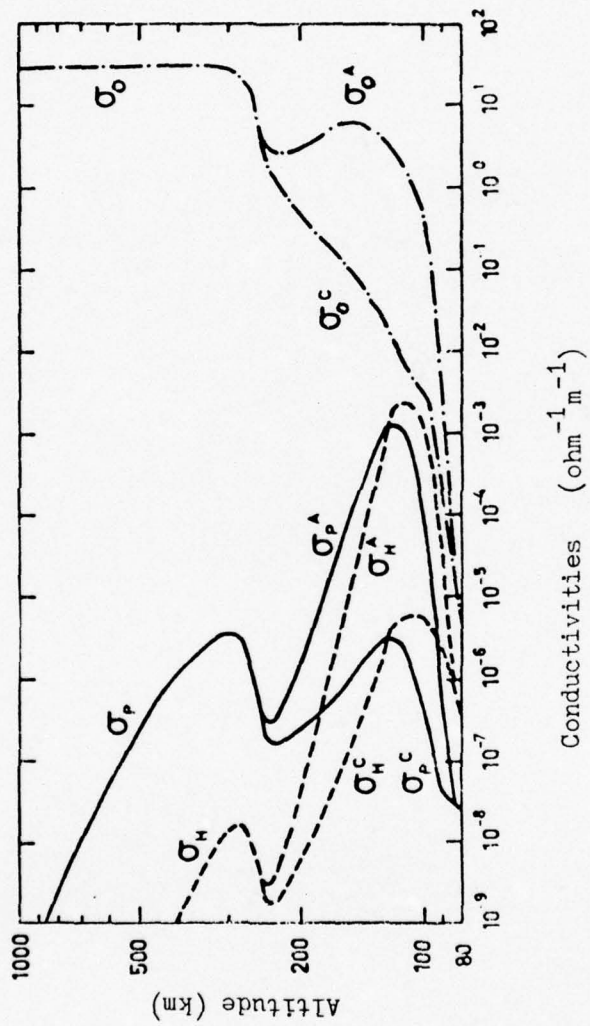


Figure 3-5

Large scale conductivity profiles in the ionosphere.

δ_p , δ_H , δ_o are pederson, Hall and specific conductivities respectively.

A refers to the region within aurora arc. C refers to the region of the undisturbed ionosphere surrounding the arc.

(Böstrom, 1964)

CHAPTER 4

COMPARISON BETWEEN THE MODEL AND DATA FROM A BALLOON FLIGHT

I. General Description of the Balloon Flight and Data

In August 1969, a total of 24 balloons were flown in four different launches from six Canadian sites (Figure 4-1) with each of the balloons in a group simultaneously returning data for up to one day. Approximately 370 hours of data are available and the vector electric fields can be calculated. The sensitivities of the vector components were such that during fair weather conditions, the vector electric field was recorded at less than half of the full scale in that channel, while the slowly time-varying horizontal fields (often associated with magnetospheric activity) were displayed in the two other channels. Thus fair weather conditions can be studied in detail. During several flights where balloons passed over thunderstorms, atmospheric fields were strong enough at times to saturate the continuous channels for the three components. However, large dynamic range electric fields signals were also transmitted in commutated forms.

The balloon payloads have been described in various papers (Mozier and Serlin, 1969; Mozier and Manka, 1971; and Mozier, 1971). A typical structure is as follows:

The balloon was separated from the payload by a rope of about 50 meters long such that its presence would not distort the fields at the

payload. Volumes of different balloons ranged from about 1600 cubic meters to around 7100 cubic meters such that ceiling altitudes of 26 km to 34 km were reached.

The electric field sensors were three mutually orthogonal pairs of dipole probes, two horizontal and one vertical. Each dipole probe pair consisted of an insulated ($\sim 10^{14}$ ohms) rod about 3 meters long with a conducting plate at each end. Each electric field component was determined as the potential difference between the appropriate pair of plates divided by their separation distance. The payload was driven by an electric motor such that it rotated with a period of 20 to 25 seconds. An on-board magnetometer provided orientation information which allowed resolution of the horizontal field into components in the magnetic north and east directions.

In order to measure the ambient electric field with accuracy, it was necessary to utilize very high input impedance preamplifier connected to the sensors. The signal of interest, V , causes a current of V/R_{circuit} to flow through the electronic input resistance, R_{circuit} . This current returns through the atmosphere along a path with resistance R_{atm} . Unless $R_{\text{circuit}} \gg R_{\text{atm}}$, an attenuated signal would be measured because an appreciable amount of V would then appear across R_{atm} . The value of R_{atm} depends on the conductivity of air at different altitudes. For the balloon system considered, $R_{\text{atm}} \approx 10^{13}$ ohms near the surface of the earth and $R_{\text{atm}} \approx 10^{11}$ ohms at 30 km. Thus an input resistance greater than 10^{14} ohms was required for field measurements. Electric circuits meeting this requirement were flown on the balloons. The four

subcarrier inputs to the FM - FM telemetry transmitter consisted of the three components of electric fields and a commutator through which other ranges of sensitivity on the electric field measurements, magnetometer and horizontal orientation information, housekeeping temperature, voltages and currents were transmitted.

In this thesis, the effort has been concentrated on the August 3, 1969, balloon flight launched from Penhold, Canada, at 0328 UT (2028 LT). Data were collected for about 21 hours. They included information on thunderstorm activity in the vicinity during the first portion of the flight and also the recovered fair weather field in the later portion. The following pieces of data (and reduced data) have been obtained:

- (a) continuous raw data of the whole flight showing saturation of field during the thunderstorm, spikes due to lightning flashes and the continuous fair weather field data after recovery of the storm;
- (b) plots of vector fields with 60 minute averages on compressed scale (0.4 in/hr) of the whole flight;
- (c) plots of vector fields with 15 minute averages on the same scale as (b) of the whole flight;
- (d) computer printout and plots of vector fields with 30 second averages on expanded scale (12 in/hr) from 0500 UT to 1000 UT for d-c thunderstorm electric field study; and
- (e) computer printout and plots of electric fields with 0.5 second averages on more expanded scale (4 in/hr) from 0800 UT to 0850 UT, when lightning activity was present, for detailed study of lightning induced fields.

The thunderstorm passed Penhold area at around 0300 UT with a velocity of 15 miles/hr to the east. The balloon, launched at 0328 UT, was first drifting to the east until around 0630 UT. It then moved to the west at 15 to 20 miles/hr and was overhead at Penhold again around 0700 UT. The ceiling height was around 28.7 km (94,000 ft).

Figure 4-2 shows the raw data format of balloon field data. Figures 4-3a and b are portions of raw data indicating the presence of thunderstorm in the vicinity and distinct lightning events respectively.

II. Fair Weather Field Data

Figure 4-4 shows the fair weather vector electric fields during the later portion of the flight. They can be discussed separately as the vertical and horizontal components of the electric field.

(1) Vertical field:

The average reading for the vertical field was at 300 mV/m. This agrees with the prediction of (2-13) for z at 28 km, the balloon altitude at the time, with scale height of conductivity $(2k)^{-1} = 5$ km. We have to keep in mind this downward field as the background value when analyzing field data during the thunderstorm period.

(2) Horizontal field:

The fair weather horizontal fields observed by balloon measurements in higher latitude regions are mostly of magnetospheric origins (Mozer and Manka, 1971). Enhancement in horizontal electric field with increasing K_p (a number ranging from 0 to 9 indicating the degree of disturbance of the geomagnetic field) has largely been observed. During quiet conditions, the observations can be best explained by the sunward

$\vec{E} \times \vec{B}$ convection model. An overall average of 32 balloon flights in the aurora zone indicated that the dominating field component is southward near dawn (0600 LT) and northward near dusk (1800 LT) (Mozer and Lucht, 1974). They also showed that for the south-north field component the maximum field, which occurs at dawn or dusk, is less than 25 mV/m and it gets close to zero at 0000 LT and 1200 LT during periods of low Kp. During times of high Kp, it fluctuates between ± 40 mV/m. For west-east field component, it does not get beyond a few mV/m during quiet times and can go up to 25 mV/m during disturbed times.

At around 0900 UT August, 1969, the Kp index was at 2- (Solar-Geophysical Data, 1969) which indicated a relatively quiet condition. As a result, the west-east field component should be zero; and the south-north component, since it was near 0200 LT, should also vanish. This agrees with observations in Figure 4-4. Furthermore, we should also bear in mind that during the thunderstorm period around 0600 UT (2300 LT), there should not be much significant field of magnetospheric origins so that the electric field observed during that period would be all weather-induced.

III. Expected Thunderstorm Field and Comparison with Data

Vector fields at balloon altitude due to thunderclouds in the lower atmosphere can be predicted from calculations of (2-26) and (2-27). During the Penhold balloon flight of August 3, 1969, observations of thunderstorm measurements were between 0500 UT and 0630 UT. At this time, the balloon was moving to the east relative to the storm at about 20 miles per hour. According to nearby radiosonde data from Edmington, 70 miles northwest of

Penhold, the freezing level was at around $2\frac{1}{2}$ km altitude at the time (Monthly Bulletin, Canadian Upper Air Data, 1969). It is generally accepted that the negative charge region inside a thundercloud is concentrated near the -5°C isotherm. The ceiling height of the clouds was around 7 km. It is then reasonable to assume a dipole cloud model with the centers of negative and positive charge regions at 4 km and 6 km respectively. Since the balloon was at sufficiently high altitude comparing to the cloud, point charge assumption is a good enough approximation for different kinds of models; for example, cylindrical, disc models either upright or tilted.

Also according to the same radiosonde information, at balloon altitude, the temperature was at -40°C , pressure at 20 mb and the wind was easterly at 6 miles/hr. And at the altitude near the storm, the temperature was -15°C along the 500 mb isobar and the wind was southwest-westerly at around 14 miles/hr.

By comparison between the maximum changes in vertical and horizontal fields, the charge concentrations were estimated at ± 20 Coul. A Cartesian coordinate system can be defined such that x-axis is to the east, y-axis to the north and z-axis in the upward direction. Since the balloon was moving to the east relative to the storm, the horizontal field components along and perpendicular to the balloon trajectory can be referred to as the x and y components of the total field respectively. The vertical field is the z component.

Figure 4-5 shows the expected vertical field at balloon altitude (~ 28 km) along different horizontal trajectories of $y = 0, 10$ and 20 km. The field above the axis refers to upward direction. The maximum vertical field changes for this case are 5.00 V/m when overhead, 3.44 V/m

along the $y = 10$ km trajectory and 1.37 V/m if $y = 20$ km. From the figure it shows the field decreases fast with increasing distance in x . At $x = 40$ km, it approaches zero. Actually for a dipole source, the vertical field would change its sign at some horizontal distance. Closer than this distance the vertical field is upward and beyond this distance the field is downward (the same direction as the fair weather field). However, at balloon altitude, the field does not change its sign until $x \gtrsim 100$ km. Since the magnitude of the field change is already very small, this effect is not at all noticeable and would not be detected by the balloon field sensors.

Figure 4-6 is the expected electric field changes in the horizontal plane along the trajectory (E_x). For the case that the balloon moves to the east relative to the storm, the direction of this component of electric field is such that when the balloon is approaching the thundercloud (negative x) the field is to the west, and when the balloon is receding from the storm, the field is to the east. The maximum horizontal field changes along the trajectory due to the thundercloud considered are 0.86 V/m at $x = 10$ km along the $y = 0$ trajectory, 0.60 V/m at $x = 12$ km if $y = 10$ km and 0.25 V/m at $x = 15$ km if $y = 20$ km.

Figure 4-7 is the expected electric field changes in the horizontal plane perpendicular to the trajectory (E_y). The direction of this field component is such that if the trajectory is north to the thundercloud, a northward field will be experienced all the way. For the case when the balloon is flying along $y = 0$, no E_y will be experienced. Otherwise the maximum occurs at $x = 0$. The values are 0.85 V/m when $y = 10$ km and 0.62 V/m if $y = 20$ km.

Figure 4-8 shows the averaged field data in the vertical, east-west and north-south directions between 0500 UT and 0630 UT. In order to trace the number of cells encountered, to estimate the magnitude of charge involved and to locate the relative position of the storm with respect to the balloon trajectory, the following steps are taken:

- (1) By studying the peaks in the vertical field, we can determine the number of cells with charge concentrations and their distances from each other. In Figure 4-8, it is indicated that there were two major cells encountered by the balloon at around 0535 UT and 0605 UT respectively; another one right before 0500 UT and one after 0630 UT. Since according to radar tracking at the time, the relative velocity of the balloon was about 20 miles/hr relative to the storm, it implies that the cells were approximately 10-15 miles (16-20 km) from each other. This agrees with weather observations which indicated the average separation between cells ranged from 10-20 miles. Furthermore, the difference between the peak vertical field value and the lowest value should be the maximum change of the vertical field. We thus obtain the maximum vertical field due to thundercloud structure to be around 1.2 V/m in the upward direction.
- (2) Since the balloon trajectory relative to the storm was along the east-west direction, the north-south field, the horizontal field perpendicular to the trajectory, should vary in the same phase as the vertical field. As

shown in Figure 4-8, the peak readings in the southward direction occurred at generally the same time as the vertical field which indicated that the balloon trajectory was south to the thunderclouds. The only exception is the peak of the southward field at 0510 UT which indicated that either the cell that the balloon just flew by had a tilted dipole structure or the balloon trajectory with respect to the cell was diverted from the assumed south direction. The difference between the maximum magnitude and the lowest value was around 0.45 V/m. We can then estimate, together with the vertical field, how far away the balloon trajectory was from the storm and the charge concentration in each cell. Comparing results from Figure 4-5 and Figure 4-7, we can conclude that the charge concentration was around ± 20 Coul in each major cell and the trajectory was 20-22 km south to the thunderclouds.

- (3) One major problem left is the almost constant bias in the measured vertical and north-south fields. After subtracting the 0.3 V/m normal downward field, the electric field still has an additional 0.3 V/m in the downward direction and around 0.15 V/m in the northward direction. They are about $1/4$ to $1/3$ of the maximum of the field component in the opposite directions. It seems most probable that there must be a negative charge source spread over the thunderclouds. The possible explanation

for this phenomenon is as follows:

There exists a "shielding layer" in the boundary region of the cloud. The formation of this layer is due to the differences in conductivities between the air and the cloud at cloud boundary. Measurements have indicated that the cloud is a much less conducting medium than air. Because of the dipole structure of the thundercloud, there will be a layer of negative charge accumulated on top of the cloud to match the discontinuous boundary condition. There should also be a layer of positive charge near the bottom. Phillips (1967) has made theoretical calculations using the method of ionic equilibrium at the cloud boundary. He showed that the loss by conduction to cloud droplets due to the shielding layer charge distribution was about 1/3 that would occur in the absence of such a layer. The thickness of the shielding layer was calculated to be in the order of tens of meters. The total shielding charge in this case is estimated to be ± 5 Coul at the top and bottom boundaries of each cell.

The field detected by the field sensors thus include (1) normal background fair weather field (downward), (2) the field due to thunderclouds (upward) and (3) the shielding field (downward). Figure 4-9 shows how these fields combine to give the total vertical fields and how they compare with the observed values. The horizontal fields can be done similarly.

- (4) From (1) and (2) we estimated the charge concentrations

to be ± 20 Coul in each thundercloud and the balloon trajectory was around 22 km south of the storm. We can then get the resultant east-west horizontal field, the field component along the direction of the trajectory, by superposition of the east-west field due to different cells (Figure 4-10). The calculated results agrees with the shape of the experienced field except most of the time there existed an unexplained additional eastward field of 0.005 to 0.008 V/m in magnitude. This was not due to the large scale shielding effect just discussed because the component along the trajectory should cancel out. It could not be of ionospheric origin either because the ionospheric condition was relatively quiet at the time and 0.08 V/m is too large a field compared to the normal 0.02 V/m ionospheric fluctuations. It is still most probably of atmospheric origin, namely a general disturbed area to the west as a continuation of the storm. This source, if existed, had to be far off enough such that peaks in fields due to different cells would not be experienced at the balloon.

In general, the data agree with the predictions and the assumed models. We are able to locate the storm position relative to the balloon and estimate the charge distribution. The major difficulties in data analyzing include:

- (1) Lack of continuous storm information from radar. For example, information on the time history of the storms and locations of different

thunderclouds at all times were not available.

(2) Saturation of data information. In Figure 4-8, part of the vertical and north-south field readings were missing because of instrument saturation. Some of the peak values could only be approximated from the slopes of the general envelop. As a result, only estimates could be made instead of exact calculations.

Nonetheless, this balloon flight has been one of the very few vector electric field measurements above thunderstorms that indicated definite field variations and provided valuable information on thundercloud mapping into the upper atmosphere. The improvements and potential of field measurements by balloons will be discussed in the next chapter.

IV. A Study of the Lightning Events

In the preceding section we have examined the thunderstorm induced electric fields due to static or slow varying distributions of charges inside thunderclouds. During a later portion of the flight (around 0830 UT) the balloon experienced some lightning activity. In this section we will study these lightning induced fields in some detail.

In a lightning discharge, there is a considerable variation in charge and current in a relatively short time interval. Thus in addition to the electrostatic field, we also have to look into the time-varying electromagnetic fields associated with lightning discharge.

For a system of source of charges and fields varying with time, we can assume the time variation factor to be $e^{-i\omega t}$ such that

$$\rho(\vec{x}, t) = \rho(\vec{x})e^{-i\omega t}$$

and
$$\vec{j}(\vec{x}, t) = \vec{j}(\vec{x})e^{-i\omega t}$$

where the real part of the expression is to be taken to obtain physical quantities. The electromagnetic potentials and fields are also assumed to have the same time dependence. In the limit that source region is of a much smaller scale compared to one wavelength $\lambda = 2\pi c/\omega$, spatial regions of interest can be divided into three zones:

the near (static) zone: $R \ll \lambda$,

the intermediate (induction) zone: $R \sim \lambda$,

the far (radiation) zone: $R \gg \lambda$.

In the near zone the fields have the character of static fields. In the far zone, the fields are transverse to the radius vector and fall off as R^{-1} , typical of radiation fields.

To solve the time-dependent problem, it is no longer valid to find an equation for the scalar potential Φ , defined as $\vec{E} = -\nabla\Phi$ because $\vec{\nabla} \times \vec{E} = -\partial\vec{B}/\partial t = i\omega\vec{B} \neq 0$. We have to define a vector potential \vec{A} such that

$$\vec{B} = \vec{\nabla} \times \vec{A}$$

and

$$\vec{E} = -\vec{\nabla}\Phi - \frac{1}{c} \frac{\partial \vec{A}}{\partial t}$$

The wave equation for \vec{A} in our case is

$$(\nabla^2 + 2k \frac{\partial}{\partial z}) \vec{A} - \frac{1}{c^2} \frac{\partial^2 \vec{A}}{\partial t^2} = - \frac{\vec{j}_s}{c\epsilon_0}. \quad (4-1)$$

The magnetic induction is given by

$$\vec{B} = \vec{\nabla} \times \vec{A}$$

and, outside the source, the electric field is

$$\vec{E} = \frac{ic}{\omega} \vec{\nabla} \times \vec{B}.$$

For a simpler case of Coulomb field $((2k)^{-1} \rightarrow \infty)$ (4-1) reduced to the familiar form

$$\nabla^2 A - \frac{1}{c^2} \frac{\partial^2 A}{\partial t^2} = - \frac{j_s}{c\epsilon_0} .$$

For an electric dipole with the dipole moment of

$$\vec{p} = \int \vec{x}' \rho(\vec{x}') d^3x' .$$

The solution of the fields are (Jackson, 1952)

$$\begin{aligned} \vec{B} &= \frac{\omega^2}{c^2} (\hat{n} \times \vec{p}) \frac{e^{i\frac{\omega}{c}R}}{R} \left(1 - \frac{1}{i k R}\right) \\ \vec{E} &= \frac{\omega^2}{c^2} (\hat{n} \times \vec{p}) \times \hat{n} \frac{e^{i\frac{\omega}{c}R}}{R} \\ &+ [3\hat{n}(\hat{n} \cdot \vec{p}) - \vec{p}] \left(\frac{1}{R^3} - \frac{i}{cR^2}\right) e^{i\frac{\omega}{c}R} \end{aligned} \quad (4-2)$$

In the near zone, $R \ll \lambda = 2\pi c/\omega$,

$$\vec{E} = 3\hat{n}[(\hat{n} \cdot \vec{p}) - \vec{p}] \frac{1}{R^3}$$

the electric field is just the static electric dipole field. In the far zone, $R \gg \lambda$,

$$\vec{E} = \frac{\omega^2}{c^2} (\hat{n} \times \vec{p}) \times \hat{n} \frac{e^{i\frac{\omega}{c}R}}{R}$$

the electric field shows the typical behavior of radiation fields.

We can now compare the magnitudes of radiation and static fields in the far zone. From (4-2), we obtain

$$\left| \frac{E_{\text{radiation}}}{E_{\text{static}}} \right| \sim \frac{\omega^2}{2c^2} = \frac{2\pi^2 f^2 R^2}{c^2} .$$

At a distance of 100 km away from the source, the ratio is about $2 \times 10^{-6} \times f^2$ where f is the frequency. In other words, if the frequency is close to 1 kHz, radiation and static fields are in the same order of magnitude at this distance. Above this frequency, radiation field will dominate.

The electrostatic field is the field that we obtained in Chapters 2 and 3; it is the only non-zero field before and after a lightning charge. The radiation field represents the energy propagated away from the source at the speed of light.

In the atmosphere, within a range of around 30 km from the lightning source, the dominating field is electrostatic. Beyond this distance, the induction and radiation terms start to contribute to the total field. In the far zone, the radiation term will be the only significant field.

Figure 4-11 shows the expected qualitative form of the three electric field components for a return stroke and also the resultant electric fields as a function of distance.

The lightning events experienced at the balloon can be assumed to be dominated by the electrostatic field component because the balloon was always no more than 30 km from the source region. Unfortunately, since the vector fields were taken only once every half a second, we are not able to see the fine structure of return strokes and possibly some of the induction effects on the total field.

The duration of the lightning activity measured by the balloon was between 0823 UT and 0834 UT. Our next job is to determine what type of lightning flashes they are, to trace the position of the active

lightning region relative to the balloon and to estimate the average discharge involved in each flash. We first summarize the data as follows:

- (1) The maximum change in vertical field caused by lightning was $\sim 0.60 - 0.70$ V/m in the downward direction.
- (2) The maximum horizontal fields were ~ 0.20 V/m and 0.25 V/m in the east and north directions respectively.
- (3) The ratio between vertical, east and north fields was about the same for all flashes. Furthermore, the values of fields were also in the same order of magnitude from one flash to another.

The direction of change in the vertical field indicated the lightning flashes experienced by the balloon could not be cloud-to-ground or cloud-to-sky; they had to be intracloud which involve downward positive discharge. The directions of changes in vertical fields due to various types of flashes are shown in Figure 4-12.

Comparison of (1) and (2) with results from (2-26) and (2-27) indicates that the source region was still north of the balloon trajectory as was the case earlier. The average amount of discharge was around 20 Coul and the flashes were about 18 km east ahead of the balloon; making the lightning region approximately 27 km northeast of the balloon. This agrees with the local weather observation at the time. From (3) we know the lightning fields measured for the balloon all came from the same general area. In other words, there was only this particular lightning active region within the range of balloon detection.

There were seven distinct lightning flashes observed by the balloon field sensors. The detail in the vertical field during each flash is shown in Figure 4-13. Table 4-1 is a summary of the amount of discharge, the time constant for field recovery (time τ required for the field to go back to $1/e$ of the peak value ΔE_{\max}).

From Figure 4-13 and Table 4-1, the amount of discharge for individual flash is between 18.5 Coul and 24 Coul. The time constant for field recovery varies between 2.5 and 7.5 seconds.

The problem of electric field recovery after lightning has been studied to some extent (Illingworth, 1971, 1972; Vonnegut et al., 1966). Experimental measurements and statistical analysis of recovery curves have been of great diversity and non-conclusive. However, the basics of physics of field response to the charge regeneration at different altitudes within the electrostatic range in the atmosphere can be outlined easily. Equations (2-1), (2-2) and (2-3) still hold.

$$\sigma_z = \sigma_0 \exp(2kz) \quad (2-1)$$

$$\vec{\nabla} \times \vec{E} = 0 \quad \text{or} \quad \vec{E} = -\vec{\nabla}\phi \quad (2-2)$$

$$\vec{j}_a = \sigma \vec{E} \quad (2-3)$$

(2-4) is no longer valid since non-steady state conditions have to be taken into consideration.

$$\vec{\nabla} \times \vec{H} = \vec{j} + \frac{\partial D}{\partial t} = \vec{j} + \epsilon_0 \frac{\partial E}{\partial t}$$

such that

$$\nabla \cdot \left(\vec{j} + \epsilon_0 \frac{\partial \vec{E}}{\partial t} \right) = 0$$

	peak value in vertical field E_{\max} (mV/m)	amount of discharge Q (Coul)	time constant for field recovery to $1/e$ (sec)
I	580	20	6.5
II	660	23	5.5
III	580	20	3.5
IV	700	24	7.5
V	550	19	2.5
VI	540	18.5	2.5
VII	660	23	6.0

Table 4-1

A general feature of the different lightning flashes

where

$$\vec{j} = \vec{j}_a + \vec{j}_s.$$

Equation (2-4) can then be rewritten as

$$\vec{\nabla} \cdot \vec{j}_a + \epsilon_0 \frac{\partial \vec{E}}{\partial t} = - \vec{\nabla} \cdot \vec{j}_s. \quad (4-3)$$

Equations (2-1), (2-2), (2-3), (4-3) together with Poisson's equation

$$\nabla^2 \phi = - \frac{\rho}{\epsilon_0} \quad (2-5)$$

then give

$$\nabla^2 \phi(\vec{x}, t) + 2k \frac{\partial \phi(\vec{x}, t)}{\partial z} + \frac{\epsilon_0}{\sigma} \frac{\partial}{\partial t} (\nabla^2 \phi(\vec{x}, t)) = - \frac{f(\vec{x}, t)}{\epsilon_0} \quad (4-4)$$

where f is the source function.

At $t = 0$, $\nabla^2 \phi$ can be derived from (2-26), $\partial/\partial t(\nabla^2 \phi)$ can be predicted as of the form

$$\frac{\partial}{\partial t} (\nabla^2 \phi) \propto - \frac{\sigma}{\epsilon_0} \frac{2k(z-z_0)}{R^3} + \text{image term}. \quad (4-5)$$

$\nabla^2 \phi$ at a later time may also be predicted. With the new $\nabla^2 \phi$ distribution we can find a new value of $\partial/\partial t(\nabla^2 \phi)$, and so advance for ϕ , the solution in time. This "finite difference method" was done by Illingworth (1972).

Estimates for time constant of recoveries are thus 20.4 sec at 18 km, 8.4 sec at 24 km and 4.6 sec at 35 km for a discharge at 6 km regardless of the amount of the discharge. This explains the more rapid recoveries at higher altitudes observed above clouds.

Recent observations of balloon flights by Winn and Byerly (1975) also indicated faster recoveries of electric fields at ground than at

balloon altitude. Furthermore, they described the pattern of field change as a nearly linear function of time. This is not a direct implication of (4-5). However, there are also other processes affecting the field recoveries in addition to the regeneration of the charge destroyed. Examples are the rearrangement of space charge in the conductivity gradient between the cloud and the air, the effects of local point discharges and reversal distance complications for cloud discharges. These may all change the predicted shape of the recovery curve.

Furthermore, we observed a definite correlation between the amount of discharge and recovery time constant (Figure 4-14). The time constant for field recovery is proportional to the amount of discharge. The simple linear correlation can be written as

$$\Delta E_{\max} = 485.4 + 25.7 \times \tau \quad (4-6)$$

where ΔE_{\max} is in mV/m and τ in seconds. The correlation coefficient r (a measure that shows how well the linear curve actually fits the data; $r = 1$ means perfect correlation and $r = 0$ is totally uncorrelated) is

$$r = \frac{m v_{ax}^2}{v_{ay}^2}$$

where m is the slope, v_{ax}^2 is the variance in the x values, and v_{ay}^2 is the variance in the y values. In our case

$$\begin{aligned} r &= \frac{25.7 \times v_{a\tau}}{v_{a\Delta E}} \\ &= 0.83. \end{aligned}$$

The lack of knowledge of the condition inside a storm prevents us from pursuing explanation for this observation further.

A better and more thorough system of solving the problem is definitely necessary. Detail observation of lightning field recoveries at different altitudes will also help in solving the mystery of charge mechanism during the active period of a thunderstorm.

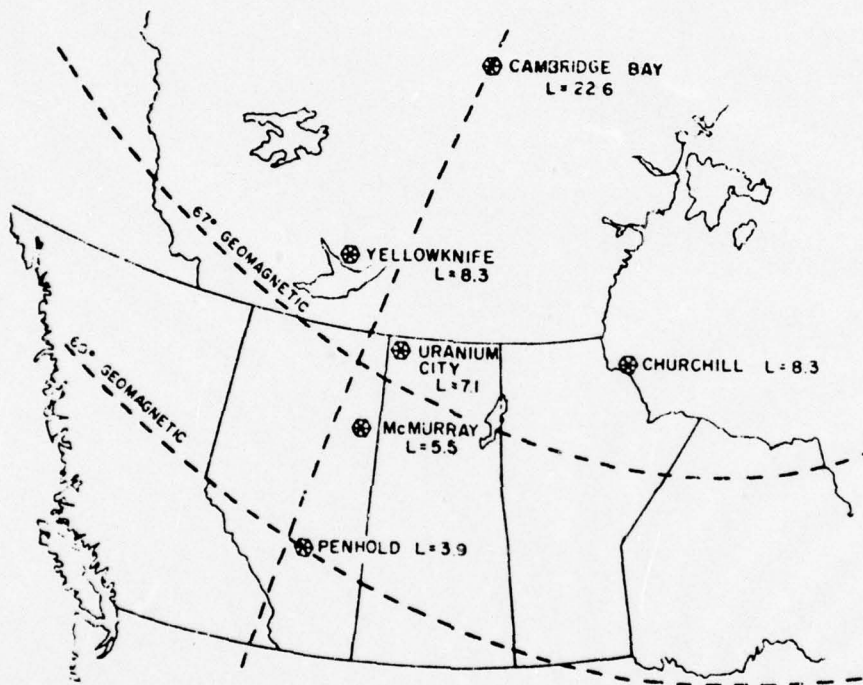


Figure 4-1

Map of Canada giving locations of the balloon launch sites. (Mozer and Manka, 1971)

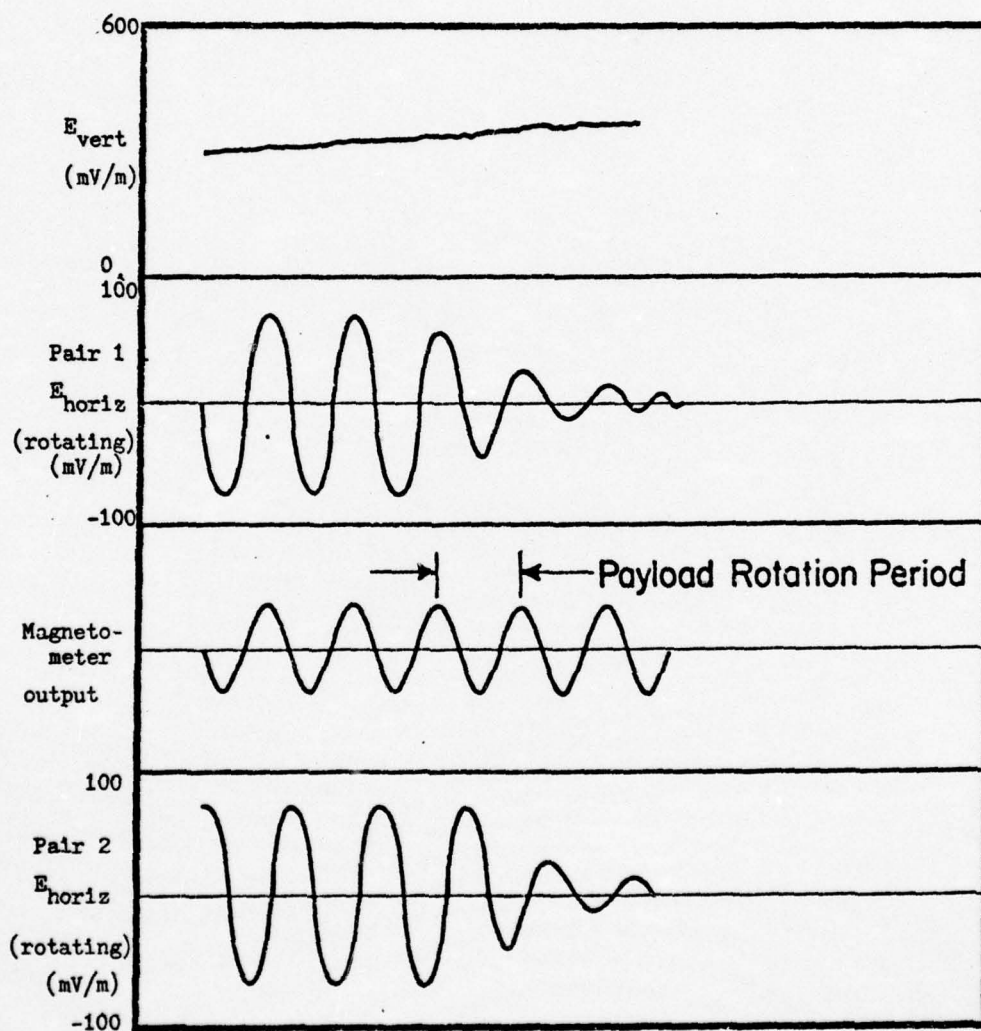


Figure 4-2

Raw data format of balloon E-field data

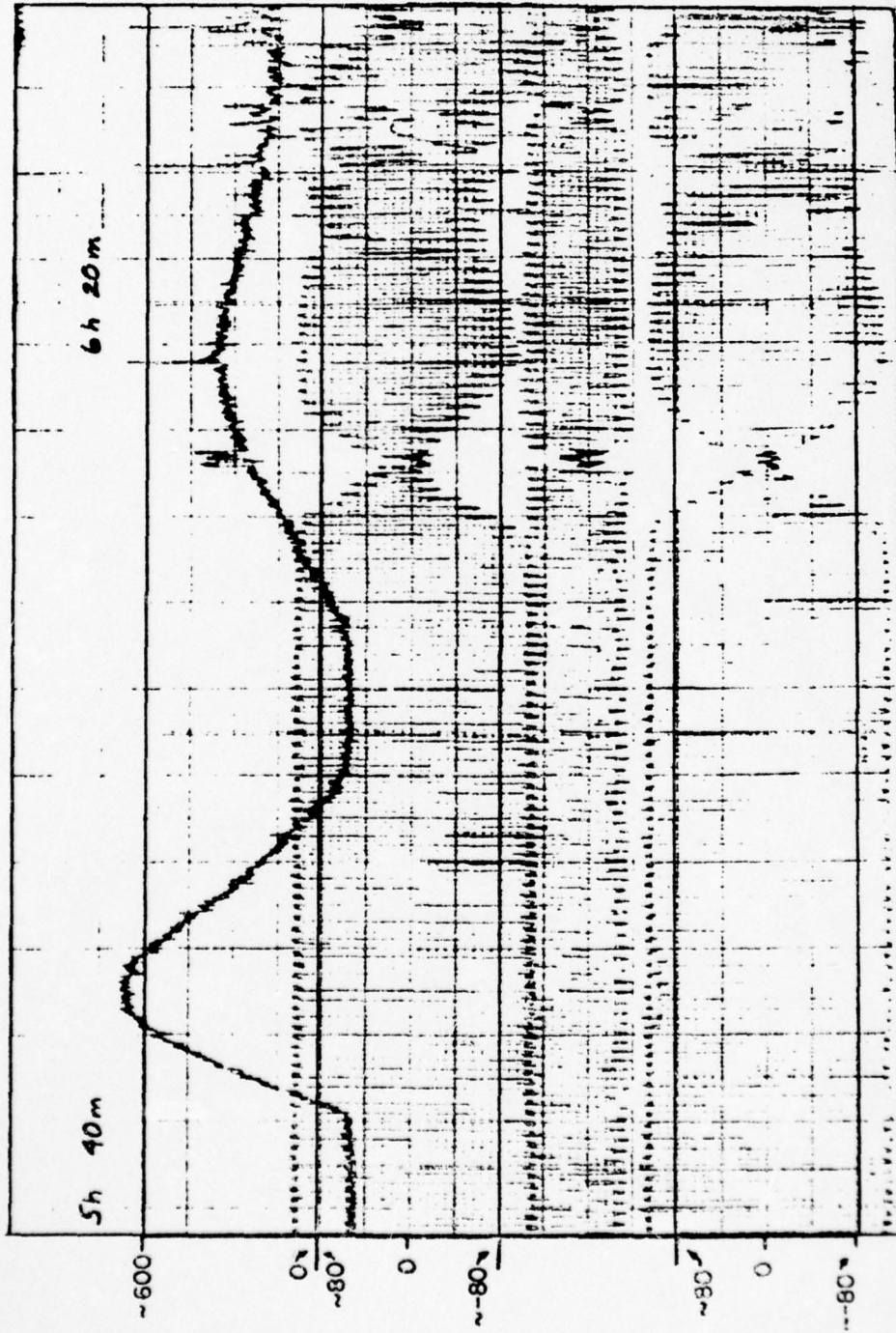


Figure 4-3a

AD-A032 509

RICE UNIV HOUSTON TEX DEPT OF SPACE PHYSICS AND ASTRONOMY F/G 4/1
LARGE SCALE ATMOSPHERIC ELECTRIC FIELDS: COMPARISONS WITH BALLO--ETC(U)
NOV 75 H K BURKE
TR061-761

N00014-67-A-0145-0006

NL

UNCLASSIFIED

2 OF 2

AD
A032509



END

DATE

FILMED

1-77

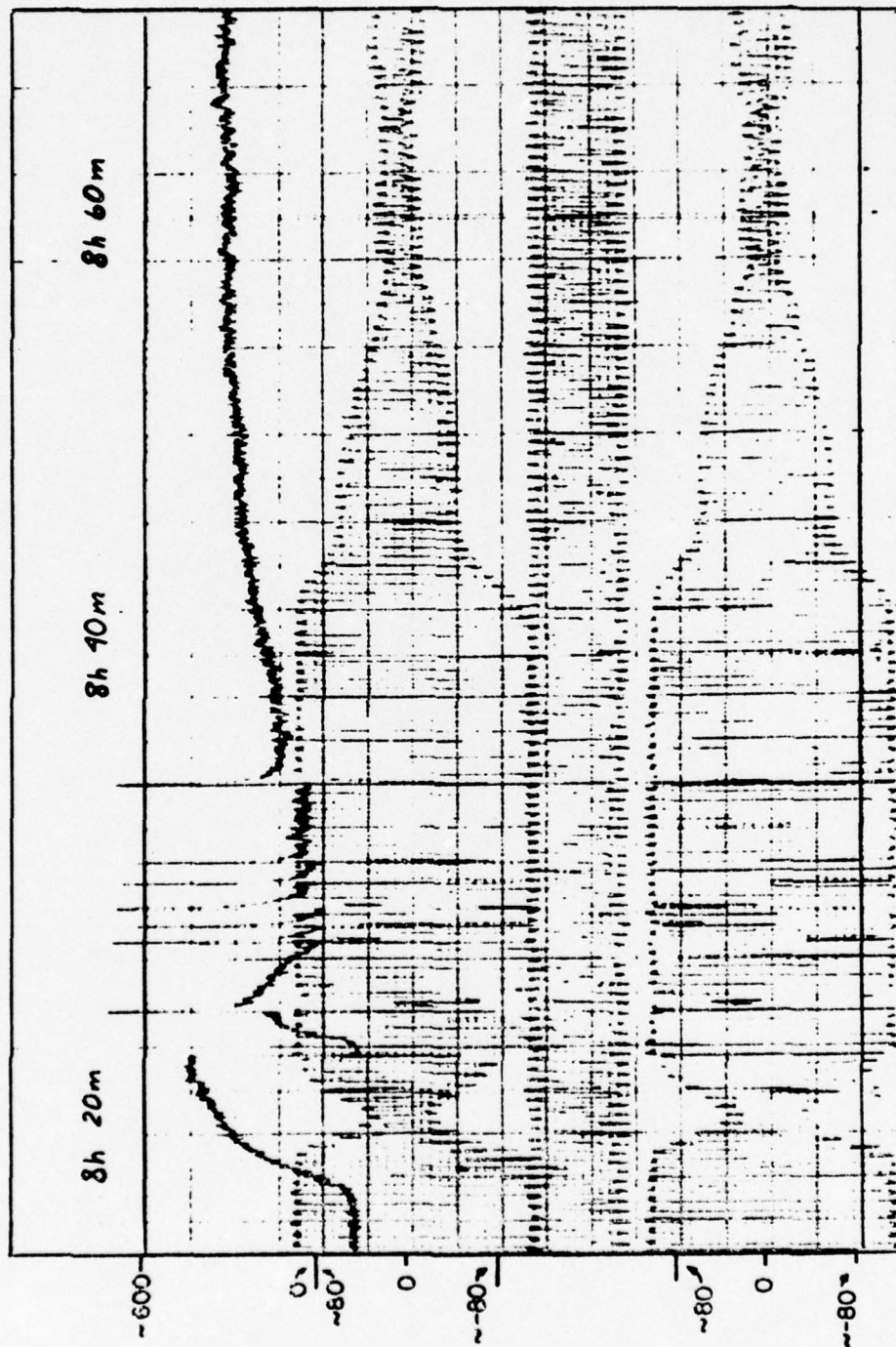


Figure 4-3b

Figure 4-3a

A portion of raw data indicating the presence of thunderstorm.

Figure 4-3b

Another portion of raw data indicating the presence of lightning activity

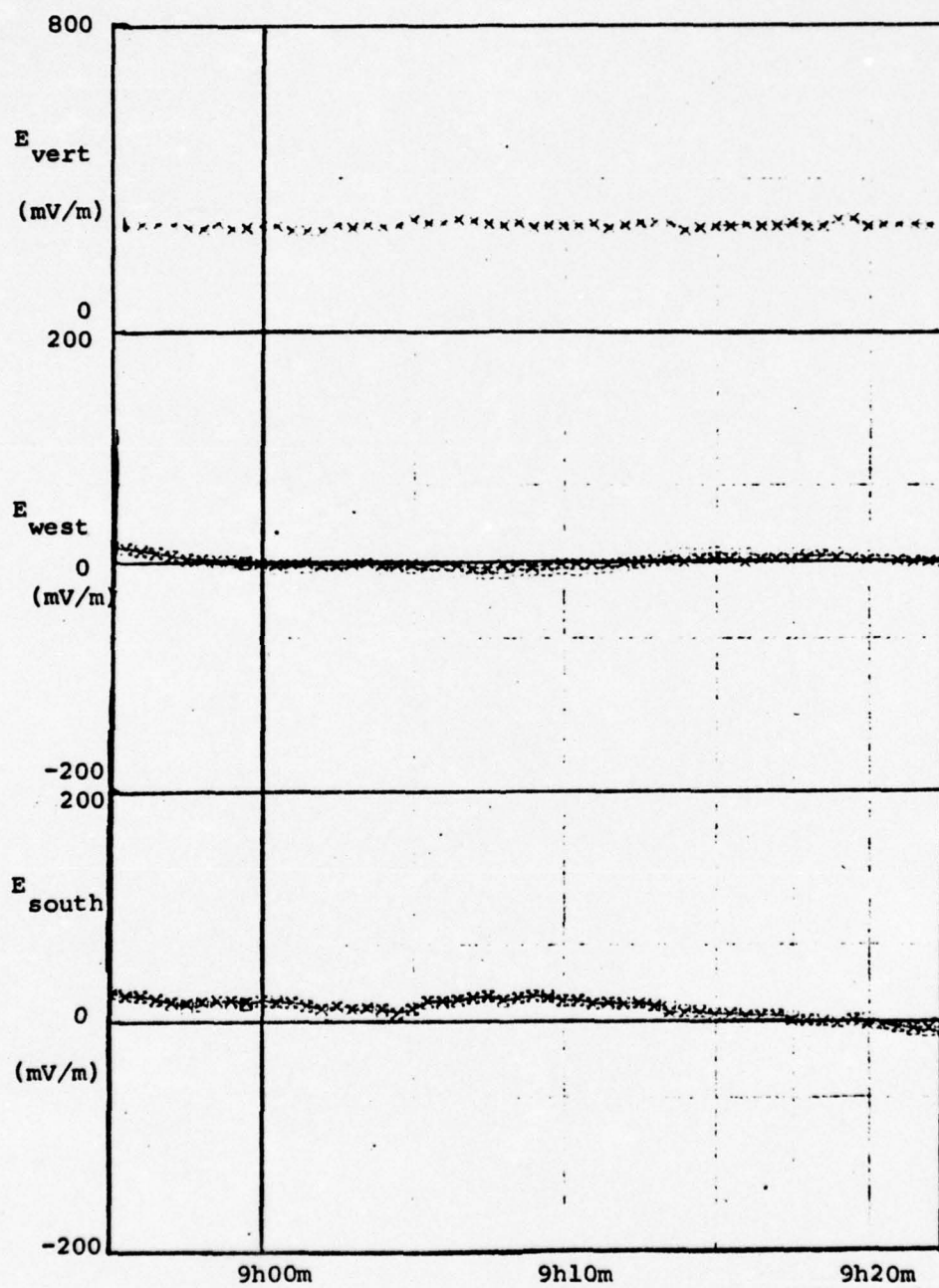
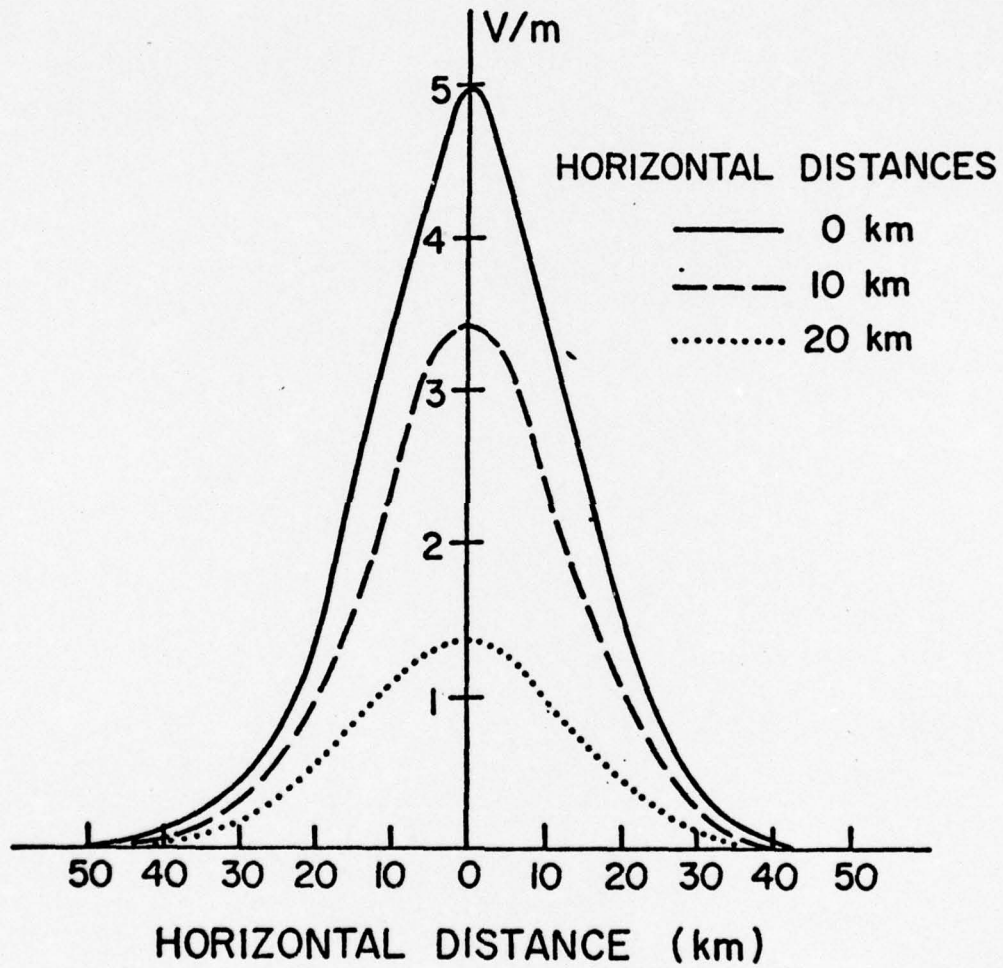


Figure 4-4

Vector electric fields during fair weather after the storm.

VERTICAL ELECTRIC FIELD EXPECTED AT BALLOON ALTITUDE



SCALE HEIGHT $(2k)^{-1} = 5$ km

+q (20C) at 6 km

-q (20C) at 3 km

Figure 4-5

EXPECTED ELECTRIC FIELD IN THE HORIZONTAL PLANE ALONG BALLOON TRAJECTORY

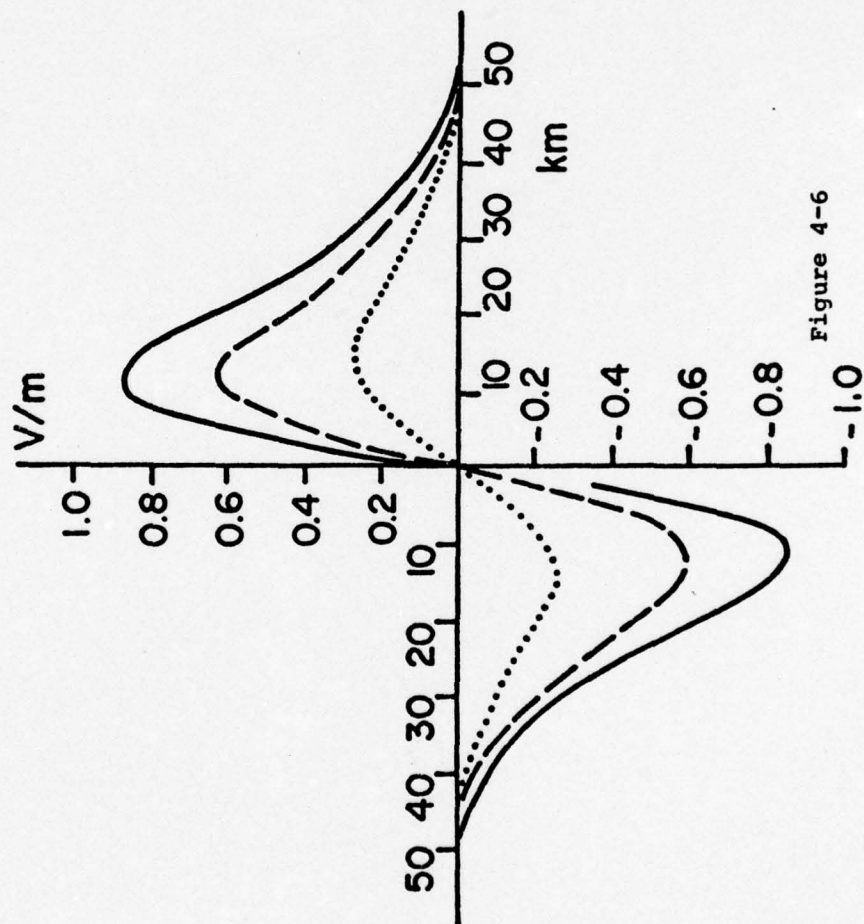


Figure 4-6

EXPECTED ELECTRIC FIELD IN THE HORIZONTAL PLANE PERPENDICULAR TO THE BALLOON TRAJECTORY

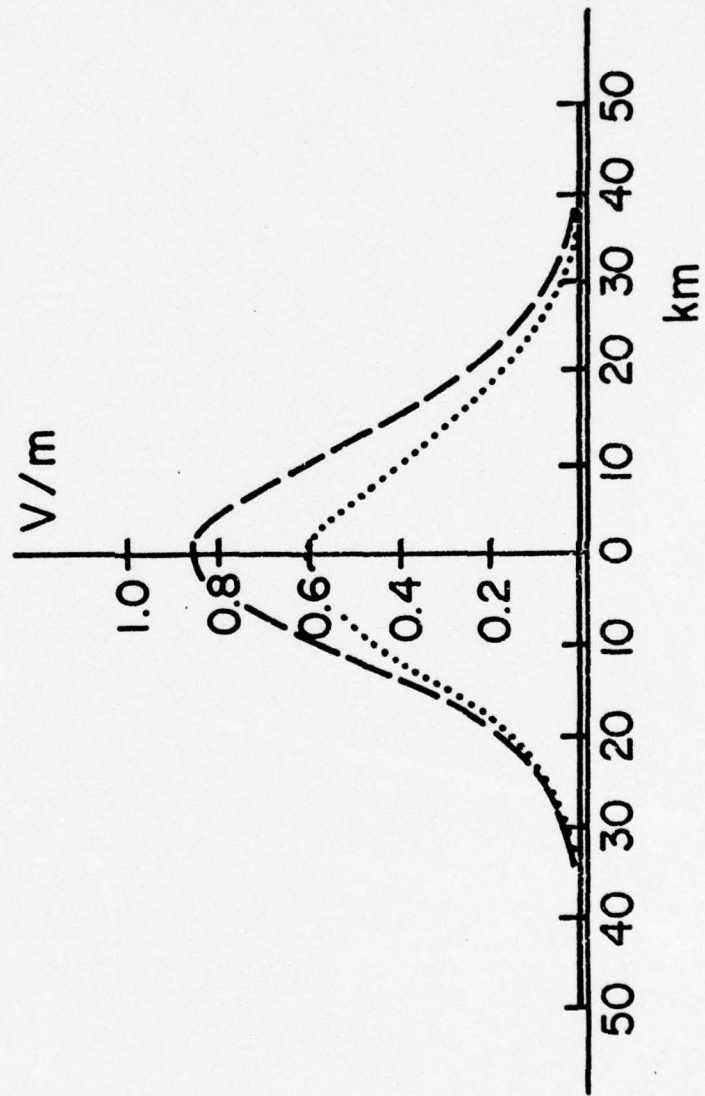


Figure 4-7

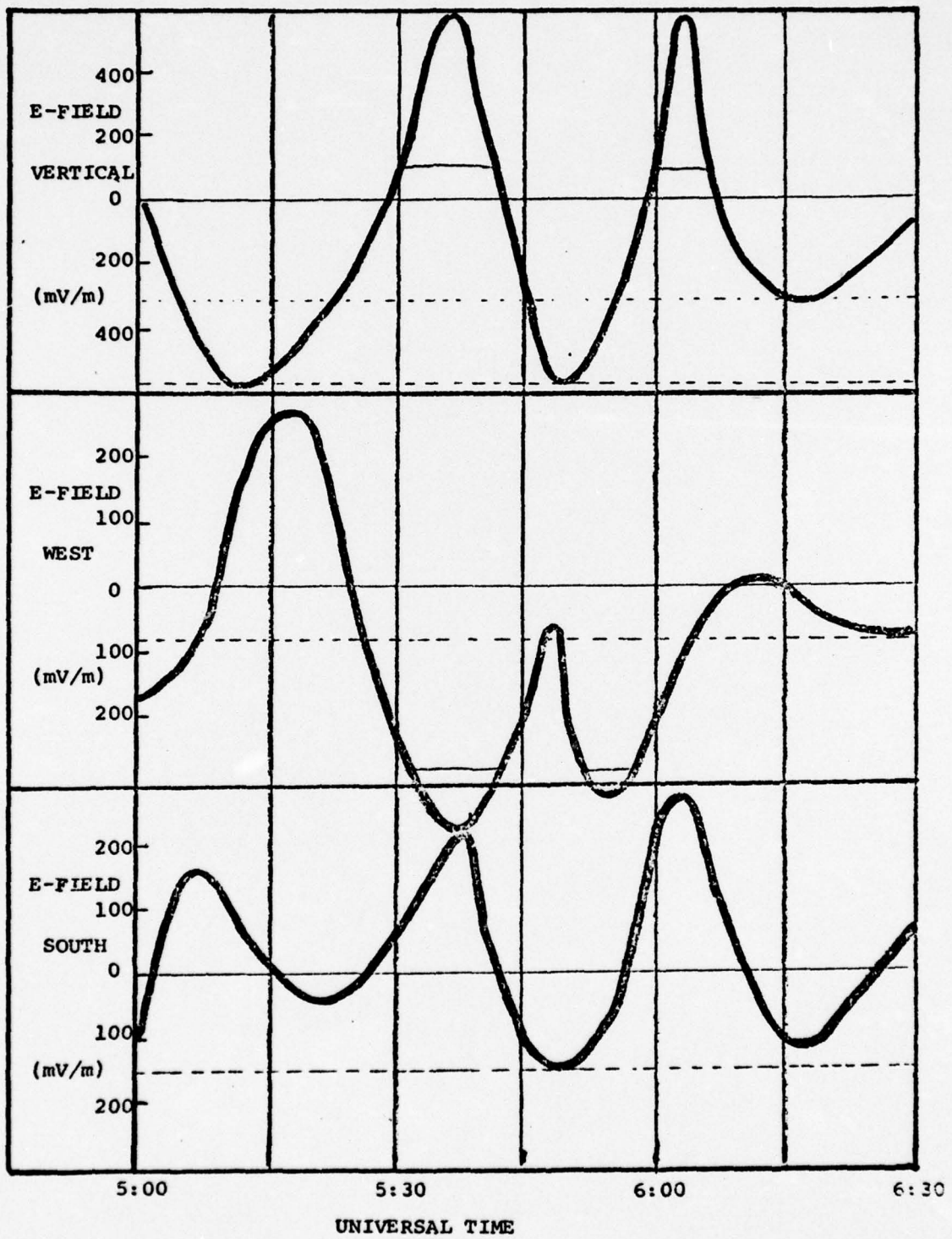


Figure 4-8

Vector electric fields during the thunderstorm from
0500 to 0630 UT observed by the balloon sensors at
90,000 ft.

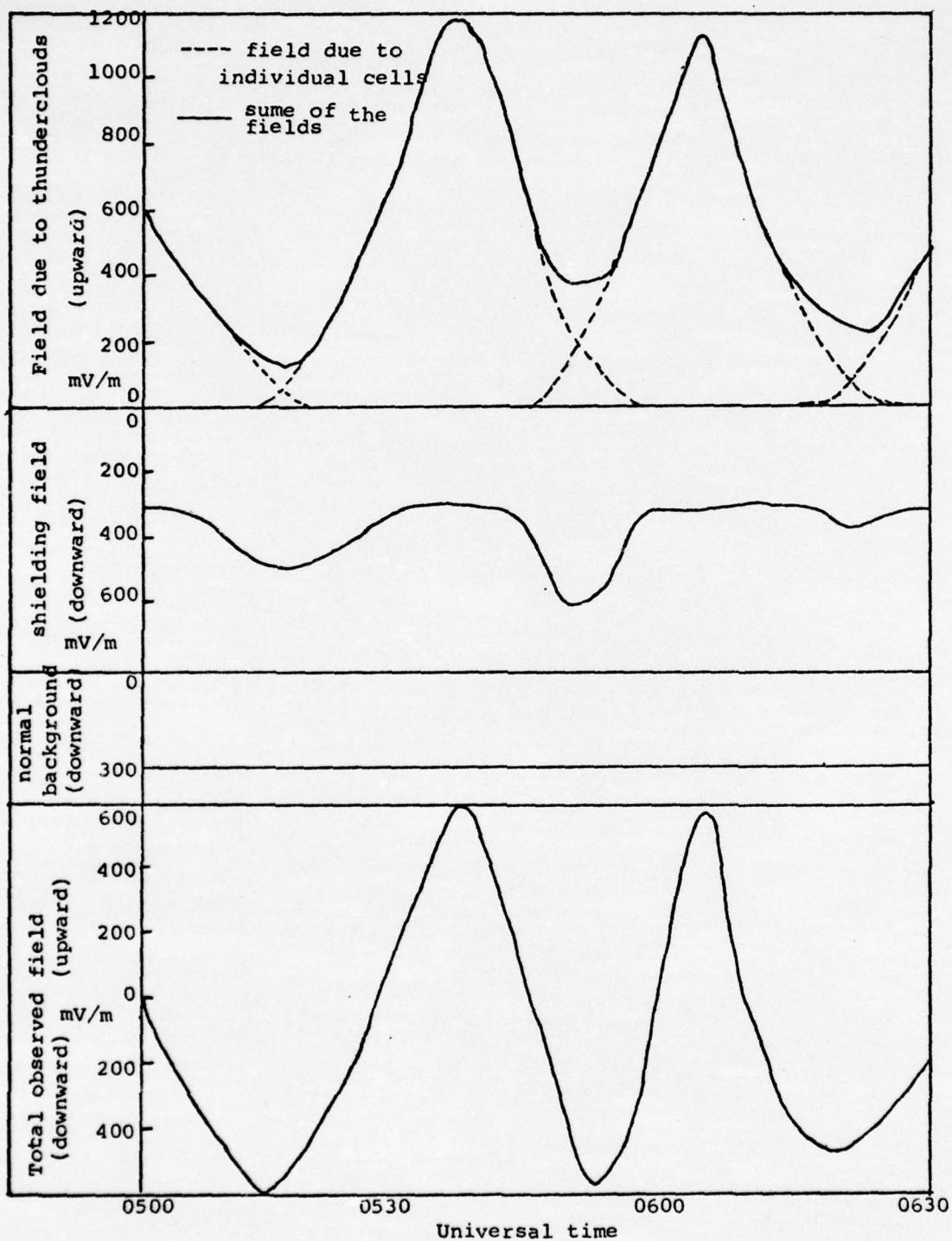


Figure 4-9

Observed vertical electric field as compared to different sources:

- (1) field due to thundercells (upward),
- (2) shielding field (downward), and
- (3) normal background field (downward).

The addition of the three sources shows agreement with the observed field.

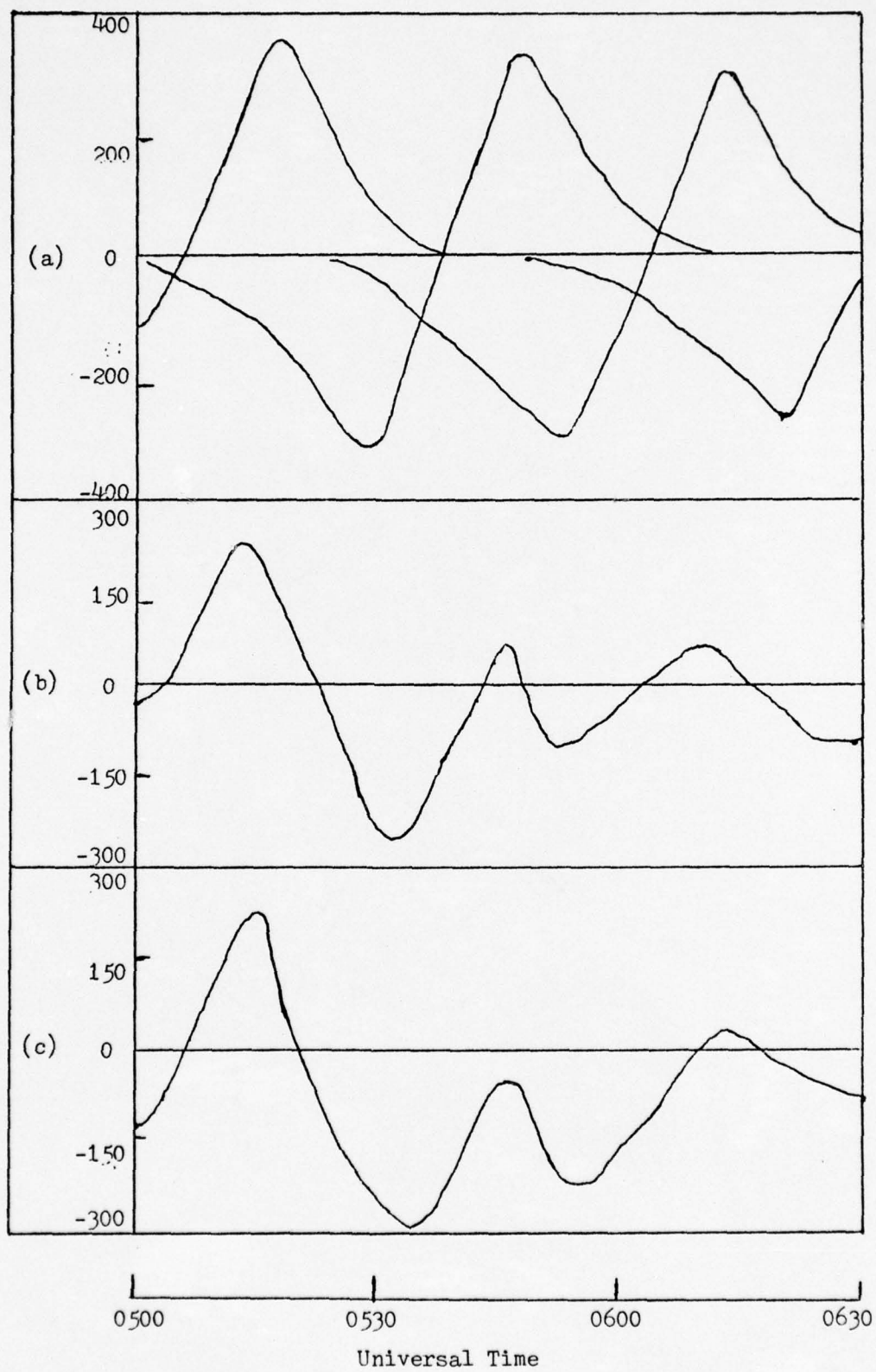


Figure 4-10

East-west (west is above the axis) electric field (in mV/m)
with respect to time:

- (a) field due to individual cells
- (b) resultant field from (a)
- (c) observed field

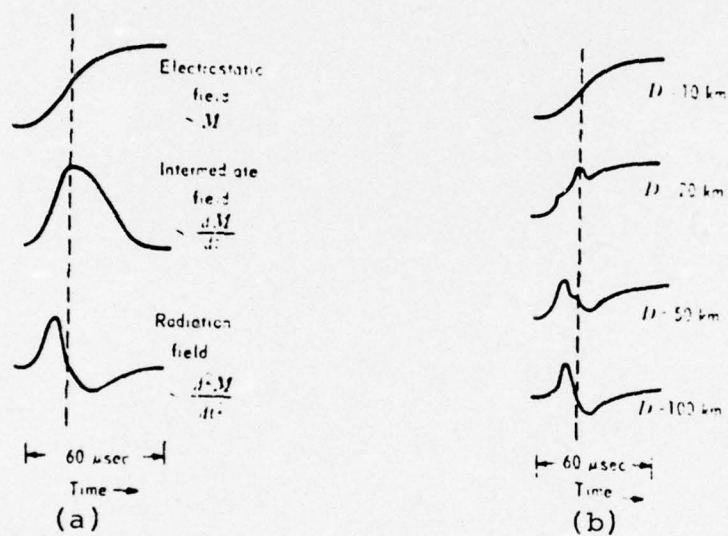
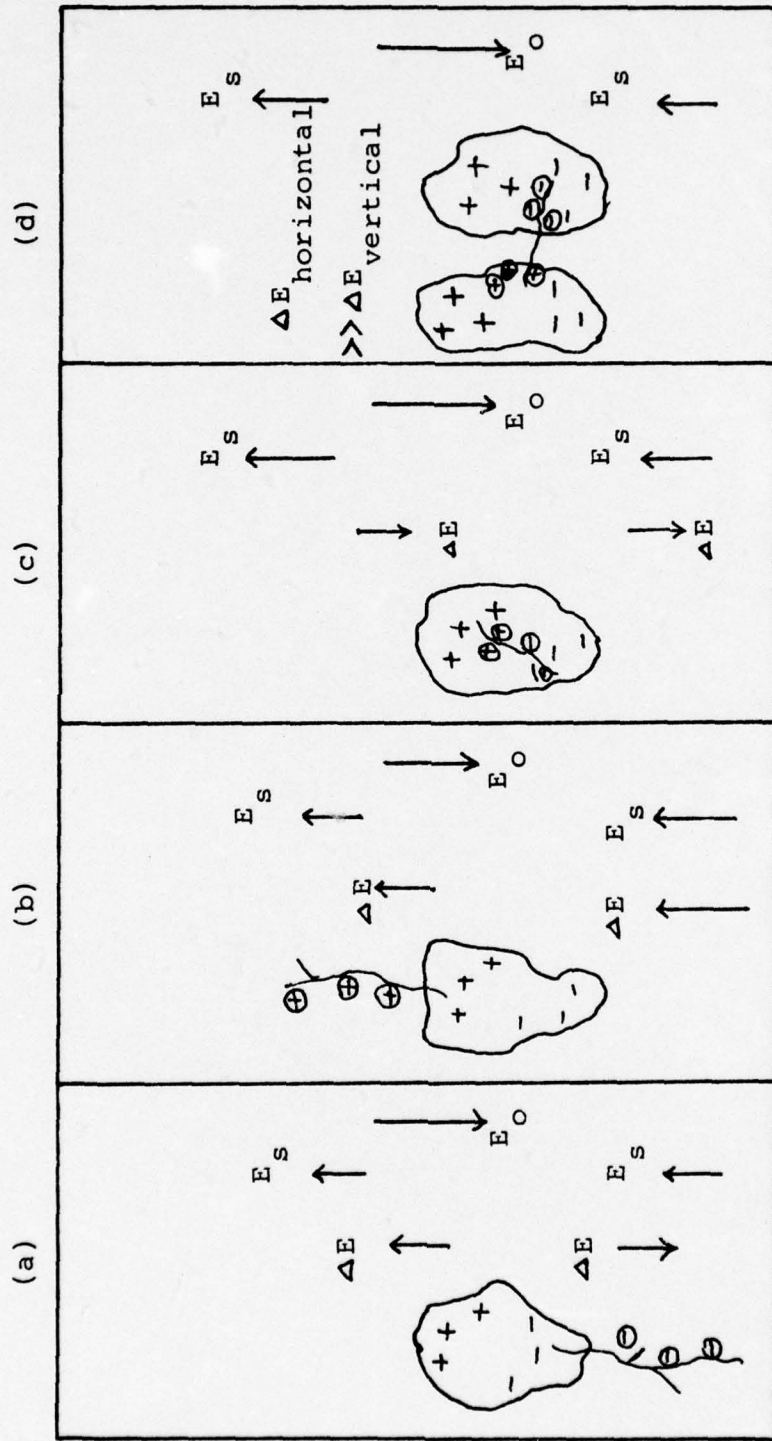


Figure 4-11

- (a) Electric field components vs. time for a return stroke.
- (b) Total electric field intensity vs. time at several distances due to the stroke.



E_o : normal, background field, E_s : static source field
 ΔE : vertical field change due to discharge

Figure 4-12

Changes of vertical fields due to different types of lightning flashes
 (a) cloud-to-ground
 (c) intracloud
 (b) cloud-to-sky
 (d) intercloud

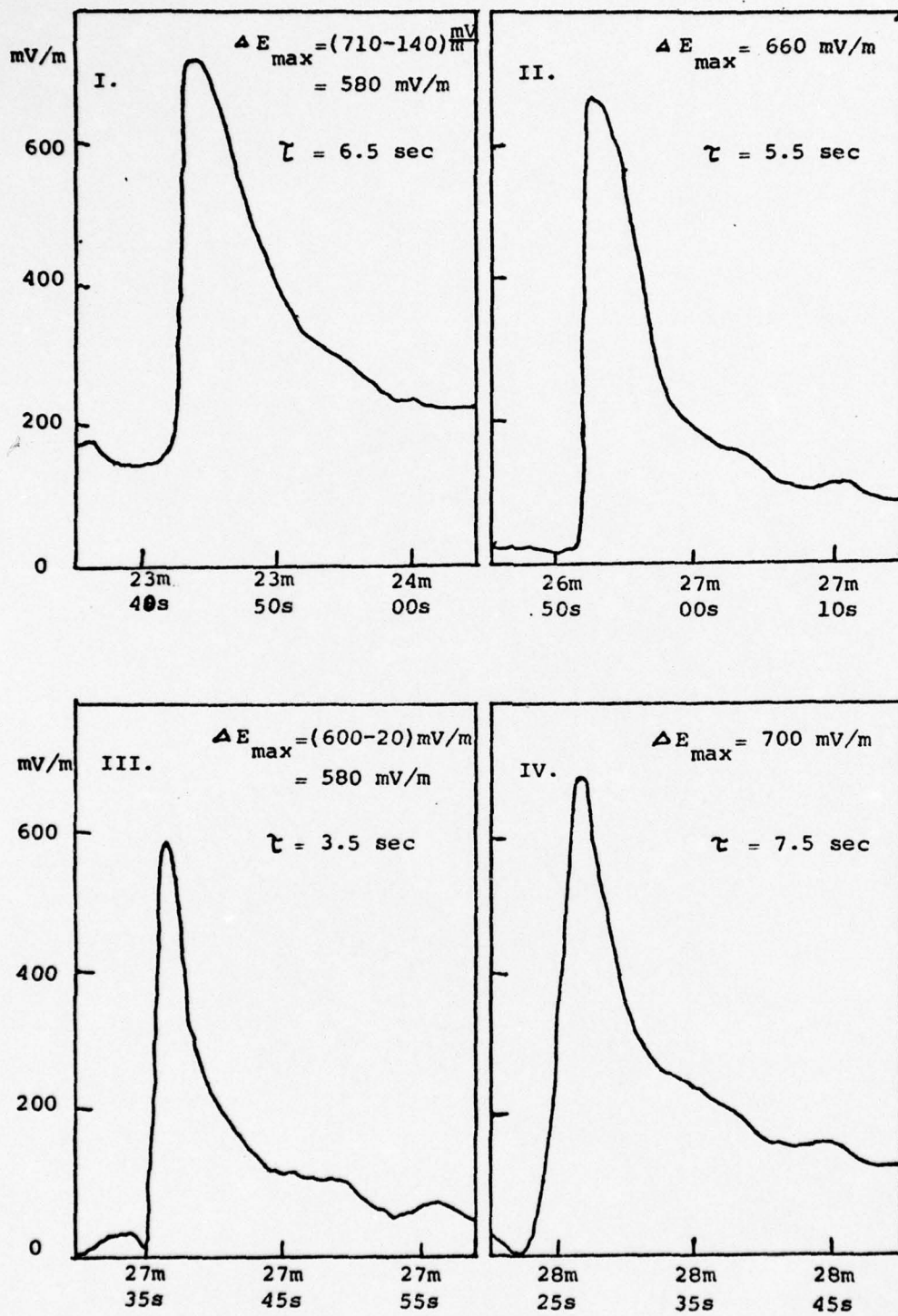


Figure 4-13

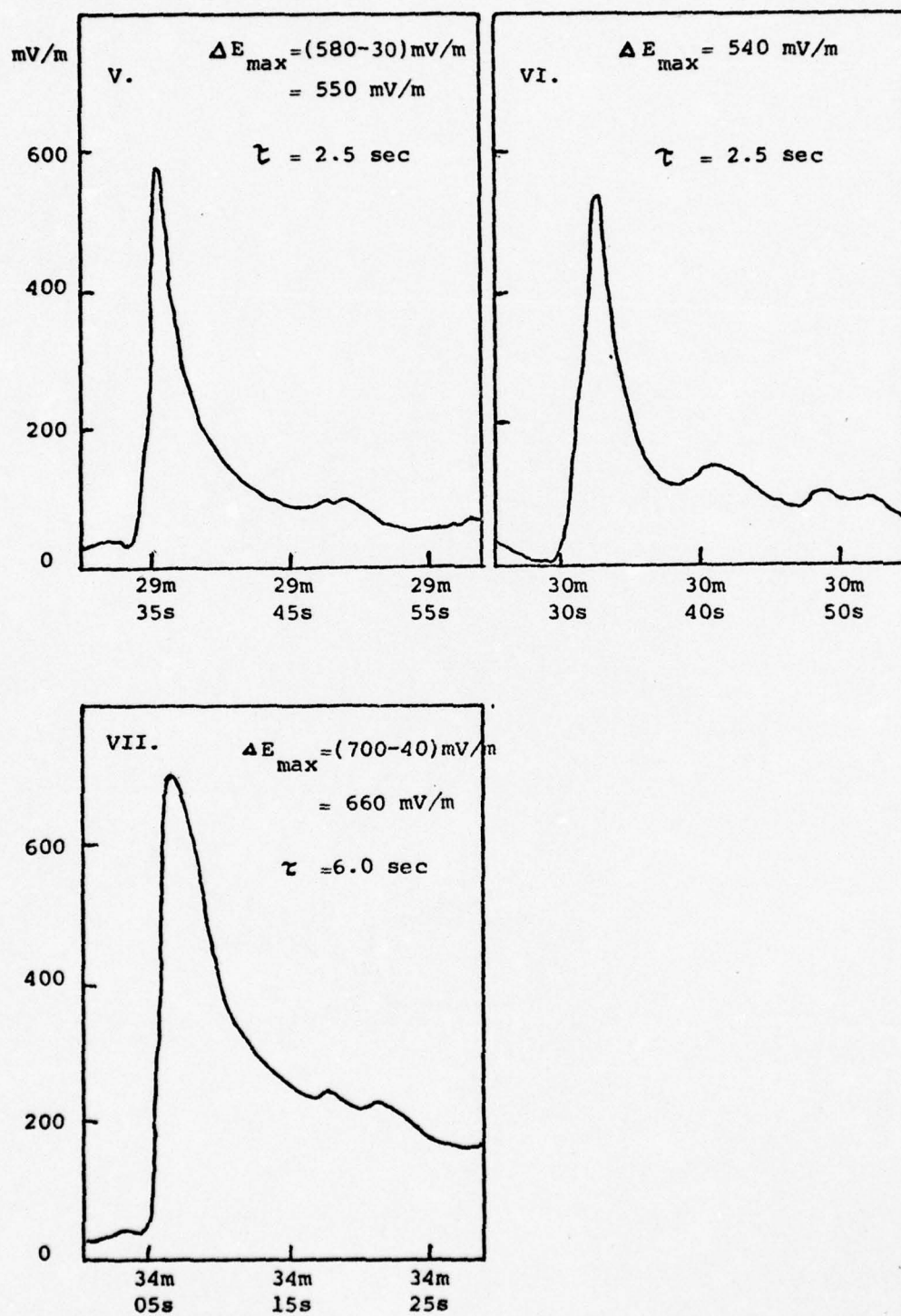


Figure 4-13 (continued)

Figure 4-13

Changes in the vertical fields indicating the presence of lightning flashes. ΔE_{\max} is the maximum change in field. τ is the relaxation time for field recovery.

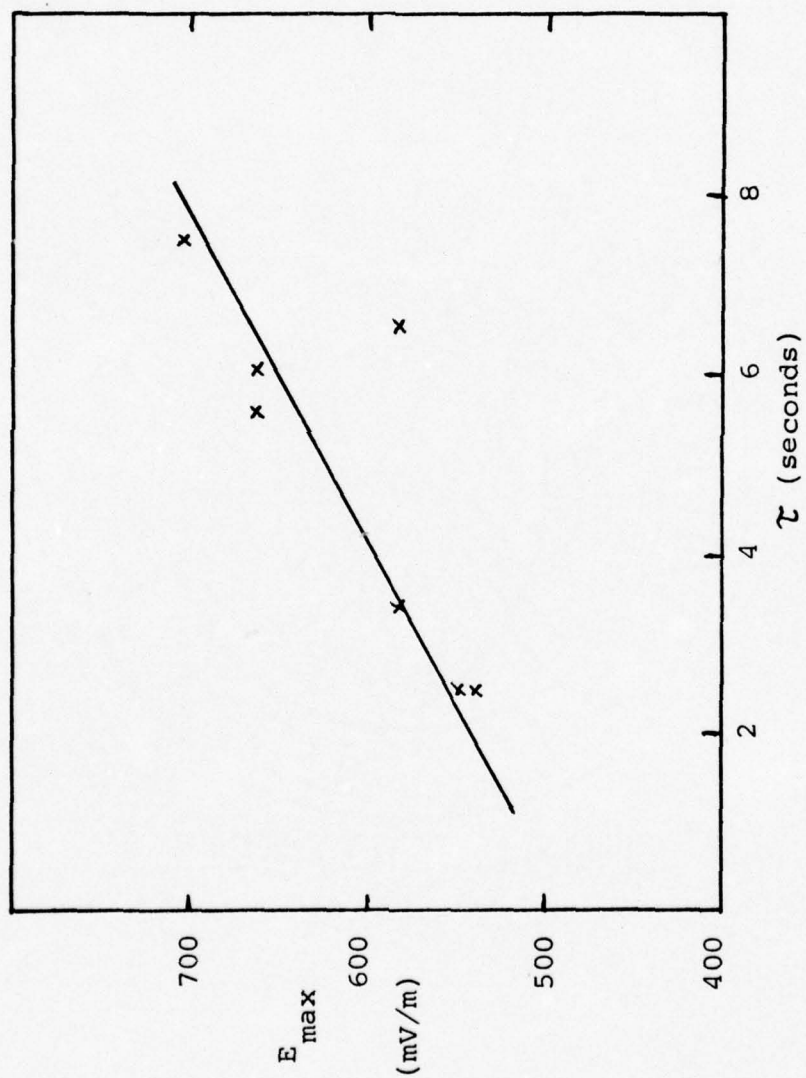


Figure 4-14
A linear correlation between E_{\max} and τ

CHAPTER 5

DISCUSSION

I. An Outline of Electrical Structures in the Atmosphere, Ionosphere, and Magnetosphere

In the previous chapters, we have studied the property of air conductivity and discussed how the atmospheric electric fields are mapped at different altitudes. Comparisons between the model and balloon data confirmed the relative position between the balloon and the thunderstorm. The charge concentration inside different cells was thus calculated. Furthermore, the mapping technique was also extended into the ionosphere. In this chapter, we will review the large scale coupling problem in both theoretical and experimental aspects and discuss the role of mapping technique in solving the problem.

Since Benjamin Franklin discovered electricity in lightning, the study of atmospheric electricity has been concerned mainly with the following problems:

- (1) the nature and origin of the atmospheric conductivity,
- (2) the origin and maintenance of earth's negative charge, and
- (3) the source and development of thunderstorm charges.

Meanwhile, the discovery of the regular diurnal variations in the geomagnetic field has made the subject of space electricity also the concern of ionospheric and magnetospheric researchers. It was the

investigations of whistler phenomena that led to the hypothesis that there exists a coupling relationship between the atmosphere, the ionosphere and the magnetosphere. General electrodynamic mechanism for each region is illustrated for an idealized height distribution in Figure 5-1 (Obayashi and Maeda, 1965).

In the atmosphere, there exists a downward electric field during fair weather conditions since the earth is negatively charged. The electric field is maintained mostly by convection currents provided by source currents from storm weather. The normal field intensity is about 130 V/m near ground but decreases with increasing altitude due to the increase of conductivity at higher altitudes. The total potential difference between the earth and the ionosphere is in the order of 4×10^5 volts. The current-electric field relationship in this region can be written as

$$\left(\frac{1}{\sigma} \right) \vec{j} = \vec{E}_s . \quad (5-1)$$

At ionospheric heights, the electric field is generated by convective motions. The sources at different latitude regions are:

- (1) At lower and middle latitude regions, the source is the interaction of tidal winds with geomagnetic field and charged particles in the upper atmosphere, the so-called "dynamo theory" (Chapman and Bartels, 1940).
- (2) At higher latitude regions (aurora and polar regions), the plasma flow and electric field pattern is shown in Figure 5-2. The two possible sources for the antisunward plasma flow over the polar cap and the sunward return flow in the aurora zone are: (a) viscous interaction (Axford and Hines,

1961), and (b) magnetic merging (Dungey, 1961).

The average magnitude of the field varies between 0 and 20 mV/m, depending on the conductivity in the region, the latitude location and local time. Large diurnal changes of amplitude and direction are the general rule in the ionosphere. The electric field which drives the current consists of two distinct parts: one due to the convection motion, producing an induction field $\vec{E}_i = \vec{v} \times \vec{B}$, and the other is the electrostatic field E_s resulting from the accumulation of polarization charges. The expression can be written as

$$\vec{j} \cdot (\vec{g})^{-1} = \vec{E}_s + \vec{v} \times \vec{B}$$

or

$$\vec{E}_s = \vec{j} \cdot (\vec{g})^{-1} - \vec{v} \times \vec{B} \quad (5-2)$$

In the magnetosphere the electric fields are generated by corotational motions within the plasmasphere and convective motions in the plasmasheet and high latitude lobes. The electrostatic field is such that it compensates the Lorentz force in order to preserve the convective motion. The representative magnitude is in the order of 1 mV/m. The corresponding expression in this region is

$$\vec{j} \cdot (\vec{g})^{-1} = 0$$

or

$$\vec{E}_s = - \vec{v} \times \vec{B} \quad (5-3)$$

II. Techniques of Electric Field Mapping

(i) Mapping between the Magnetosphere and Ionosphere

Wolf (1975) has given a thorough review on the coupling problem of the ionosphere and magnetosphere. Magnetic field lines in the higher ionosphere and magnetosphere can be considered to have high enough conductivity, at most times and places, such that a reasonable zero order picture of circulation in the ionosphere and magnetosphere can be obtained with the assumption that $\vec{E} \cdot \vec{B} = 0$. In the region of dipolar magnetic field lines, Mozer (1970) developed the relationships of electric fields between the two regions as

$$\frac{E_{\text{east}}^{\text{ionosphere}}}{E_{\text{east}}^{\text{equat. plane}}} = L^{3/2} \quad (5-4)$$

$$\frac{E_{\text{radial}}^{\text{ionosphere}}}{E_{\text{radial}}^{\text{equat. plane}}} = 2L^{3/2} \quad (5-5)$$

where the L-value of a particular point is the distance from the center of the earth at which the field line through that point crosses the equatorial plane. The unit of L is in earth radius.

Mapping of fields in the outer magnetosphere is a more complicated problem and will not be discussed here (for more references, see the review paper by Wolf, 1975).

Components of electric field parallel to magnetic field lines are the least understood even though their existence has been suggested by data from rocket-borne double probe experiments (Mozer and Fahleson, 1970;

Kelley et al., 1971). More experiments must be done in order to produce information on the average global distribution of total field aligned potential drops and thus to determine whether these fields play an important role in large scale ionosphere-magnetosphere dynamics.

(ii) Mapping between the Ionosphere and Atmosphere

Unlike the two-way relationship of electric fields between the ionosphere and the magnetosphere as expressed in (5-4) and (5-5), the field mapping from ionosphere down to the atmosphere is quite different from that of the atmosphere into the ionosphere. The main reasons are:

- (1) In the atmosphere, the weather-induced fields are due to charge sources. In the ionosphere, electric fields are mostly induced from $\vec{v} \times \vec{B}$ convections. Because of the high conductivity, regions of net charges cannot exist in the ionosphere.
- (2) In the atmosphere, the conductivity of air is isotropic and can be expressed as a scalar. In the ionosphere, the conductivity becomes anisotropic and the presentation is in tensor form.

Recent work on downward field mapping from the ionosphere into the atmosphere include Mozer (1971) and Volland (1972). Assuming scalar conductivity up to 100 km where ionospheric fields originate, both of them showed that these fields can map into the lower atmosphere (~ 30 km) without much attenuation. Using numerical techniques, Park (to be published) gave a more thorough treatment taking into consideration of the tensor presentation, possible horizontal gradient and other irregularities of ionospheric conductivity. Thus more generalized results are obtained.

Upward mapping of atmospheric electric fields into the ionosphere was reviewed in Chapter 2. In this thesis we developed an analytic solution for mapping of thunderstorm electric fields to different altitudes, including balloon altitudes and ionosphere. The results at balloon altitude agree with measured values. Near the boundary between the atmosphere and the ionosphere (~ 70 km), the thunderstorm induced fields are in the same order of magnitude as ionospheric fields — several to tens of millivolts per meter. In the ionosphere, the fields attenuate much faster so that thunderstorm induced fields will fall below the instrument detection range at ~ 100 km.

It seems paradoxical that ionospheric fields can map down to the atmosphere but the atmospheric fields dissipate rather quickly in the ionosphere. The explanation for this is simply that ionospheric conductivity is much greater than atmospheric conductivity; the electric field is mapped more efficiently along a path of decreasing conductivity ($k < 0$) than vice versa.

III. Experimental Techniques

The advantage of vector electric field measurements above thunderstorms is they avoid all ambiguities near ground; for example, corona discharges near trees and other ground conductors and the anomalies of conductivity between thunderclouds and ground. As a result, measurements above thunderstorms can give us first-hand information on the time history and electrical structure of the storm and thus help in monitoring the electrification processes inside thunderclouds.

Another advantage of field measurements at altitudes between 30 and 40 km is that electric fields of both atmospheric and ionospheric origins can be observed and studied. They can then provide valuable evidence in the ionosphere-atmosphere coupling problem.

Popular vehicles for electric field measurements at higher altitudes include (1) airplanes, (2) barium cloud releases, (3) rockets and (4) balloons. Airplanes provide the best control of detecting path. Their major problem lies in the determination of the enhancement factors since the payload is usually mounted at the tip of the plane where field distortion is the worst. Barium cloud releases are easy to perform, yet its application is mainly on the $\vec{v} \times \vec{B}$, convection, electric fields. Storm induced fields, since they do not always cross the magnetic field lines, cannot be accurately determined. Rockets are capable of accurate measurements. However, their flight durations are obviously not sufficient for studying the time variation of the fields. Balloons, on the other hand, even though it is not possible to control their exact path, compensate for most of the disadvantages of the other vehicles and thus are good payload carriers. Of course, in order to get a complete picture of the electrical structure of upper atmosphere, simultaneous measurements from satellite and ground bases are also necessary in addition to balloon measurements.

IV. Future Prospects

In short, we have shown the mapping technique from the atmosphere into the ionosphere. Our conclusion is that thunderstorm induced electric fields, after mapping into the ionosphere, are much less than field

produced by ionospheric or magnetospheric processes. Nonetheless, such fields might be responsible for formation of localized electron density enhancements, the so-called "magnetospheric ducts" (Mozer, 1971).

Another aspect requiring research is the VLF range of the lightning induced fields; even though electrostatic fields dissipate fast in the ionosphere, the radiation field is still a possible excitation source of geomagnetic pulsations in the magnetosphere (suggested by Dejnakintra and Park, 1974).

Furthermore, the subject of solar-terrestrial effects on the weather has drawn more and more interest and attention these days (Markson, 1971, 1975; Roberts and Olson, 1973; Silverman and Korff, 1975). Mapping techniques between magnetosphere, ionosphere and atmosphere will certainly be a first necessary step in setting up a theoretical model.

It is certainly encouraging that the science of atmospheric electricity is now experiencing more interactions with other disciplines of space studies. It will work to the benefit of all of science that these disciplines are now cooperating after so many years of isolated research.

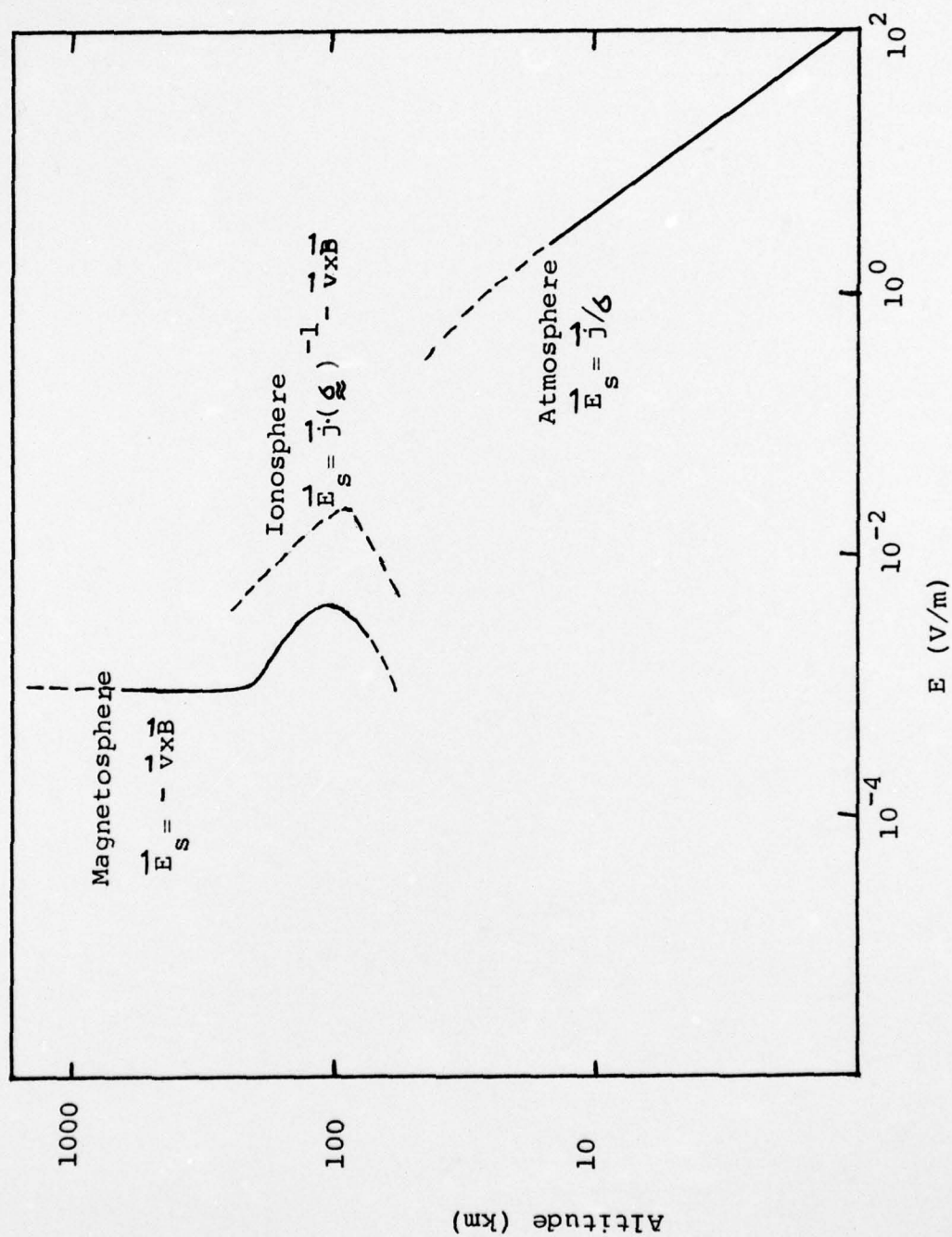


Figure 5-1

Electric Fields in the atmosphere, ionosphere and magnetosphere

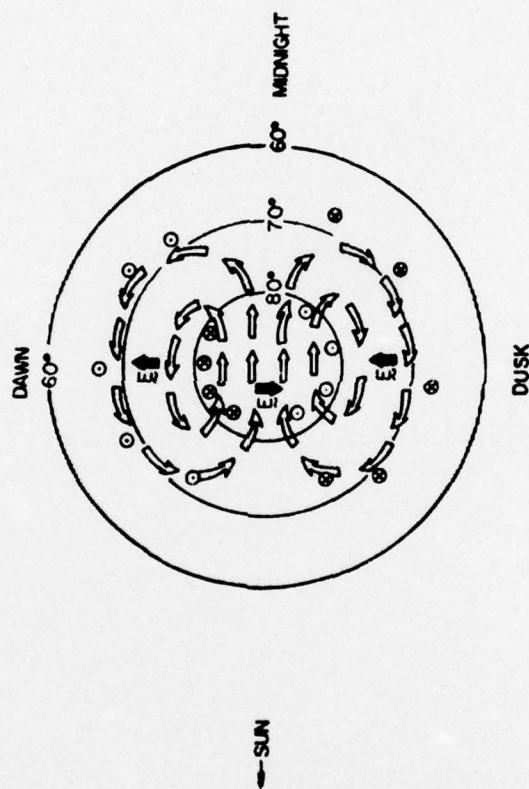


Figure 5-2

Pattern of plasma flow and electric fields in the high-latitude ionosphere. The sun is to the left. Hollow arrows give directions of flow (EXB drift). Heavy arrows are electric fields. (Wolf, 1975)

Mathametical Appendix

An Alternate Method of Solving
the Potential Problem in the Atmosphere with a Point Source

The Laplace equation to be solved is

$$\left(\nabla^2 + 2k \frac{\partial}{\partial z} \right) \Phi = 0$$

with boundary condition of charge q_1 at z_1 .

In the cylindrical coordinates:

$$\frac{1}{r} \frac{\partial}{\partial r} \left(r \frac{\partial \Phi}{\partial r} \right) + \frac{1}{r^2} \frac{\partial^2 \Phi}{\partial r^2} + \frac{\partial^2 \Phi}{\partial z^2} + 2k \frac{\partial \Phi}{\partial z} = 0.$$

Assuming azimuthal symmetry, separation by means of the product function gives

$$\Phi(r, z) = R(r)Z(z).$$

We obtain

$$\frac{d^2 R}{dr^2} + \frac{1}{r} \frac{dR}{dr} + m^2 R = 0 \quad (A-1)$$

$$\frac{d^2 Z}{dz^2} + 2k \frac{dZ}{dz} - m^2 Z = 0 \quad (A-2)$$

where m is a separation parameter. Equation (A-1) is known as Bessel's equation.

The solution of (A-1) is of the form

$$R(r) = C_1 J_0(mr) + C_2 Y_0(mr)$$

where $J_0()$ and $Y_0()$ are Bessel functions of first and second kind with zero order. Boundary condition here requires that as $r \rightarrow 0$, $R(r)$ remains finite

$$\therefore C_2 = 0$$

such that

$$R(r) = C_1 J_0(mr) \quad (A-3)$$

The solution of (A-2) is of the form

$$Z(z) = C_3 \exp \left[\left(\sqrt{m^2 + k^2} - k \right) (z - z_0) \right] \\ + C_4 \exp \left[\left(-\sqrt{m^2 + k^2} - k \right) (z - z_0) \right]$$

Boundary conditions in this case require that

$$\text{as } z \rightarrow \infty, Z(z) \rightarrow 0 \text{ such that } C_3 = 0 \text{ for } z > z_0$$

$$\text{and as } z \rightarrow -\infty, Z(z) \rightarrow 0 \text{ such that } C_4 = 0 \text{ for } z < z_0$$

$$Z(z) = \begin{cases} C_4 \exp \left[\left(-\sqrt{m^2 + k^2} - k \right) (z - z_0) \right] & \text{for } z > z_0 \\ C_3 \exp \left[\left(\sqrt{m^2 + k^2} - k \right) (z - z_0) \right] & \text{for } z < z_0 \end{cases} \quad (A-4)$$

$$(A-5)$$

where $z > z_0$ and $z < z_0$ refer to above and below the charge source respectively. (We are interested in the $z > z_0$ case.)

For $z > z_0$, we can write

$$\Phi_1 = \sum_{m=0}^{\infty} A_m J_0(mr) \exp \left[\left(-\sqrt{m^2 + k^2} - k \right) (z - z_0) \right] \quad (A-6)$$

and for $z < z_0$,

$$\Phi_2 = \sum_{m=0}^{\infty} A_m J_0(mr) \exp \left[\left(\sqrt{m^2 + k^2} - k \right) (z - z_0) \right] . \quad (A-7)$$

In order to find A_m , we apply boundary conditions at $z = z_0$ by means of

$$\int_0^\infty \int_0^\infty \delta(r) \delta(z-z_0) 2\pi r dr dz = 1$$

or

$$\int_0^\infty \delta(r) 2\pi r dr = 1 \quad (A-8)$$

as shown in Phillips and Panofsky (1962).

The flux condition at the plane $z = z_0$ is

$$\int \left[\frac{\partial \Phi_1}{\partial z} - \frac{\partial \Phi_2}{\partial z} \right]_{z=z_0} dA = \frac{1}{\epsilon_0} \int \rho dV$$

which implies that

$$2 \sum_{m=0}^{\infty} \sqrt{m^2+k^2} A_m J_0(mr) = \frac{q\delta(r)}{\epsilon_0} \quad (A-9)$$

Multiplying both sides of (A-9) by $rJ_0(m'r)$ and integrating over $r(0 \rightarrow \infty)$:

$$2\sqrt{m^2+k^2} A_m \int_0^\infty \left[J_0(mr) \right]^2 r dr = \frac{q J_0(0)}{2\pi\epsilon_0}$$

by using the relationship (A-8).

Since $J_0(0) = 1$, and

$$\int_0^\infty x J_p(kx) J_p(k'x) dx = \frac{1}{k} \delta(k' - k)$$

or

$$\int_0^\infty x \left(J_p(kx) \right)^2 dx = \frac{1}{k} ,$$

we obtain

$$2\sqrt{m^2+k^2} \cdot A_m \cdot \frac{1}{m} = \frac{q}{2\pi\epsilon_0}$$

or

$$A_m = \frac{q}{4\pi\epsilon_0} \cdot \frac{q}{\sqrt{m^2+k^2}}.$$

Now for $z > z_0$

$$\phi(r, z) = \frac{qe^{-k(z-z_0)}}{4\pi\epsilon_0} \int_0^\infty \frac{m}{\sqrt{m^2+k^2}} J_0(mr) e^{-(z-z_0)\sqrt{m^2+k^2}} dm.$$

By using the relationship in Gradshteyn and Ryzhik (1955, 6.616)

$$\begin{aligned} & \int_1^\infty J_0(r\sqrt{m'^2-1}) \exp(-zm') dm' \\ &= \frac{\exp(-\sqrt{r^2+z^2})}{\sqrt{r^2+z^2}}, \end{aligned}$$

we get

$$\phi(r, z) = \frac{q}{4\pi\epsilon_0} e^{-k(z-z_0)} \frac{e^{-k\sqrt{r^2+(z-z_0)^2}}}{\sqrt{r^2+(z-z_0)^2}}.$$

Introducing an image charge of $+q$ at $-z_0$ to match the boundary condition on the ground such that $\phi = 0$ at $z = 0$,

$$\phi = \frac{q}{4\pi\epsilon_0} e^{-k(z-z_0)} \left[\frac{e^{-k\sqrt{r^2+(z-z_0)^2}}}{\sqrt{r^2+(z-z_0)^2}} - \frac{e^{-k\sqrt{r^2+(z+z_0)^2}}}{\sqrt{r^2+(z+z_0)^2}} \right],$$

the same result as (2-26).

ACKNOWLEDGEMENTS

I am indebted to my thesis advisor, Professor Arthur A. Few, for the motivation of this thesis work and the many valuable discussions. For four and a half years at Rice, Dr. Few not only introduced me to the beauty of atmospheric electricity; he also taught me the methods of research from which I will benefit for many years to come.

I have to thank Dr. Robert H. Manka, the co-principle investigator of the project, for his many helpful suggestions. I also want to thank Professor Forest S. Mozer of the University of California at Berkeley, who provided the data. He and Dr. Manka made this research work possible.

Furthermore, I owe the most to my husband, Dr. William J. Burke, for his constant encouragement and stand-by assistance. Without him, a lot of the derivation work in this thesis would have remained unsolved. Special appreciation also goes to our daughter, Elaine, who was born at the beginning of the project. She made the life of a mother graduate student as happy and rewarding as it could be.

This thesis work was supported by the Physics and Atmospheric Science Sections of the Office of Naval Research Contract Number N00014-67-A-0145-0006 and by The National Aeronautics and Space Administration SR & T Grant NGL 44-006-012. Thanks are also due to Ms. Anita Poley for her excellent typing job.

REFERENCES

- Anderson, F.J. and G.D. Freier, Interactions of the Thunderstorm with a Conducting Atmosphere, *J. Geophys. Res.*, 74 (23), 5390, 1969.
- Axford, W.I. and C.O. Hines, A Unifying Theory of High-Latitude Geophysical Phenomena and Geomagnetic Storms, *Can. J. Phys.*, 39, 1433, 1961.
- Benbrook, J.R., J.W. Kern and W.R. Sheldon, Measured Electric Field in the Vicinity of a Thunderstorm System at an Altitude of 37 km, *J. Geophys. Res.*, 79 (34), 5289, 1974.
- Boström, R., A Model of the Auroral Electrojets, *J. Geophys. Res.*, 69 (23), 4983, 1964.
- Bragin, I.A., Direct Measurements of Ion and Electron Concentration in the Stratosphere and the Mesosphere, *Space Res.*, 7, 391, 1967.
- Chalmers, J.A., Atmospheric Electricity, 2nd Edition, Pergamon Press, New York, 1967.
- Chapman, S. and J. Bartels, Geomagnetism, Oxford Univ. Press, Oxford, 1940.
- Cole, R.K. and E.T. Pierce, Electrification in the Earth's Atmosphere for Altitudes between 0 and 100 km, *J. Geophys. Res.*, 70 (12), 2735, 1965.
- Dejnakarintra, M. and C.G. Park, Lightning-Induced Electric Fields in the Ionosphere, 79 (13), 1903, 1974.
- Dungey, J.W., Interplanetary Magnetic Field and the Auroral Zones, *Phys. Rev. Letters*, 6, 47, 1961.
- Gradshteyn, I.S. and I.M. Ryzhik, Table of Integrals, Series, and Products, 4th Edition, Academic Press, New York, 1965.

- Hatakeyama, H., Atmospheric Electricity Research in the Far East, Proc. of the Third International Conf. on Atmospheric and Space Electricity, 11, 1965.
- Hilderbrand, F.B., Advanced Calculus for Engineers, Prentice-Hall, Inc., New York, 1955.
- Holzer, R.E. and D.S. Saxon, Distribution of Electrical Conduction Currents in the Vicinity of Thunderstorms, J. Geophys. Res., 57 (2), 207, 1952.
- Illingworth, A.J., The Variation of the Electric Field after Lightning and the Conductivity within Thunderclouds, Quart. J. R. Met. Soc., 97, 440, 1971.
- Illingworth, A.J., Electric Field Recovery after Lightning as the Response of the Conducting Atmosphere to a Field Change, Quart. J. R. Met. Soc., 98, 604, 1971.
- Jackson, J.D., Classical Electrodynamics, John Wiley & Sons, Inc., New York, 1962.
- Kraakevik, J.H., The Airborne Measurement of Atmospheric Conductivity, J. Geophys. Res., 63 (2), 161, 1958.
- Kelley, M.C., F.S. Mozer and U.V. Fehleson, Measurements of the Electric Field Component of Waves in the Auroral Ionosphere, Planet. Space Sci., 18, 847, 1970.
- Manka, R.H. and F.S. Mozer, Global Electric Fields Measured in the Stratosphere, Contributed Paper at Fifth International Conf. on Atmospheric Electricity, Garmisch-Partenkirchen, 1974.
- Markson, R., Solar Sector -- Thunderstorm Relationship and Proposed Mechanism for Solar Control of Atmospheric Electrical Activity, Presented at I.U.G.G., Grenoble, 1975.

- Markson, R., Considerations Regarding Solar and Lunar Modulation of Geophysical Parameters, Atmospheric Electricity, and Thunderstorms, Pure and Applied Geophys., 84, 161, 1971.
- Monthly Bulletin, Canadian Upper Air Data, Dept. of Transport., Toronto, August, 1969.
- Mozer, F.S., Electrical Field Mapping in the Ionosphere at the Equatorial Plane, Planet. Space Sci., 18, 259, 1970.
- Mozer, F.S., Balloon Measurement of Vertical and Horizontal Atmospheric Electric Fields, Pure Appl. Geophys., 84, 32, 1971.
- Mozer, F.S., Simultaneous Electric Field Measurements on Nearby Balloons, J. Geophys. Res., 77 (31), 6129, 1972.
- Mozer, F.S. and P. Lucht, The Average Auroral Zone Electric Field, J. Geophys. Res., 79 (7), 1001, 1974.
- Mozer, F.S. and U.V. Fablesen, Parallel and Perpendicular Electric Fields in an Aurora, Planet. Space Sci., 18, 1563, 1970.
- Mozer, F.S. and R.H. Manka, Magnetospheric Electric Field Properties Deduced from Simultaneous Balloon Flights, J. Geophys. Res., 76 (7), 1697, 1971.
- Mozer, F.S. and R. Serlin, Magnetospheric Electric Field Measurements with Balloons, J. Geophys. Res., 74 (19), 4739, 1969.
- Obayashi, T. and K. Naeda, The Electrical State of the Upper Atmosphere, Proc. of the Third International Conf. on Atmospheric and Space Electricity, 532, 1965.
- Paltridge, G.W., Experimental Measurements of the Small Ion Density and Electrical Conductivity of the Stratosphere, J. Geophys. Res., 70 (12), 2751, 1965.

Panofsky, W.K.H. and M. Phillips, Classical Electricity and Magnetism, 2nd edition, Addison-Wesley, Reading, 1962.

Park, C.G., Downward Mapping of High Latitude Ionospheric Electric Fields to the Ground, to be published in J. Geophys. Res., 1975.

Park, C.G. and M. Dejnakarindra, Penetration of Thundercloud Electric Fields into the Ionosphere and Magnetosphere, 1. Middle and Subauroral Latitudes, J. Geophys. Res., 78 (28), 6623, 1973.

Phillips, B.B., Ionic Equilibrium and the Electrical Conductivity in Thunderclouds, Monthly Weather Rev., 95 (12), 854, 1967.

Roberts, W.O. and R.H. Olson, New Evidence of Variable Solar Corpuscular Emission on the Weather, Rev. Geophys. Space Phys., 11, 731, 1973.

Sagalyn, R.C. and D.R. Fitzgerald, Atmospheric Electricity, Chap. 8, Handbook of Geophysics and Space Environments, Air Force Cambridge Res. Lab., 1965.

Silverman, S.F. and D.F. Korff, Solar Sector Effects on Near-Earth Atmospheric Electric Fields at Thule, Greenland, presented at I.U.G.G., Grenoble, 1975.

Smythe, W.R., Static and Dynamic Electricity, 3rd edition, McGraw-Hill, New York, 1968.

Solar-Geophysical Data, (Prompt Reports), 302, I, for August and September 1969, ESSA Research Lab, U. S. Dept. of Commerce, 1969.

Uman, M.A., Lightning, McGraw-Hill Book Company, New York, 1969.

Volland, H., Mapping of the Electric Field of the Sq. Current into the Lower Atmosphere, J. Geophys. Res., 77 (10), 1961, 1972.

Vonnegut, B., C.B. Moore, R.O. Espinola and H.H. Blau, Jr., Electric Potential Gradients above Thunderstorms, J. Atm. Sci. 23, 764, 1966.

Winn, P.W. and L.G. Byerley, III, Electric field Growth in Thunderclouds, to be published in J. Geophys. Res., 1976.

Wolf, R.A., Ionosphere-Magnetosphere Coupling, Space Sci. Rev., 17, 537, 1975.